RCЛ
Review

Contents

Sensitivity and Resolution of Charge-Coupled Imagers at Low Light Levels

J. E. Carnes and W. F. Kosonocky

RCA Laboratories, Princeton, N.J.

Abstract—An analysis is presented of the expected sensitivity and resolution of charge-coupled imagers (CCI's) at low light levels. The results show that a 500 × 500 element CCI is expected to have a sensitivity limited by two noise sources of comparable magnitude: shot noise of the thermally-generated background charge and noise associated with fast interface state trapping. It is concluded that a 500 × 500 CCI with 1-mil center-to-center spacing between elements should achieve full geometric-limited resolution at about ten times starlight illumination, roughly comparable to that of the I-SIT tube.

1. Introduction

The charge-coupled device (CCD)[1,2] has provided a new approach for the design of self-scanned solid-state image sensors,[3-5] or charge-coupled imagers (CCI's). In addition to the obvious advantages of an all solid-state imager, calculations[6-9] indicate that the CCD is an inherently low-noise device, and it is expected that the CCI will be a sensitive imager with large dynamic range appropriate for low-light-level applications.

This paper presents an analysis of the expected resolution versus light-level capabilities of the CCI. It is concluded that noise arising

from trapping in fast interface states and shot noise due to the thermal generation of background charge should limit the sensitivity of CCI's and that their performance will lie somewhere between that of the I-SIT tube (intensified silicon intensifier target) and the silicon vidicon.
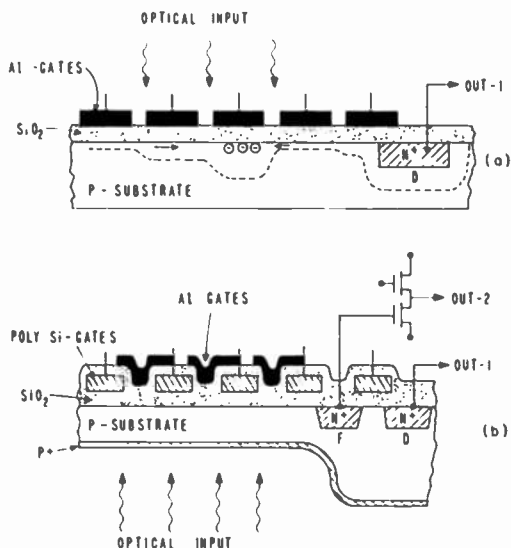
Fig. 1—Cross sectional view of (a) top (front) illuminated CCI and (b) back illuminated CCI.

2. Charge-Coupled Imagers

One can think of the CCI as the semiconductor equivalent of an electron-beam tube in which the charge signal can be *stored* and moved (transferred) under the control of the clock voltage pulses free of pickup and switching transients. The only limitations on the charge-coupling process come about because the charge transfer is not 100% complete. The finite transfer loss results in some distortion of the signal and introduces transfer noise. As will become apparent from the following description of known CCI arrays, the pickup from the clock voltages is limited to a single output stage.

Two general approaches for the construction of a CCI array are illustrated in Fig. 1. The optical input can be introduced from the top of the substrate through the spaces between nontransparent metal gates, as shown in Fig. 1(a). Top illumination of CCI's is also possible by transmitting the optical input through transparent gates such as

thin polysilicon. An alternate approach, illustrated in Fig. 1(b), consists of thinning the substrate in the optically sensitive area and applying the optical input from the back side of the substrate. Let us assume now that an optical input is applied to a CCD register while the clock voltages are adjusted so that one potential well is created at each stage along the CCD channel. With one of the phase voltages high, photogenerated charge will be collected and the stored charge pattern will represent the integrated light intensity pattern during this integration time. At the end of the integration time, the transfer action of the CCD is initiated by cycling the clocks, and the charge packets representing the light signal are shifted out to a single output detector and amplifier. To prevent smearing of the image, the optical integration time should be much longer than the total time required to transfer the detected image. The CCD is used to detect the light, store the resultant photogenerated charge, and scan or read out this charge pattern, and thus forms a line sensor. Arrays of adjacent line sensors can be used to make an area sensor.
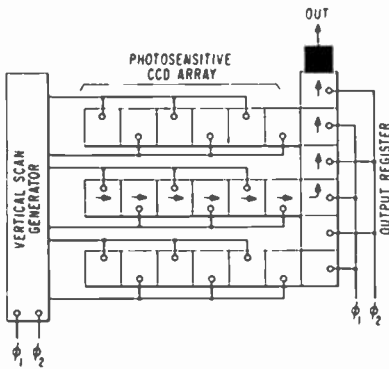
Fig. 2—Horizontal-line-transfer CCI.

Two basic systems have been proposed for constructing area sensors. One of these is the line-by-line horizontal read out system which has been built using a bucket-brigade transfer rather than CCD's.[10,11] This system is shown in Fig. 2. A vertical scan generator is used to sequentially apply the clock voltages to each horizontal CCD register in turn. The output of each horizontal register feeds a continuously running output register that transfers the signal to the output amplifier. Because of topological considerations, this system can be effectively implemented only with 2-phase CCD's. Assuming a square array of $N \times N$ elements with a 2-phase clocking system, this system

requires a maximum of $4N$ transfers since two gates are required for each element. If one frame is transferred each 1/30th of a second, then the clock frequency required is $30N^2$ Hz.
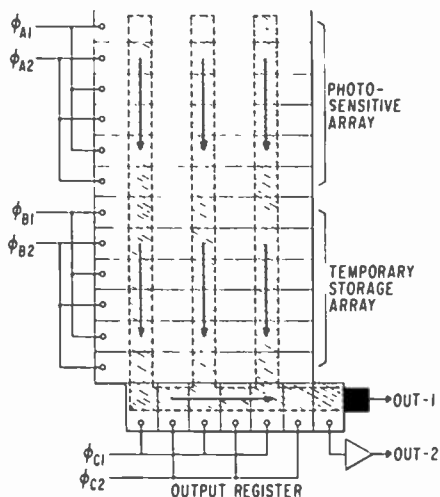
Fig. 3—Frame-transfer CCI with a temporary-storage array.

Another system that can be constructed with either a 3-phase or 2-phase clocking system is the frame transfer system with temporary storage.[3,12] A 2-phase version is illustrated in Fig. 3. In this system all of the signal charge in the photosensing array (top array) is shifted simultaneously into a temporary storage array (below) by clock-system-A during the vertical retrace time (900 μsec for normal TV raster). During the following integration period (1/30th of a second) the charge pattern in the temporary storage array is stepped down line-by-line by clock-system-B and each horizontal line is loaded in parallel into the output register. This line is then shifted out at high speed by clock-system-C to a single output amplifier. The operation of an $N \times N$ frame transfer system requires $2N$ vertical transfers and N horizontal transfers.

3. Noise Sources in CCD's

The noise introduced by any type of imager is very important, since it determines the sensitivity of the device and greatly affects the dynamic range. The CCI appears to be useful for low-light-level applications because the noise it introduces is expected to be rather low.

Following Reference 7, Table I is a listing of the expected noise sources in CCD's, along with the expected values for the rms fluctuation in the number of carriers per charge packet. Since CCD's are charge-packet shift registers with no gain mechanism (so that the same carriers remain essentially intact in the same packets throughout the entire transfer process), the rms fluctuation in the number of carriers in each packet, $\overline{N_n}$, has been used to quantify and compare the various

Table 1—Noise Sources in CCI's

Source	$\overline{N_n}$	Typical Values for $\overline{N_n}$
Photo-Electron Shot Noise	$\sqrt{N_s}$	25 for $C = 0.2$ and $S/N = 5$
Background Charge Generation Noise		
Thermal or Optical	$\sqrt{N_{s,o}}$	100 to 200
Electrically Introduced	$400 \sqrt{C_{pf}}$	40
Background Charge Incomplete Transfer Noise	$\sqrt{2\epsilon N_g N_{s,o}}$	200 for $\epsilon N_g = 0.2$ $N_{s,o} = 10^5$
Fast Interface State Trapping Noise	$[1.4 N_g (kT/q) N_{ss} A_g]^{1/2}$	950 for 2000 transfers $N_{ss} = 10^{10} (\mathrm{cm}^2 - \mathrm{eV})^{-1}$ $A_g = 10^{-6}\,\mathrm{cm}^2$
Output Amplifier Noise		
RC—Limited Bandwidth	$400 \sqrt{C_{pf}}$	1200 $C_{pf} = 10$
Reset—Floating Diffusion	$400 \sqrt{C_{pf}}$	120 $C_{pf} = 0.1$
Reset—Floating Gate	filterable	negligible
MOSFET (thermal)	$60\,C_{pf}$	~6

noise sources. Following Thornber and Tompsett,[9,13] CCD noise sources are divided into two general classes: storage process (SP) noise and transfer process (TP) noise. In our dicussion we will assume that the SP noise represents completely random and independent fluctuations between the charge packets. However, as pointed out by Tompsett[8] the TP noise in adjacent charge packets is not independent, since what is lost by one packet is gained by adjacent packets. This correlation of the TP noise flunctuation between adjacent charge packets must be taken into account when considering TP noise-limited operation of CCI's.

In CCI's the shot noise of the incoming photon stream is an example of SP noise. This noise source results in an rms fluctuation of $\sqrt{N_s}$, where N_s is the total number of photogenerated carriers in the charge packet. Since a background charge must be constantly circulated in CCD's to prevent losses into fast interface states,[14] this background charge will also contribute a SP fluctuation, depending upon the manner in which it is introduced into the potential well. If generated thermally, due to the dark current, it will have shot noise with rms fluctuation $\sqrt{N_{s,o}}$, where $N_{s,o}$ is the number of background charge carriers per packet. If $N_{s,o}$ is introduced electrically, the lower limit of the noise will be due to thermal voltage fluctuations, the resulting carrier fluctuation depends upon the capacitance of the potential well according to

$$\overline{N}_n = \frac{1}{q}\sqrt{kTC} = 400\sqrt{C_{pf}}. \tag{1}$$

where C_{pf} is the capacitance of the potential well in picofarads.

There are two sources of TP noise. One is due to a small fraction ϵ of the charge that is left behind at each transfer. On the average, $\epsilon(N_s + N_{s,o})$ carriers are left behind at each transfer with a mean-squared fluctuation about that average of $\epsilon(N_s + N_{s,o})$. In addition, since each packet gains or loses charge from the packet ahead, as well as gaining or losing charge to the trailing packet, at each transfer it suffers a mean-squared fluctuation of $2\epsilon(N_s + N_{s,o})$. Thus after N_g transfers, the rms fluctuation due to transfer loss is

$$\overline{N}_{n,\,\text{Transfer Loss}} = [2\epsilon N_g(N_s + N_{s,o})]^{1/2} \tag{2}$$

Another source of TP noise is that due to interface state trapping. As signals are shifted along the register, the interface states are periodically filling and emptying. While on the average they fill and empty to the same levels each period (if the signal level is constant), there is a fluctuation about this average. This mean-squared fluctuation is given by $(\ln 2)$ (kT/q) $N_{ss}A_g$ where N_{ss} is the density of fast interface states in $(cm^2 - eV)^{-1}$ and A_g is the area of one gate. Again a factor of 2 is required at each transfer; so after N_g transfers, the rms fluctuation due to interface state trapping is

$$\overline{N}_{n,\,\text{trap}} = [1.4(kT/q)N_{ss}N_gA_g]^{1/2}. \tag{3}$$

At low signal levels, this type of noise is expected to dominate for a large number of transfers, N_g.

Another possible noise source is the output amplifier. For an amplifier whose bandwidth is limited by the RC time constant at the input, there is a thermal noise associated with the input resistance that causes an rms carrier fluctuation of

$$\overline{N}_{n, \, RC \; \text{Amp}} = \frac{1}{q} \, (kTC)^{1/2} = 400 \sqrt{C_{pj}} \quad . \tag{4}$$

This type of noise limits the sensitivity of the silicon vidicon because C is on the order of 10-20 pF. The capacitance appropriate for a CCI with an amplifier integrated on the same chip is the gate capacitance of a MOSFET, which is on the order of 0.1 pF. In addition, the bandwidth of the integrated output amplifier of a CCI is not RC-limited, but rather is determined by the CCI clock frequency. In this case, the noise fluctuation due to the resetting of the floating diffusion can also be expressed by Eq. [1] where C is the effective capacitance associated with floating diffusion. This noise, however, presumably can be eliminated by resorting to charge sensing by a floating gate[7] that is reset once every frame time. Thus the noise associated with the output stage is expected to be small compared with the other noise sources discussed above.*

4. Analysis of Sensitivity and Resolution

The analysis presented in this section considers the effect of the CCI noise sources just discussed on the sensitivity and resolution of CCI's at low light levels. The basic criterion used in this analysis to determine the resolution versus light level capability is that the ratio of the number of photoelectrons to the number of rms fluctuations in that number per observable picture element (i.e., the signal-to-noise ratio) must exceed a certain number $k_{S/N}$. At any given image irradiance (the image irradiance is defined as the number of photons passing the image plane per second per cm²), the effective picture element area must be large enough to provide sufficient photoelectrons, or signal, to exceed the fluctuations by a factor of $k_{S/N}$. At high image irradiance levels, the picture element size can be small, but the minimum area is limited by the geometrical pattern of the CCD. Since the number of signal photoelectrons increases directly as the picture element area, but the fluctuations generally increase only as the square root of area, the signal-to-noise ratio increases as the picture element

---

* For more detailed discussion of the noise sources in CCD's see Ref. 7.

area increases. Thus, at low image irradiance levels, the observable picture element area becomes larger than the geometrical area; the number of observable TV lines per picture height decreases from the maximum determined by the geometrical pattern; and the resolution is noise-limited.

The fluctuations in the number of electrons per observable picture element fall into two general classes. First are uncorrelated, random noise sources such as the randon nature of the incoming photon stream, shot noise of thermally-generated charge, fluctuations in the number of fat zero electrons, and noise introduced by the output amplifier. The second class is correlated noise associated with the charge transfer process. In this case, for every charge fluctuation in one signal packet, there is an equal and opposite fluctuation in one of the adjacent signal packets. The transfer noise arises from the fluctuations associated with the transfer of the background charge as well as the detected signal charge and also from the trapping of charge by fast interface states.

If we assume that the active imaging area is square with a lateral dimension W_i, then the total number of observable TV lines per picture height L_{obs} is related to the lateral dimension of the effective picture element area W_e by

$$L_{obs} = \frac{W_i}{W_e}.$$

Since the minimum W_e is limited by the geometric center-to-center spacing of the CCI device W_g, the maximum or geometric TV lines resolution, is

$$L_{geom} = \frac{W_i}{W_g}. \tag{5}$$

The effective picture element area is

$$A_{eff} = W_e^2 = \frac{W_i^2}{L_{obs}^2} = W_g^2 \left(\frac{L_{geom}}{L_{obs}}\right)^2. \tag{6}$$

The number of photoelectrons per frame per picture element is

$$N_s = H_i \theta\, t\, A_{eff} \tag{7}$$

where

H_i is the image irradiance (photons/sec-cm^2)

θ is the quantum efficiency

t is the integration time or frame time.

However, the signal may only be a fraction of N_s if the scene contrast is low. If contrast is defined in the usual manner;

$$C \equiv \frac{\Delta N_s}{N_s},$$ [8]

where ΔN_s is the modulation of N_s, or signal, then the signal electrons per picture element is

$$\Delta N_s = CH_i \, t\theta \, A_{eff}.$$ [9]

Thus, using the criterion that the signal-to-noise ratio must be at least $k_{S/N}$ and using Eqs. [6] and [9], we have the following relationship between light level H_i and resolution L_{obs}:

$$\frac{\text{Signal}}{\text{Noise}} = \frac{\Delta N_s}{\overline{N}_n} = k_{S/N} = \frac{CH_i \, \theta t \, A_{eff}}{\overline{N}_n} = \frac{CH_i \theta t \, W_g^2}{\overline{N}_n} \left(\frac{L_{geom}}{L_{obs}}\right)^2.$$ [10]

Or, by rearranging,

$$H_i = \frac{k_{S/N}\overline{N}_n}{C\theta t W_g^2} \left(\frac{L_{obs}}{L_{geom}}\right)^2, \qquad L_{obs} \leqslant L_{geom}$$ [11]

The transition from geometry-limited to noise-limited resolution occurs when $L_{obs} = L_{geom}$. Note that since $W_g L_{geom} = W_i$, Eq. [11] indicates that in the noise-limited region for any given value of observable TV line resolution L_{obs}, the sensor with the larger active imaging area W_i^2 will be more sensitive, i.e., it will require a lower value of H_i. Quoted values for $k_{S/N}$ for random noise vary from 1.2 for a 14-bar test pattern[15] to 3 for a 100% contrast scene[16] to 5 for isolated disc patterns.[17] In this analysis we will use a $k_{S/N}$ value of 5 for the uncorrelated noise sources. However, the correlated noise sources associated with the charge-transfer process represent a new type of noise

in the context of determining imager resolution and we suggest that a $k_{S/N}$ value of 1 may be sufficient to provide a useable picture for the case of correlated noise sources.

4.1 Photon Shot Noise Limitations

As an instructive example of the uncorrelated noise let us consider the shot noise introduced by the incoming photon stream, a noise source not yet discussed but one which applies to the CCD imager, along with all image sensors, and represents the highest sensitivity possible.

Since the incoming photon stream is random with Poisson-distributed arrival times the fluctuations about the average number of detected photons N_s will be just $\sqrt{N_s}$. Thus if we denote the rms fluctuations in photoelectrons per picture element due to the randomness of the incoming photon stream as $\overline{N}_{n,\,\text{photon}}$, we can write

$$\overline{N}_{n,\,\text{photon}} = \sqrt{N_s} = (H_i t \theta A_{\text{eff}})^{1/2}. \tag{12}$$

If this were the only source of noise, then the resolution versus image irradiance relationship, Eq. [10], would become

$$H_{i,\,\text{photon}} = \frac{k_{S/N}^2}{\theta t\, C^2 W_g^2} \left(\frac{L_{\text{obs}}}{L_{\text{geom}}}\right)^2, \qquad L_{\text{obs}} \leqslant L_{\text{geom}} \tag{13}$$

While $k_{S/N}$, t, and C are parameters unrelated to sensor comparison, it is clear that sensors with the highest θ and largest $W_i = W_g L_g$ are capable of the most sensitive operation. The photoelectron limit for CCI's is low because the extended spectral response of the silicon (up to 1.1 μm) causes its quantum efficiency to be relatively high compared to standard photocathodes (S-1, S-20), especially in the starlight illumination condition which is relatively rich in near-IR photons. In particular, the S-20 quantum efficiency is approximately 50 times lower than silicon at starlight illumination levels. This difference is reduced as the light spectrum moves toward visible wavelengths.

For CCI's, using $\theta = 1$, $t = 0.1$ sec, $k_{S/N} = 5$, and assuming $W_g = 2.5 \times 10^{-3}$ (1 mil)

$$H_{i,\,\text{photon}} = \frac{4 \times 10^7}{C^2} \left(\frac{L_{\text{obs}}}{L_{\text{geom}}}\right)^2 \frac{\text{photons}}{\text{sec-cm}^2} \tag{14}$$

4.2 Background Charge-Transfer Noise

As an example of how the correlated noise is expected to affect the sensitivity and resolution of CCI's, let us consider the effect of the noise resulting from incomplete transfer of the background charge. Similar analysis should also be applicable for the other transfer noise sources. If $N_{s,o}$ is assumed to be the number of background charges in each geometric picture element, the rms fluctuations in each charge packet after N_g transfers will be

$$\overline{N}_n = [2\epsilon N_g N_{s,o}]^{1/2} \tag{15}$$

However, at low image-irradiance levels where the resolution is noise-limited, the fact that the transfer noise is correlated must be taken into account. As the observable picture element area A_{eff} becomes larger than the geometric picture element A_{geom}, the transfer noise fluctuations will cancel each other inside the observable picture element, and the only remaining noise fluctuations will come from the edges of the observable picture element. Since the observable element is being transferred along a given direction by the CCI, only the leading and trailing edges contribute fluctuations. There are L_{geom}/L_{obs} channels contributing a mean-square noise of $\epsilon N_{s,o}$ twice at each transfer, once at the leading edge and once at the trailing edge. Thus, the corresponding rms fluctuation due to the incomplete transfer of background charge after N_g transfers is given by

$$\overline{N}_n = \left[2\epsilon N_g N_{s,o} \frac{L_{geom}}{L_{obs}} \right]^{1/2}. \tag{16}$$

Using Eq. [11], we have

$$H_i = \frac{k_{S/N} \left[2\epsilon N_g N_{s,o} \dfrac{L_{geom}}{L_{obs}} \right]^{1/2}}{C\theta t W_g^2} \left(\frac{L_{obs}}{L_{geom}} \right)^2$$

$$= \frac{k_{S/N} [2\epsilon N_g N_{s,o}]^{1/2}}{C\theta t W_g^2} \left(\frac{L_{obs}}{L_{geom}} \right)^{3/2}. \tag{17}$$

Using a $k_{S/N}$ value of 1 because this is a correlated noise source, assuming $\epsilon N_g = 0.1$, $N_{s,o} = 10^5$, and values for the other parameters similar to those in Eq. [14], we have

$$H_i = \frac{2.2 \times 10^8}{C} \left(\frac{L_{obs}}{L_{geom}} \right)^{3/2} \frac{\text{photons}}{\text{cm}^2\text{-sec}} \qquad [18]$$

4.3 Resolution Versus Light Level

The effect of the other CCI noise sources on low light level capabilities can be determined in a similar manner using the various $\overline{N}_n$ values derived earlier. Table 2 lists the various noise sources and their rms fluctuation along with the H_i versus L_{obs} relationships that apply. The third column of the table shows the noise-limited image irradiance for signal-to-noise ratio of 5 for uncorrelated noise sources and 1 for correlated sources. The image irradiance H_i is expressed in terms of the ratio of L_{obs} to L_{geom} since the resolution becomes noise-limited when this ratio is less than unity. The transition between the geometric resolution and the noise-limited resolution in our analysis does not take into account the so-called Kell factor (~ 0.75) that is expected because of the discrete sensor elements of the CCI.

5. Expected Performance of CCI's at Low Light Levels

Fig. 4 shows the television lines per picture height versus image irradiance (L_{obs} versus H_i) for a 500×500 CCI with 1-mil center-to-center spacing. One curve is shown for each noise source, assuming that each acts alone. The total mean-squared noise, of course, is the sum of the individual mean-square contributions, so the total noise is only slightly larger than the largest contribution. In Fig. 4, the shot noise of the thermally-generated background charge (curve 7) ($N_{s,o}$ assumed to be 10^5) is the largest contribution and limits the sensivity of the device. Trapping due to fast interface states (curve 6) introduces a comparable amount of noise. A fast state density of $10^{10}(\text{cm}^2\text{-eV})^{-1}$ and 2000 transfers were assumed.

In Fig. 4, two noise sources associated with the introduction of background charge are shown — one for thermally-generated charge, the other for electrically-introduced background charge. Experimental evidence indicates that a background charge density (or fat zero) of 10% or more of a full well is required to reduce fast state losses to an acceptable level. At room temperature, the dark currents normally observed in CCI's (10 nA/cm²) are of the proper order or magnitude

Table 2—CCI Noise Source and Image Irradiance, H_i, versus the Observable Lines per Picture Height, L_{obs}.

Source	rms fluctuations per observable picture element, $A_{eff} = W_e^2 \left(\frac{L_{geom}}{L_{obs}}\right)^2$	Image irradiance for noise-limited resolution $\left(\frac{L_{obs}}{L_{geom}}\right) \leq 1$, signal-to-noise ratio k, and contrast C
Photo-electron shot noise	$[H_i \theta t A_{eff}]^{1/2}$	$H_i = \dfrac{k}{C^2 \theta t W_e^2} \left(\dfrac{L_{obs}}{L_{geom}}\right)^2$
Background Charge Generation noise Thermally-generated	$\left[\dfrac{J_d}{q} t W_e^2\right]^{1/2} \left(\dfrac{L_{geom}}{L_{obs}}\right)$	$H_i = \dfrac{k(J_d/q)^{1/2}}{C\theta t^{1/2} W_e} \left(\dfrac{L_{obs}}{L_{geom}}\right)$
Electrically-generated	$400\sqrt{C_{pi}} \left(\dfrac{L_{geom}}{L_{obs}}\right)$	$H_i = \dfrac{400k\sqrt{C_{pi}}}{C\theta t W_e^2} \left(\dfrac{L_{obs}}{L_{geom}}\right)$
Incomplete Charge Transfer Signal	$\left[2\epsilon N_s CH_i \theta t W_e^2 \dfrac{L_{geom}}{L_{obs}}\right]^{1/2}$	$H_i = \dfrac{25k\epsilon N_s}{C\theta t W_e^2} \left(\dfrac{L_{obs}}{L_{geom}}\right)^3$
Background charge	$\left[2\epsilon N_s N_{s,o} \dfrac{L_{geom}}{L_{obs}}\right]^{1/2}$	$H_i = \dfrac{k[2\epsilon N_s N_{s,o}]^{1/2}}{C\theta t W_e^2} \left(\dfrac{L_{obs}}{L_{geom}}\right)^{3/2}$
Fast Interface State Noise	$\left[1.4 N_s (kT/q) N_{ss} A_e \dfrac{L_{geom}}{L_{obs}}\right]^{1/2}$	$H_i = \dfrac{5[1.4 N_s (kT/q) N_{ss} A_e]^{1/2}}{C\theta t W_e^2} \left(\dfrac{L_{obs}}{L_{geom}}\right)^{3/2}$
Output Amplifier Noise Reset Floating Diffusion	$400\sqrt{C_{pi}} \left(\dfrac{L_{geom}}{L_{obs}}\right)$	$H_i = \dfrac{400k\sqrt{C_{pi}}}{C\theta t W_e^2} \left(\dfrac{L_{obs}}{L_{geom}}\right)$
MOSFET (thermal)	$60 C_{pi} \left(\dfrac{L_{geom}}{L_{obs}}\right)$	$H_i = \dfrac{60k C_{pi}}{C\theta t W_e^2} \left(\dfrac{L_{obs}}{L_{geom}}\right)$

to provide this background charge in 1/30 of a second. However, as we see in Fig. 4, this process is noisy and may limit CCI sensitivity.

However, if the CCI were cooled to suppress dark currents (factor of 2 reduction for every 10°C), then the background charge could be introduced electrically at the input of each register. Then Eq. [1] should govern the rms fluctuation in each packet and the capacitance of the potential well into which it is introduced should determine the noise. Since shot noise (rms) for 10^5 electrons is 316 and a capacitance of 0.1 pF would result in $400 \sqrt{0.1} = 126$, electrical introduction of background charge may provide more sensitive CCI operation.

If this were true, then fast interface state noise would be dominant. It is possible that buried channel CCD's,[18] which have a channel for charge transfer that is located away from the Si-SiO_2 interface and should be free of the deleterious effects of fast interface states, may provide, when cooled, very sensitive operation. Since no background charge is needed, such devices may be capable of photoelectron shot noise-limited operation (curve 3).
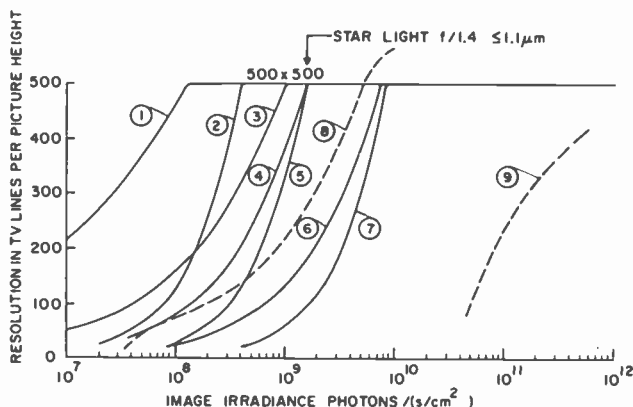
Fig. 4—Observable resolution in television lines per picture height versus image irradiance for 500×500 CCI with element spacing of 1.0 mil, frame time of 0.1 sec, quantum efficiency of 1.0, contrast of 0.2, and signal-to-noise ratio k. The various curves show the limits imposed by the various noise sources:

(1) Incomplete transfer of signal, $N_s = 625$, $\epsilon N_s = 0.2$, $k = 1$;

(2) MOSFET noise, $\overline{N}_n = 10$, $k = 5$;

(3) Photo-electron shot noise, $k = 5$;

(4) Transfer noise of elecrically introduced background charge, $N_{s,e} = 10^5$, $\epsilon N_s = 0.2$, $k = 1$;

(5) Storage noise of electrically introduced background charge $\overline{N}_n = 40$, $k = 5$;

(6) Fast interface trapping noise, $\overline{N}_n = 950$, $k = 1$;

(7) Thermally generated background charge noise, $\overline{N}_n = 200$, $k = 5$;

(8) Measured resolution for 40 mm I-SIT tube;

(9) Measured resolution for silicon vidicon.

Another source of noise that has not been considered in this analysis, but which we have encountered experimentally, is pulser noise. When the signal level is detected by means of a floating diffusion that is reset to a reference potential by capacitive coupling to one of the clock voltages (cf. Reference 19), any noise on the clock pulse due to amplitude or pulse width jitter is introduced at the output of the CCD. This is not a fundamental source of noise and should be avoidable by utilizing different schemes for sensing the output signal.

For comparison purposes, Fig. 4 also shows the measured performance of a 40 mm I-SIT tube and a beam-scanned silicon vidicon target. The I-SIT tube is limited by the photoelectron shot noise, but since the efficiency of the S-20 photocathode is about 50 times smaller than that of silicon for starlight illumination (which is relatively rich in near-IR photons), the I-SIT photoelectron limit occurs at higher image irradiance than the CCI photoelectron limit. The difference is not 50 because the total I-SIT area is larger than the 500×500 CCI area (1-mil centers) assumed. The silicon vidicon on the other hand is limited by the RC-limited output amplifier ($\overline{N}_n \cong 400 \sqrt{Cpf}$). The capacitance for the beam-scanned silicon vidicon is ~ 10-20 pF. Even with this limitation, the silicon vidicon is considered to be a very sensitive camera, especially when near-IR components are present in the incoming light.

It should be pointed out here that Fig. 4 assumes a 500×500 CCI array — beyond the present-day state-of-the-art. A smaller camera, say a 100×100 (but still with 1-mil spacing), has a smaller active imaging area and will not be as sensitive as the larger 500×500 device. On the other hand, a 1000×1000 array should be more sensitive than indicated in Fig. 4.

In summary, because the CCI has a low output capacitance, it is capable of more sensitive operation than the silicon vidicon. Based upon the analysis presented here, noise due to fast interface state trapping and generation and transfer of the background charge needed to suppress fast state losses will limit CCI sensitivity. If one could reduce fast interface states, CCI-type devices have the capability, when cooled, of surpassing I-SIT sensitivity because of the CCI's relatively higher quantum efficiency.

Acknowledgment

References:

[1] W. S. Boyle and G. E. Smith, "Charge-Coupled-Semiconductor Devices," **Bell System Tech. J.,** p. 587 (1970).

[2] G. F. Amelio, M. F. Tompsett, and G. E. Smith, "Experimental Verification of the Charge-Coupled Device Concept," **Bell System Tech. J., Briefs,** p. 593, April 1970.

[3] M. F. Tompsett, G. F. Amelio, W. J. Bertram, R. R. Buckley, W. J. McNamara, J. C. Mikkelsen, and D. A. Sealer, "Charge-Coupled Imaging Devices: Experimental Results," **IEEE Trans. Electron Dev.** Vol. ED-18, p. 992, Nov. 1971.

[4] W. J. Bertram, D. A. Sealer, C. H. Sequin, M. F. Tompsett, and R. R. Buckley, "Recent Advances in Charge-Coupled Imaging Devices," Digest of Technical Papers, 1972 IEEE International Convention, March 20-23, 1972, New York, p. 292.

[5] G. F. Amelio, W. J. Bertram, and M. F. Tompsett, "Charge-Coupled Imaging Devices: Design Considerations," **IEEE Trans. on Electron Dev.,** Vol. ED-18, p. 986, Nov. 1971.

[6] D. F. Barbe, "Noise and Distortion Considerations in Charge-Coupled Devices," **Electronics Letters,** Vol. 8, p. 207, April 20, 1972.

[7] J. E. Carnes and W. F. Kosonocky, "Noise Sources in Charge-Coupled Devices," **RCA Review,** Vol. 33, p. 327, June 1972.

[8] M. F. Tompsett, "The Quantitative Effects of Interface States on The Performance of Charge-Coupled Devices," to be published in **IEEE Trans. Electron Dev.**

[9] J. K. Thornber and M. F. Tompsett, "Spectral Density of Noise Generated in Charge-Coupled Devices," to be published in **IEEE Trans. Electron Dev.**

[10] M. G. Kovac, F. V. Shallcross, W. S. Pike, and P. K. Weimer, "Image Sensors Based on Charge Transfer by Integrated Bucket Brigades," International Electron Devices Meeting, Washington, D.C., October 11-13, 1971.

[11] M. G. Kovac, W. S. Pike, F. V. Shallcross, and P. K. Weimer, "Solid State Imaging Emerges from Charge Transport," **Electronics,** p. 72, Feb. 28, 1972.

[12] C. H. Sequin, et al., "A Charge-Coupled Area Image Sensor and Frame Store," to be published in **IEEE Trans. on Electron Dev.**

[13] J. K. Thornber, "Noise Suppression in Charge Transfer Devices," **Proc. IEEE,** Vol. 60, p. 1113, Sept. 1972.

[14] J. E. Carnes and W. F. Kosonocky, "Fast Interface State Losses in Charge-Coupled Devices," **Appl. Phys. Ltrs.,** Vol. 20, p. 261, April 1, 1972.

[15] J. S. Parton and J. C. Moody, Image Intensifier Symposium, Ft. Belvoir, Virginia, NASA SP-2, 1961.

[16] R. W. Engstrom and G. A. Robinson, "Choose the Tube—for L³TV," **Electro-Optical Systems Design,** p. 14, June, 1971.

[17] A. Rose, **J. Opt. Soc. Amer.,** Vol. 38, p. 196, 1948.

[18] R. H. Walden, et al., "The Buried Channel Charge-Coupled Device," **Bell Syst. Tech. J.,** Vol. 51, p. 1635, Sept. 1972.

[19] W. F. Kosonocky and J. E. Carnes, "Charge-Coupled Digital Circuits," **IEEE J. Solid-State Circuits,** Vol. SC-6, p. 314 (1971).

A Television-Rate Laser Scanner
I. General Considerations

I. Gorog, J. D. Knox, and P. V. Goedertier

RCA Laboratories, Princeton, N.J.

Abstract—A television-rate laser raster scanner is described. This scanner util-
izes an acousto-optic Bragg cell as the fast horizontal deflector and
either a rotating refractive prism or a galvanometer as the vertical de-
flector. The beam-shaping and image-forming optics, the electronic
system, and the major deflection components are discussed in detail,
and experimental results are presented. Also, a detailed treatment of
the frequency response of scanning beams is included.

1. Introduction

Virtually all laser systems require some form of laser beam deflection,
including communications systems where beam deflection (or steering)
is necessary for accurate tracking of the receiver, and laser machining,
where precise beam positioning will be needed in automated cutting,
trimming, and drilling equipment. Of course deflectors are key com-
ponents in all image display, recording, and pick-up systems.

To date the deflectors employed in most operational laser systems* are based on moving mirrors. For fast, sequential scanning, high-resolution imaging systems, many-faceted rotating mirrors are employed;[1-6] for slow random-access applications, galvanometers and piezoelectrically driven tilting mirrors are available.[7-10] Research models of deflectors utilizing practically all known strong optical interactions have been constructed. The two methods currently believed to hold the most promise are the digital electro-optic deflector,[11-15] which utilizes the electric field-dependent index of refraction in certain materials, and the acouto-optic Bragg deflector,[16-27] which uses the diffraction of light by sound. The electro-optic method is well suited for expensive, fast, random-access applications, but will be unlikely to find application where lower cost sequential scanning is needed. The acousto-optic Bragg method is very well suited for sequential scanning and is also applicable to intermediate-speed random-access systems (approximately 10 microseconds access time for any one of 10^6 beam positions is an achievable goal).

Of the above two methods the Bragg technique promises to find the wider range of applications. We believe that acousto-optic deflectors are here to stay, and that they will become the basic work horse of all scanning systems operating in approximately the 0.1 to 100 kHz scan line repetition rate range. We have constructed all of our experimental apparatus to operate at television rates. Our general aim, however, is to learn to manipulate light beams with the same ease as we now do electron beams; laser-beam technology is probably about as well developed today as electron-beam technology was in the pre-television days.

Even though large-screen multicolor laser projection television has been mentioned by a number of authors as the important application for sequential scanners, we believe it is only one of many potential uses and probably one of the more uncertain ones. The reason for this conclusion is that we expect that: (1) efficient cw generation of monocolor visible laser light will be achieved by harmonic up-conversion from the near infrared, but that multicolor generation will not be achieved with anywhere near the efficiency and simplicity of monocolor, (2) safety considerations will complicate the widespread (i.e., home) use of high-power (multiwatt) scanned laser beams, and (3) other, more suitable techniques will be developed.

In Table 1 we have listed some of the likely applications for laser scanners, mostly in the image-display, recording, and pickup areas.

---

* By "operational systems" we mean systems that perform a useful function beyond the demonstration of a potentially useful concept.

As this list indicates, we expect that low-power scanned lasers will find wider use than high-power lasers. For purposes of display, various laser-addressed light valves will be developed, and these devices will have a strong impact on large-screen displays. We have concluded that

Table 1—Laser Scanner Applications (D = Display, R = Recording, P = Pickup)

1—Laser-addressed light valve (D)
2—Laser-addressed light amplifier/image intensifier (D)
3—Special displays that require holo-lenses (e.g. "head-up display") (D)
4—Large-screen laser display (D)
5—Laser recording (R)
6—Heat printers with scanned IR lasers (R)
7—Computer print-out (R)
8—Scanned optical microscope (P)
9—Laser image scanner (P)
10—Low-light-level scanned TV pick-up (P)
11—Scanned optical radar (P)
12—Beam tracking in optical communication systems
13—Industrial control systems
14—Manufacturing operations (cutting, trimming, etc.)—mostly IR and pulsed
15—Materials testing (P)
16—Optical mask preparation (R)
17—Laser-scanned orthicon type pick-up tubes (P)
18—Optical memories and image stores

Laser-addressed light valves examples:
    Photo-emitter controlled
        Electro-optic crystal (KDP, $Bi_{12}SiO_{20}$)
        Thin membrane schlieren
    Photoconductor controlled:
        Ferpic (E.O. ceramic PLZT)
        Liquid crystal
        Surface deformable media (thermoplastics, oil films, elstomers)

incoherent-light-controlling valves that use a 1-milliwatt laser source as the valve addressing means could be developed now. This 1-milliwatt source requirement takes into account currently achieved modulator and deflector efficiency and measured reversible medium (thermoplastic) exposure sensitivity.

In this paper we describe in some detail the results of the first phase of our deflector program, namely the construction and operation of a real-time television-rate laser scanner. This scanner utilizes an acousto-optic Bragg device as the fast horizontal deflector and either a novel refractive rotating device or a galvanometer as the vertical deflector. A beam-shaping, focusing, and image-forming lens system that allows compact construction has been designed. The system ac-

cepts standard TV modulation and deflection signals and has greater than 500-line vertical and 5-MHz horizontal resolution.

This paper is in four parts. After the introduction we describe the deflection system. In the next part the major deflection components are treated. In the final part the general problem of the frequency response of scanning beams is discussed. This discussion includes both intensity-modulated and velocity-modulated beams. A general quantitative formulation of the connection between the spread function of a scanning beam and its frequency response is presented and a number of specific examples are treated. The results provide useful guidelines for specifying scanners for given applications.

2. Deflection System

2.1 General Comments

This paper describes a laser raster scanner capable of operating at standard television rates. The main areas of potential applications are information display, recording, and generation. An outstanding feature of laser scanners is their versatility; for a given scanner, the scan mode (e.g., jump scan, sequentially scanned raster, etc.) and the scan rate are the basic specifications on which the design depends. Raster size is of secondary concern, and the overall optical efficiency is independent of it. Also, the resolution, expressed either as the number of resolvable points per frame, or as the video frequency response, is a constant of the system, and is essentially independent of the image size. Our scanner, for example, produced a large-screen (approximately 3 foot by 4 foot) television display; also, when passed through microscope optics, it operated as a television read-out scanning laser microscope. This paper is restricted to the description of the scanner; details of the applications experiments will be published later.

The hybrid scanner configuration was chosen. For the fast horizontal scanning, an acousto-optic deflector, operating in the "transition region" (see Section 3.1) is used. For the vertical deflection, either a rotating refractive prism polygon or an oscillating galvanometer-driven mirror is employed. Operation in the acousto-optic transition region allows sweeps over an acoustic bandwidth sufficiently wide for TV resolution, with approximately 50% optical efficiency, without use of phased-array transducers. The electromechanical vertical deflectors provide essentially 100% deflection efficiency, are potentially inexpensive, and require simple drive signals.

The choice of the acousto-optic material was based on two considerations: In addition to high diffraction efficiency, a small optical

aperture in the deflector is also desirable. (The smaller the aperture, the easier and cheaper it is to obtain diffraction-limited operation along the optical chain.) Therefore, in order to maintain the required resolution, one must operate at the highest possible frequency. Thus, single-crystal acousto-optic materials must be employed. Using a lead molybdate deflector with 0.85 cm aperture, a complete, diffraction-limited raster scanner that has a 30 cm over-all optical length (unfolded physical length) was developed. This length included the beam expander and the complete x and y deflection optics, with the necessary beam-shaping, image-forming, and projection lenses. No special lens designs were required; all the lenses employed are of average quality, but are operated at sufficiently small numerical aperture to allow diffraction-limited operation.

2.2 Optical System

We have designed and tested two hybrid deflection systems, each capable of operating at real time with a full 5-MHz horizontal TV resolution and a vertical resolution of 1000 lines. Both systems derive their fast axis scanning with an acoustic Bragg deflector; they differ only by the means in which they achieve vertical deffection; one employs a rotating polygon, the other uses a scanning mirror galvanometer. Both of these electromechanical deflectors are capable of high resolution and efficiency, and are quite adequate for the slow-axis scanning. Naturally, the assets and liabilities of each electromechanical deflector dictate selection for a given application.

The deflection optics used in the laser address system include a unique lens chain that must perform a number of beam-shaping and image-forming operations to realize the full performance capabilities of the horizontal and vertical deflectors contained within it. This optical system was developed according to the following design criteria:

(a) proper beam shaping to optimize the apertures of the acoustic deflector and electromechanical deflectors,

(b) diffraction-limited performance and accommodation of large-aperture (up to 2.5 cm) acoustic deflectors by the optical lens chain,

(c) adjustability of the aspect ratio of the scanned raster,

(d) correction for the cylindrical astigmatism exhibited by the frequency-swept acoustic deflector,

(e) compactness (about 30 cm in length or less),

(f) simplicity and ease of alignment,

(g) use of simple lenses of average quality.
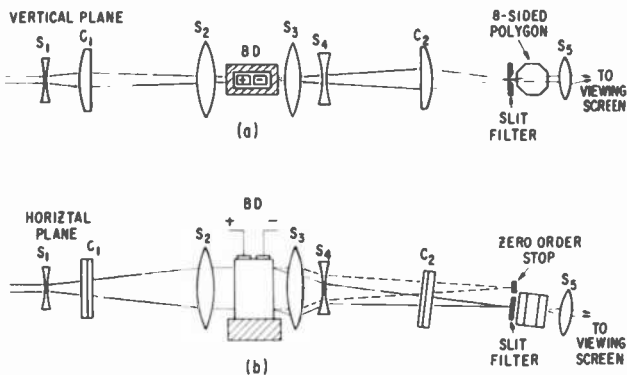
Fig. 1—Complete deflection optics incorporating an acousto-optic horizontal deflector and a rotating refractive prism polygon vertical deflector.

In the above listing, conditions (a) through (d) are necessary only to demonstrate feasibility of performance of the laser deflection system; conditions (e) through (g), however, are necessary to render it practical.

In the following discussion a complete description of the deflection optics is given, along with the design considerations necessary to stay within the above-stated guidelines. Fig. 1 shows a schematic diagram of the deflection optics (including the complete beam-shaping and image-forming lens chain) including the acoustic deflector and the 8-sided rotating polygon. A similar diagram is shown in Fig. 2 for the scanning mirror galvanometer. In the two systems, the "front-end" optics, up to and including the second cylinder lens, C_2, are identical, and thereafter differ only to accommodate the respective electromechanical deflectors.
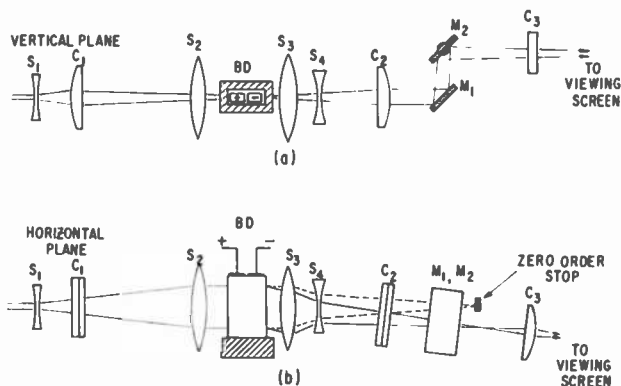

Fig. 2—Complete deflection optics incorporating an acousto-optic horizontal deflector and a galvanometer-type vertical deflector.

The first three elements, S_1, C_1, and S_2, in the lens chain (see Figs. 1 and 2) serve a number of functions, but, in essence, are used to transform the input laser beam from a small circular cross section into a large elliptical cross section in order to accommodate the long but narrow rectangular aperture geometry of the acoustic deflector. Thus we flood the aperture of the acoustic deflector, thereby obtaining its optimum deflection efficiency and resolution.

This three-lens arrangement is basically a beam expander with a cylindrical lens, C_1, inserted in the middle. Thus, as can be seen from Figs. 1 and 2 the beam expands in the horizontal direction to fill the large aperture dimension of the acoustic deflector; in the vertical direction, the cylindrical lens focuses the light through its narrow width.*


$$f'/f = 1 - \frac{D}{f_1}$$
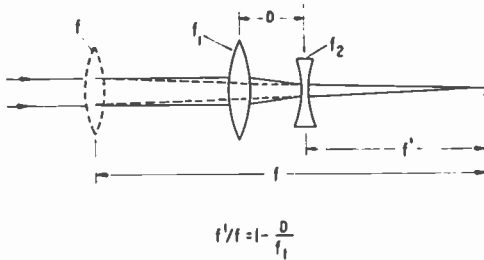
Fig. 3—The telephoto optics (lens combination S_x and S_4 on Figs. 1 and 2) and its equivalent lens of focal length f ($f = f_1 f_2 / [f_2 - f_1 + D]$), where f_1 and f_2 are the focal lengths of the positive and negative lenses, respectively).

The positive and negative lens arrangement, S_3 and S_4, immediately following the acoustic deflector is a telephoto system that gives a long focal length over a short physical distance (see Fig. 3). This long focal length is required to provide sufficient magnification of the scanner image before it is projected onto the viewing screen. The telephoto arrangement is an important design consideration for compactness when using the in-line-optics rotating polygon (Fig. 1). However, for the galvanometer (Fig. 2), which offers a natural folded-optics arrangement, the telephoto system is not always needed.

The second cylindrical lens, C_2, following the telephoto arrange-

---

* This narrow rectangular aperture geometry of the acoustic deflector is a design consideration aimed at obtaining maximum resolution and deflection efficiency for a given acoustic drive power input. (See discussion on acoustic deflectors). A further narrowing of the useful aperture is caused by cracks and cleavages frequently introduced during the bonding of the acoustic transducers to the deflector crystal.

ment, provides the final beam convergence necessary for the efficient operation of the electro-mechanical deflectors. For the rotating polygon (Fig. 1), it means a large beam convergence angle for maximum resolution but a small beam diameter upon entering the rotating polygon to optimize its built-in blanking capabilities. For the scanning mirror galvanometer, the second cylindrical lens provides a small convergence angle in order to flood the galvanometer aperture, thus obtaining its full resolution capabilities. (Note the difference in forward displacement of C_2 in Fig. 1, relative to that in Fig. 2.)

The last lens in the optics chain projects the scanned image onto a viewing screen. Its focal length determines the actual physical size of the scanned raster.

The deflection optics shown in Figs. 1 and 2 operates with small numerical apertures; thus, for all practical purposes, it guarantees diffraction-limited operation and ease of alignment. In addition, a spatial filter in the form of a narrow slit can be inserted in the back focal plane of the projection lens S_5 in Fig. 1 to filter out any undesirable spatial frequencies due to cylindrical lens aberrations, which tend to degrade the picture quality. Also, all of the lens elements are simple and of average quality. The overall length of the deflection optics is about 30 cm; with folding and appropriate choice of lens parameters, this length can be further reduced.

The aspect ratio of the scanned raster can be adjusted in both deflection systems by adjusting the bandwidth of the rf drive of the acoustic deflector. The scan angle of the galvanometer can also be adjusted to offer further flexibility of aspect ratio adjustment.

Finally, when the acoustic deflector is operating in a sequential scanning mode in response to a strictly linearly swept rf input, it exhibits a phenomenon known as cylindrical astigmatism.[28]. In effect the acoustic deflector behaves like a long-focal-length (15-20 meters) cylindrical lens. The equivalent cylindrical lens focal length is $f = v^2 T / (\lambda \Delta \nu)$, where v is the sound velocity in the acoustic medium, T is the linear sweep time duration, λ is the light wavelength in air, and $\Delta \nu$ is the change in acoustic frequency during the sweep. Note that $\Delta \nu$ can be either positive or negative, depending on the sweep direction. Therefore, if the sweep direction is reversed, the optics must be refocused. With the cylindrical lenses incorporated into the deflection optics (which decouples the horizontal from the vertical focus), a small forward or backward displacement will correct for the astigmatic effect.

2.3 Electronic System

The block diagram of the electronic system used to process the laser beam into a video display is shown in Fig. 4. The electronic system

is designed to be operated with a standard monochrome video signal; the required control pulses are composite blanking, horizontal drive, and vertical drive. The video chain consists of a processing amplifier, a video amplifier and dc restorer, and a dc-coupled modulator drive amplifier. The deflection circuits consist of various waveform processors and signal generators needed to drive the scanners linearly within the retrace times set by television standards.
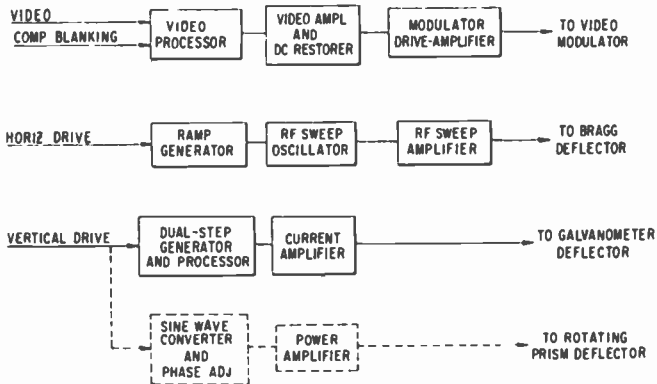
Fig. 4—Block diagram of the electronic system.

While the general outline of this electronic system is similar to that used in processing an electron beam in a CRT display, the various waveforms and signal levels needed are substantially different from their CRT counterparts. In the following discussion we give a functional description of the main building blocks of the electronic circuitry.

a. The Video Chain

The incoming composite video signal is first fed to the video processor. The video processor reconstructs the pure video signal from the composite video, provides an optional polarity-inversion capability, and should include gamma-correction capability. (The present system is not equipped with gamma correction). The modulator drive amplifier is a commercially available dc-coupled video amplifier designed specifically to drive the transverse electro-optic modulator. The observed frequency response of the complete video chain, from composite video input to a laser beam detector output, extends from dc to well over 5 MHz.

b. Horizontal Deflection

The highest-resolution performance of the lead molybdate acousto-optic deflector was achieved when its rf drive was swept linearly from 125 to 250 MHz. The nominal input impedance of the deflector transducer is 50 ohms and the required rf drive power level is one to three watts.

The sweep signal was generated by a commercially available sweep generator and a wideband-compensated distributed amplifier capable of delivering 3 watts at 1 dB compression into a 50-ohm load.

The poor impedance match of the transducer over the wide bandwidth necessitated the use of some padding between the deflector and the amplifier. The actual power reaching the transducer was therefore approximately 1.5 watts maximum.

c. Rotating-Prism Scanner

The rotating prism is mounted on the shaft of a 60-Hz series hysteresis synchronous motor that requires approximately 20 watts of drive power. The sinusoidal drive signal, synchronous with the field rate, is obtained from a symmetric multivibrator that is triggered by the vertical blanking pulses. The output of the multivibrator is passed through an L-C filter and then fed to a 20-watt audio amplifier. In order to match exactly the scanner retrace time with the vertical blanking interval, an adjustable phase-shifting network is included between the sine-wave generator and the audio amplifier.

d. Galvanometer Scanner

When a fast galvanometer is driven by a television-field-rate ramp signal, the galvanometer's high mechanical Q results in overshoot and ringing at the end of the retrace. Ringing-free retrace, however, can be achieved by applying the retrace current in two precisely timed steps. The first step, applied at time t_1, which corresponds to the beginning of the retrace, reverses the angular motion of the galvanometer and drives it to the opposite extreme position in a time interval equal to approximately one half of a period of the free oscillation of the mechanical system. At time t_2 the galvanometer comes to rest. If the initial retrace pulse were the only driving force, the coil would again reverse its motion and complete a second half of its ringing cycle. Exactly at time t_2, however, a second current step is applied to the coil. The height of this step is carefully adjusted so that at time t_2 the driving force precisely cancels the restoring force. There-

fore the galvanometer remains stationary at its extreme position. At time t_3 the linear ramp is initiated and the galvanometer begins its forward sweep.

An electronic processor was designed to generate the desired functions. Two monostable multivibrators, triggered at field rate by the vertical drive pulses, generate two pulses of duration $t_2 - t_1$ and $t_3 - t_1$,
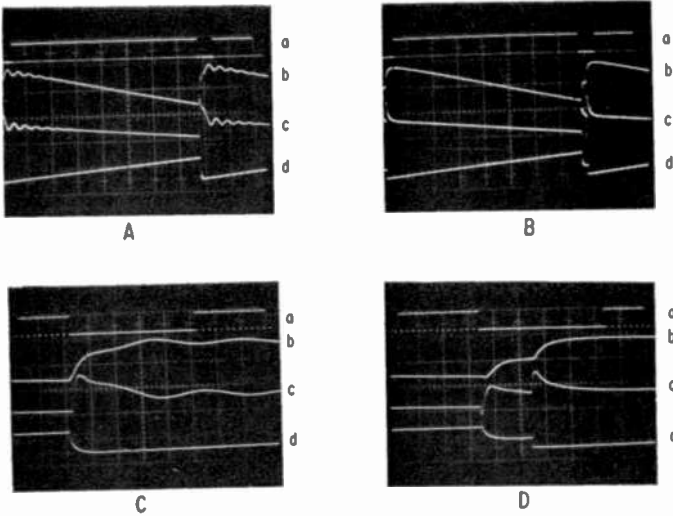

Fig. 5—Performance of the galvanometer drive signal processor. Figs. A and C show retrace without special processor, B and D show retrace with processor. Trace a is the blanking pulse, b is the galvanometer coil current, c is the voltage across the galvanometer coil, d is the open circuit drive voltage. (Horizontal scale on A and B is 2 milliseconds per major division; on C and D it is 0.24 millisecond per major division).

respectively. After proper level adjustment, the sum of these two pulses provides the required two-step retrace pulse. The linear forward ramp is generated by integrating the pulse train composed of the $t_3 - t_1$ duration pulses. Best linearity with a galvanometer type deflector is obtained when the armature shaft swings symmetrically about its zero torque angular position; the adjustable dc bias, also provided by the processor, assures this mode of operation.

The performance of the processor is illustrated in Fig. 5. Oscillograms A and B show a complete television field, while C and D are expanded to illustrate the wave shapes during vertical retrace. Oscillograms A and C show the performance without the special two-step retrace drive signal processor; B and D show the performance with it. On all four oscillograms trace "a" is the blanking pulse, "b" the

galvanometer coil current, "c" the voltage across the galvanometer coil, and "d" is the open-circuit drive voltage. The electrical impedance of the galvanometer depends on its mechanical angular velocity; therefore, mechanical ringing results also in electrical ringing. Note the clean ringing-free fast retrace performance obtained with the two-step retrace drive pulses shown on oscillograms B and D. Also note that the retrace is completed in approximately one half the blanking time and that the linear forward sweep is achieved well before the end of the blanking period.
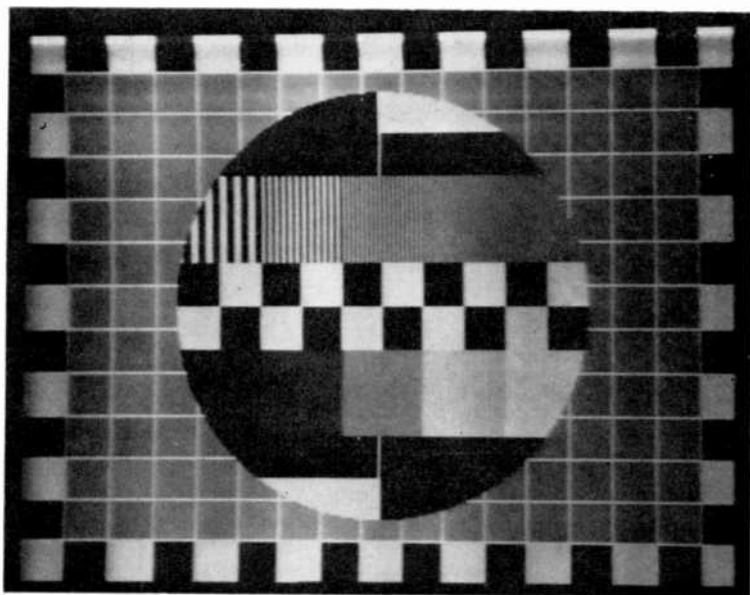
Fig. 6—Monochrome television test pattern displayed by the laser scanner, using a galvanometer vertical deflector.

2.4 Results

The performance of a laser scan system using lead molybdate acousto-optic horizontal deflectors and galvanometer vertical deflectors is shown in Fig. 6. Using the 4880-Å argon laser line, the standard monochrome television test pattern was scanned onto a color-converting organic phosphor screen, and the resulting black and yellowish white display was photographed. The apparent slight skew is the result of the off-axis camera location; the actual display was completely free of such distortions. The theoretical horizontal resolution, as determined by the acousto-optic device, was 282 Rayleigh spots, with 52 microseconds

active line time, corresponding to a limiting horizontal TV resolution of 5.4 MHz (i.e., the straight-line MTF rolls off to zero at 5.4 MHz, see Section 4). Careful inspection of the frequency bursts in Fig. 6 (corresponding to 1, 2, 3, 4, and 5 MHz) indicates a limiting resolution of approximately 5 MHz. The vertical resolution is approximately 1,000 lines; the actual TV raster lines were fully resolved over the entire field. The overall linearity of the scanned pattern was estimated to be better than 3%.

The photographed test pattern clearly indicates some small but definitely noticeable brightness nonuniformities that stem from a number of sources. First, there is a slow center-to-edge brightness variation in the horizontal direction; it is caused by a combination of Bragg roll-off and transducer roll-off. The Bragg roll-off is discussed in some detail in the section on acousto-optic deflectors. The transducer roll-off is caused by the frequency-dependent efficiency of the acoustic transducer. Experimentally, we found that the intensity variations due to Bragg roll-off and to transducer roll-off were comparable. By proper adjustment of the Bragg angle, approximately 35% center-to-edge roll-off was obtained. The second major source of brightness variation is the frequency-dependent electrical impedance of the acoustic transducer; it causes a number of bright vertical stripes to appear on a uniform "white field" display. With most subject matters, however, these vertical stripes are not very noticeable. The best long-term stability of the galvanometer deflector was obtained when the drive pulses allowed some ringing, which causes the slight vertical intensity variation at the upper edge of the raster. Finally, some bright areas are caused by the nonuniform phosphor coating of the display screen.

Fig. 7 shows the performance of the laser scanner with a "typical" subject. This picture was taken under the same conditions as Fig. 6.

Fig. 8 shows the test pattern, but here the vertical deflection was accomplished by an 8-sided fused-silica rotating refractive prism (approximately 2.5 cm diameter). In all other respects the arrangement was the same as that used for Fig. 6.

A few preliminary experiments concerning the effects of various viewing screens on the performance of a laser display were also performed. We found that using directional projection screens, a 0.5-W laser, at 5145 Å, with 10% overall optical efficiency, produces a highly visible display on a 3×4-foot screen. A major problem with this type of a display is speckle noise. From a convenient viewing distance (approximately 6 feet), the speckle noise killed information above approximately 3 MHz. When a reflective screen is coated with an ap-

Fig. 7—"Typical" test subject displayed by the laser scanner, using a galvanometer vertical deflector.
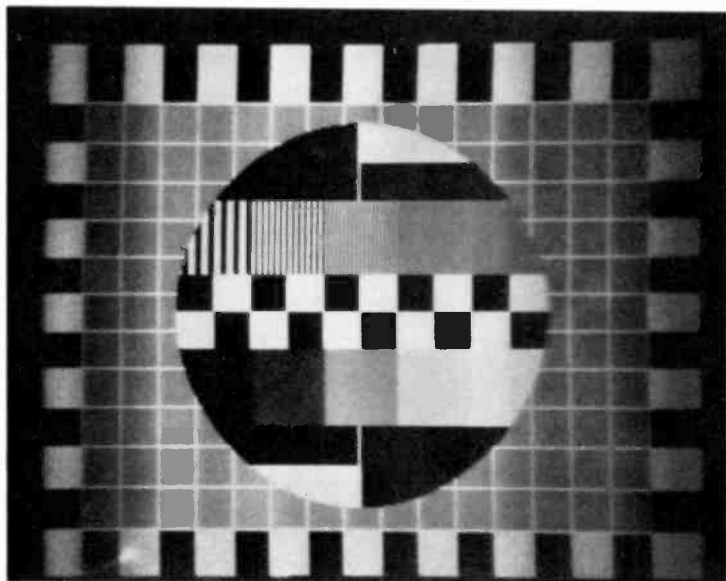

Fig. 8—Monochrome television test pattern displayed by the laser scanner, using a rotating refractive prism polygon vertical deflector.

propriate photoluminescent phosphor, the speckle noise is completely eliminated. Also, the screen may provide luminous gain. Furthermore, special phosphor screen designs may be used to create a color display using a monochrome laser scanner. Our experiments have thus far been limited to handling monochrome information, but all of our experimental results made use of the speckle-suppressing and color-converting properties of such phosphor screens.

3. The Deflection Components

3.1 Acousto-Optic Deflectors

The most convenient method of achieving fast linear scanning of laser light for analog-signal-handling applications is by means of acousto-optic deflectors.[17,18] In an acousto-optic device, light deflection is achieved through diffraction of light by sound-pressure-produced refractive index variations.

Assume that the index of refraction variation in the medium is described by $n(x,t) = n_o + n_1 \sin(\Omega t - Kx)$, where Ω and K are the angular frequency and the wave number of the sound, respectively. When a plane wave of light with wavelength λ is incident on the variable-index medium, the amplitudes of the various diffraction orders, for $\lambda/n_o \ll \Lambda = 2\pi/K$, are related by a set of coupled difference differential equations.[19] In general, this set of equations can only be solved numerically. A number of such numerical solutions is available.[19,20] Dependent on a set of interaction parameters, the solutions, and the corresponding devices, can be separated into three classes. The pertinent parameters are

$$\Delta\phi = k n_1 L, \qquad\qquad [1]$$

$$Q = \frac{K^2 L}{n_o k}, \qquad\qquad [2]$$

$$\alpha = -\frac{n_o k}{K} \sin\theta, \qquad\qquad [3]$$

where $k = 2\pi/\lambda$, L is interaction length (the width of the sound wavefront in the plane formed by $\vec{k}$ and $\vec{K}$), and θ is the incidence angle. (The angle between $\vec{k}$ and $\vec{K}$ is 90-θ.) The first interaction parameter, $\Delta\phi$, describes the x-dependent phase shift; the second one, Q, is the

normalized interaction-length parameter and α is a normalized angle parameter.

In the region $Q \ll 1$, the sound field acts like a thin grating and the first-order diffraction intensity I_1, is given by

$$I_1 = I_0 J_1(\Delta\phi), \qquad [4]$$

where I_0 is the incident intensity and J_1 is the Bessel function first kind, first order. The maximum diffraction efficiency, from Eq. [4], is 34%. The diffraction efficiency is entirely independent of α. Therefore, in this region, as long as a constant phase shift is maintained, the diffraction efficiency is also independent of Λ.

The region $Q \gg 1$ is called the Bragg region. Light is diffracted only when θ equals the Bragg angle, $|\alpha| = 0.5$, and only one diffraction order exists. Then the diffracted intensity is given by

$$I_1 = I_0 \sin^2\left(\frac{\Delta\phi}{2}\right). \qquad [5]$$

The deflection efficiency can reach 100%. Devices operating in this regime are very sensitive to angular alignment. In order to assure efficient operation over a wide band of acoustic frequency, phased-array acoustic transducers must be employed.[20,21]

The region $1 \leq Q \leq 10$ is called the transition region. There is no known analytical solution in this regime and no simple scaling laws exist. The available numerical solutions, however, suggest that this region is the most useful one for light-deflection applications. Its main features are: the first-order diffraction efficiency is high, the sensitivity to angular misalignments is low, and more than one diffraction order is present. The presence of higher diffraction orders restricts operation to one-octave rf bandwidth. (If greater than an octave sweep is employed, the low-frequency end of the second-order spectrum overlaps the high-frequency end of the first-order spectrum.) The roll-off of the diffracted intensity with changing acoustic frequency (i.e., the variation of I_1 with respect to α) is sufficiently low to allow an octave operation. For example[19] with $Q = 10$ and $\Delta\phi = 2.0$, the calculated roll-off from band center to edge with an octave bandwidth is approximately 25%; the center of the band occurs at $\alpha = 0.5$ and, at the center, approximately 67% of the incident light is deflected. With $Q = 10$ and $\Delta\phi = \pi$ at $\alpha = 0.5$, over 90% of the incident light is deflected. In general, for any given Q and given acceptable roll-off, the

smaller $\Delta\phi$ is, the larger is the allowed bandwidth. Also, for $Q > 10$, the diffraction efficiency at $\alpha = 0.5$ is well approximated by Eq. [5].

From the above we conclude that an acousto-optic cell with $Q \simeq 10$ offers a good design compromise for deflection applications. For $Q \ll 10$, the deflection efficiency is low but the angular tolerance is excellent; for $Q \gg 10$, the diffraction efficiency is high, but, because of the small angular tolerance, either the operation is restricted to a narrow band of acoustic frequencies, or a phased-array acoustic transducer arrangement is required.

All of our experiments to date were performed with deflectors using lead molybdate as the acousto-optic medium.[22] The construction of our device was identical to that described in Ref. (22).* The longitudinal sound waves were propagated in the c direction. Then the sound velocity[29] is 3.6×10^5 cm/sec, and from Eq. [2] we find that at 150 MHz with 5,000-Å light ($n = 2.48$),[29] and $L = 1$ cm, $Q \simeq 20$. The required sound power can be estimated from the well-known relationship[30]

$$\Delta\phi = \pi \sqrt{\frac{2}{\lambda^2} \frac{L}{W} M_2 M_s P_{ac}}, \qquad [6]$$

where W is the acousto-optic cell dimension perpendicular to both the light- and the sound-wave propagations, M_2 is the relative acousto-optic figure of merit, $M_s = 1.51 \times 10^{-18}$ sec³/g is the acousto-optic figure of merit for fused silica,[22] and P_{ac} is the sound power. For our device $L = 1.0$ cm, $W = 0.5$ cm, $\lambda \simeq 5000$ Å, $M_2 \simeq 25$ and therefore maximum deflection efficiency ($\Delta\phi = \pi$) occurs with $P_{ac} = 1.5$ watts.[23] Experimentally we have observed approximately 60% diffraction efficiency with 3 watts rf drive power. (We conclude, therefore, that our transducer losses were approximately 6 dB.)

The diffraction-limited resolution of an acousto-optic deflector is given by

$$N = \Delta f \tau, \qquad [7]$$

where Δf is the bandwidth of the swept-frequency sound waves and τ is the transit time of the sound waves across the optical aperture.[21] In our deflector the useful optical aperture was 0.85 cm, and with a subjectively acceptable roll-off, we operated over a 125-MHz bandwidth. The diffraction-limited resolution was therefore $N = 282$ spots.

3.2 Electromechanical Deflectors

a. Rotating-Mirror Polygons

Electromechanically driven reflective and refractive optical elements are the highest-resolution optical deflectors known. The simplest and most commonly used deflector of this type is the rotating polygon with polished mirror facets. Its ultimate resolution capability is determined by the mechanical strength of the available materials. As the polygon is rotating, each facet scans out a line. Therefore a polygon with v facets, rotating at M revolutions per second, scans out vM lines per second. The maximum allowed rotation rate can be estimated by calculating the burst speed of a rotating disk.

In a rotating solid disk made of a homogeneous isotropic material, the maximum stress occurs at the center of the disk. At the center the tangential and radial stresses are equal, and their value is given by[31]

$$\sigma_r = \sigma_\theta = \frac{3 + \eta}{8} \rho \omega^2 R^2, \tag{8}$$

where σ is the stress, ρ is the density, ω is the angular velocity, R is the radius of the disk, and η is Poisson's ratio, which for most materials[32] is approximately 0.25. Therefore the maximum achievable rotation rate is

$$M_{max} = \frac{1.57}{2\pi R} \sqrt{\frac{T}{\rho}} \quad \text{rev/sec}, \tag{9}$$

where T is the ultimate tensile strength of the material.

For a tilting mirror, the scan angle, Ψ, is twice the mirror tilt angle, and therefore for a polygon $\Psi = 4\pi/v$. The minimum achievable diffraction angle is determined by the effective aperture size. It is easy to show that with uniform slit illumination the number of resolvable spots per line, N, scanned by a rotating mirror polygon, is

$$N \cong f \frac{8\pi R}{v\lambda} \sin\left(\frac{\pi}{v}\right), \tag{10}$$

where f is the required fractional blanking time, λ is the light wavelength, and R is the radius of the circumscribed circle. A resolution higher than predicted by Eq. [10] can be obtained at the expense of

reduced light utilization efficiency. In very high resolution scanning systems the incident beam completely floods at least two facets of the rotating mirror polygon. The size and the location of the image plane is selected so that exactly at the time when the scanning beam from one facet comes to the end of a scan line, the scanning beam from the next facet starts the next successive scan line.[1] In this case the resolution can be calculated from Eq. [10] by setting $f = 1$ and for a 1-cm radius four-sided polygon $N \simeq 10^5$ spots per scan line. The maximum number of spots per second, B, that a mirror polygon can scan is,

$$B = v M_{max} N = f \frac{6.28}{\lambda} \sqrt{\frac{T}{\rho}} \sin \left(\frac{\pi}{v} \right) . \qquad [11]$$

Assume that a 1-cm radius four-sided polygon is made out of bronze ($T \simeq 10^5$ psi $\simeq 10^{10}$ dynes/cm^2, $\rho \simeq 8.8$ grams/cm^3), that 10% fractional blanking time is acceptable ($f = 0.1$), and that 5,000-Å light is used. Then, from the above equations, we obtain: $M_{max} \simeq 10^4$ rev/sec, $N = 10^4$ spots/line, and $B = 4 \times 10^8$ spots/sec. Clearly, the rotating-mirror polygon is well suited for high-resolution scanning applications. For the much lower resolution and deflection rate required for a vertical television deflector, other, more convenient alternatives exist.

b. Rotating Refractive Prisms

When a light ray is transmitted through a transparent plane-parallel plate at incidence angles other than normal, the exit ray is displaced and parallel to the entrance ray. Therefore a rotating even-sided glass polygon, illuminated with a convergent (or divergent) ray bundle, offers a convenient means of light scanning. The outstanding feature of the rotating prism deflector is that it allows operation with in-line optics. A convenient feature, common with rotating-mirror polygons, is that it can be simply driven by a synchronous motor. As will be shown below, the refractive prism deflector can be arranged to produce an extremely short flyback time (approximately equal to an element time) without a corresponding reduction of the effective aperture size. The effective aperture, however, is limited by the severe geometric aberrations inherent to rotating refractive prism deflectors. They are well suited only for applications requiring approximately 10^3 resolvable spots maximum resolution.

The basic arrangement is shown in Fig. 9. The plane-parallel plate of thickness d and index of refraction n is tilted with respect to the

central ray of the incident convergent bundle by angle β. The ray bundle has a half convergence angle θ. The displacement, y, of the central ray can be easily calculated from Snell's law;

$$y = \sin \beta \left(1 - \frac{\cos \beta}{\sqrt{n^2 - \sin^2 \beta}} \right), \qquad [12a]$$

and for small tilt angles $(\beta \ll \pi/2)$,

$$y \simeq \beta \left(1 - \frac{1}{n} \right) + 0(\beta^3). \qquad [12b]$$
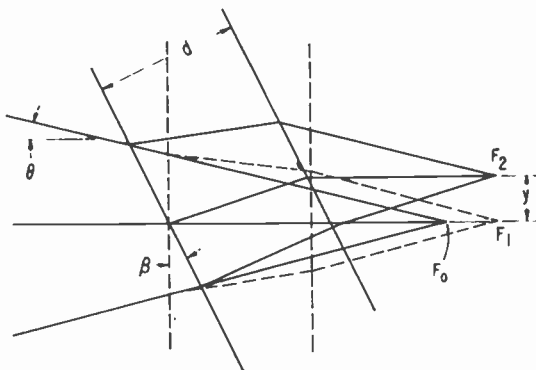
Fig. 9—Illustration of principle of operation of a refractive prism deflector. F_0 is the point where the light would focus in the absence of the slab.

Because the displacement of a ray depends on its incidence angle, the presence of the slab destroys the geometric focus. An estimate of the aberration introduced can be obtained by calculating the longitudinal aberration at $\beta = 0$. In this case a ray incident at angle θ intersects the central ray at an axial distance z, measured from F_0 in Fig. 9:

$$z = d \left(1 - \frac{\cos \theta}{\sqrt{n^2 - \sin^2 \theta}} \right), \qquad [13a]$$

and for $\theta \ll \pi/2$,

$$z \simeq d \left(1 - \frac{1}{n} \right) + \theta^2 \frac{d}{n} \left(1 - \frac{1}{2n^2} \right). \qquad [13b]$$

As the slab is rotated, even the central ray bundle (θ aproaching zero) does not focus on a plane. The axial displacement for the $\theta \to 0$ bundle is given by

$$\epsilon = d \left[\cos \beta - \frac{\cos (2\beta)}{(n^2 - \sin^2\beta)^{1/2}} - \frac{1}{4} \frac{\sin^2 (2\beta)}{(n^2 - \sin^2\beta)^{3/2}} \right], \qquad [14a]$$

and for $\beta \ll \pi/2$

$$\epsilon \simeq d \left(1 - \frac{1}{n} \right) + \beta^2 \frac{d}{n} \left(2 - \frac{n}{2} - \frac{3}{2n^2} \right). \qquad [14b]$$

The two aberration formulas, Eqs. [13a] and [14a], can be used to estimate the resolution capability of the rotating-prism deflector. The minimum convergence angle allowed by diffraction considerations for 500-spot resolution, with $n = 1.5$, $v = 8$ and $d = 2$ cm, is $2\theta \simeq 5 \times 10^{-2}$ rad. The geometric spot size is given by $2\theta\Delta z$. Therefore, with the aid of Eq. [13b], we conclude that the longitudinal aberration will not be important. The curvature of the focal plane, Eq. [14a], however, does limit the resolution. By selecting the nominal focal plane such that the best focus occurs at $\beta = \beta_{max}/\sqrt{2}$ and calculating the geometric spot size from Eq. [14b] with $2\theta = 5 \times 10^{-2}$ rad, we find that at $\beta = 0$ and $\beta = \beta_{max}$, the equivalent resolution drops to approximately 200 spots.

The limitation on the resolution resulting from the curvature of the focal plane is, however, significantly reduced if the scanner image is projected with large magnification onto a viewing screen. Using the thin-lens imaging formula, one can easily show that

$$\delta = - \frac{m}{\dfrac{1}{m} + \dfrac{\epsilon}{F}} \epsilon, \qquad [15]$$

where m is the linear magnification, F is the focal length of the projection lens, and δ is the deviation from the nominal image plane as a result of the deviation ϵ from the nominal object plane. If ϵ is small in

comparison with the focal length of the projection lens and $m \gg 1$, then the geometric spot-size-limited resolution in the image plane, N_p, is given by

$$N_p = N \left(1 + m \frac{\epsilon}{F} \right), \qquad [16]$$

where N is the geometric spot-size-limited resolution in the nominal object plane, as determined by the curvature of the object plane.

Eq. [16] appears to suggest that as the magnification is increased, the resolution will continuously increase. Clearly this is not possible. This apparent anomaly is resolved by noting that Eq. [16] takes into account only the geometric spot size. For sufficiently large magnifications the scanner aberrations will be masked by the diffraction spread and the ultimate resolution is then given by Eq. [17] discussed below.

The typical experimental values are $m = 10^2$, $F = 5$ cm, and, for the above example, $\epsilon = 0.12$ cm. Then, with $N = 200$, we find $N_p \simeq 650$ spots. Therefore, we conclude that in a typical projection arrangement the prism-deflector-induced focal-plane curvature limitation on the resolution is not important, and diffraction-limited operation of 500-line deflectors is possible. This conclusion is in agreement with our experimental observations.

Additional details of the aberrations, obtained by numerical evaluation of the appropriate ray-tracing formulas, are given in Figs. 10 and 11. On these figures, U, L and C denote the principal rays, incident at angles $\theta - \beta$, $\theta + \beta$, and β, respectively. (U,C), (U,L) and (L,C) denote the intersection of the bracketed ray pairs. The importance of operating with narrow cone angles is especially apparent from Fig. 11.

In addition to the aberrations discussed above, the rotating-prism deflector is also astigmatic.[33] The hybrid laser scanner, however, uses independent cylindrical lens chains for the x and y directions, and therefore the astigmatism can be compensated.

Thus far we have not discussed any restrictions arising as a result of blanking considerations. When a rotating refractive prism is used with a convergent ray, the size of the ray bundle incident on the entrance facet must not exceed the product of the fractional blanking time and the facet dimension in the scan plane. In this case, however, the diffraction-limited resolution is significantly less than 500 spots. A much more favorable arrangement is indicated on Fig. 12. Here, the light is brought to a focus before entering the prism and deflection is obtained by displacement of the virtual image. Fly-back occurs during the time the focus clears the prism corner; i.e., the time requirement is
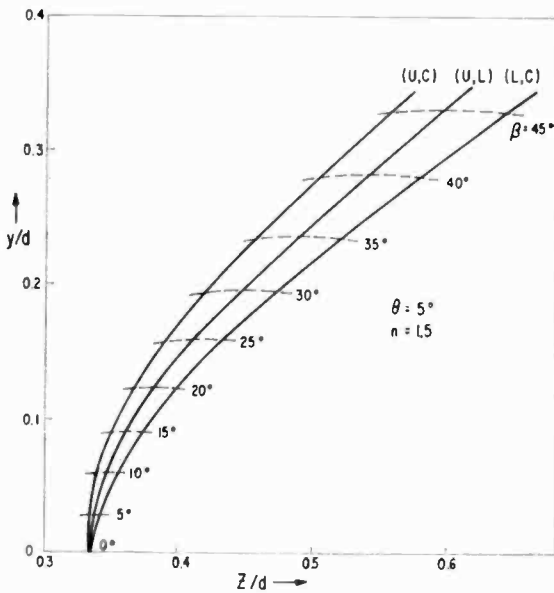
Fig. 10—Performance of a rotating refractive prism deflector. Intersections of the principal rays of a cone with 5° half angle.
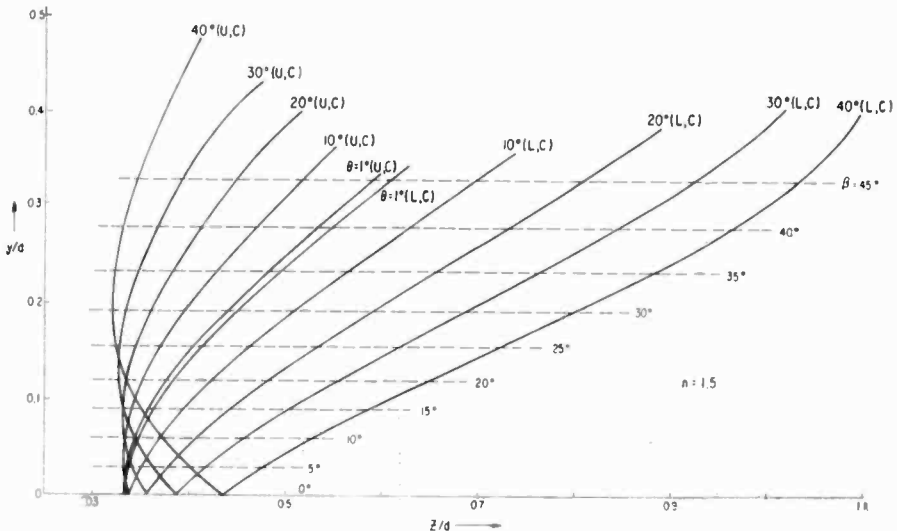

Fig. 11—Performance of a rotating refractive prism deflector. Intersections of the extreme rays with the central ray. This figure clearly illustrates the importance of narrow cone operation.

approximately one element time. (If the prism is used as the vertical deflector in a raster scanner, then the resulting flyback time is approximately one horizontal line time.) The rays drawn with solid lines on Fig. 12 correspond to the instant in time when the facet pair formed by A_1 and A_2 is operative; the dotted lines correspond to when facets B_1 and B_2 are operative. The cone angle restriction is then that at no
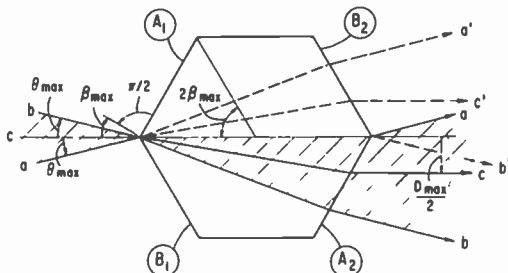

Fig. 12—The illumination of a rotating refractive prism deflector that allows the minimum fractional blanking time and the highest possible resolution.

instant in time should any portion of the bundle exit through any other facet but the one opposite to the entrance facet. With this restriction one easily finds in the paraxial ray approximation that $\theta_{max} = n\pi/v$, and, with uniform illuminating intensity distribution, the number of diffraction-limited resolvable spots is

$$N = \frac{d}{\lambda} \frac{4\pi^2}{v^2} (n-1). \qquad [17]$$

A comparison of Eqs. [17] and [10] indicates that, since $d \simeq 2R$, and for most applications, $n - 1 > f$, taking only diffraction limitations into account, the resolution of the rotating refractive prism is higher than that of the rotating-mirror polygon. Both of these devices suffer from curvature of focal plane; in some applications (e.g., recording), this curvature can be fully compensated for. The longitudinal aberration of the refractive-prism deflector, however, necessitates a convergence angle $\theta \ll \theta_{max}$. By equating the diffraction-limited spot size, $w = \lambda/2\theta$, with the geometrical spot size $2\theta\Delta z$, where Δz is obtained from Eq. [13b] for the longitudinal aberration, one can determine the resolution where the diffraction-limited and the aberration-limited resolutions are equal. For $d = 2$ cm, $v = 8$, and $n = 1.5$, we find $2\theta = 1.3 \times 10^{-1}$ rad and the corresponding resolution is 1.3×10^8 spots,

c. Galvanometer Mirrors

Recently available galvanometer-driven mirrors are excellent scanning devices for intermediate resolution (a few thousand spots) and slow scan rate (a few hundred scans per second, with approximately half a millisecond retrace) range. These devices consist of a small mirror mounted on the shaft of a moving-iron galvanometer. Their drive signal requirements consist of a linear current ramp during the active portion of the scan and a precisely timed two-step pulse during retrace.[10] By precisely adjusting the retrace pulse, a flyback time that is approximately equal to one half the period of the natural mechanical oscillation of the mirror-loaded galvanometer can be obtained.

The diffraction-limited resolution is determined by the maximum achievable tilt angles, β_{max}, and the mirror dimension in the scan plane, b. Then

$$N = \frac{2 \beta_{max} b}{\lambda}. \qquad [18]$$

Commercially available galvanometers* are capable of $\beta_{max} = 0.14$ rad with 0.75-cm mirror aperture, resulting in 4,200-spot resolution at $\lambda = 5000$ Å.

The resolution is proportional to the mirror size, but the inertia also increases with mirror size. For the device cited above, the mirror dimensions are 0.1 cm thickness and 0.75×1.1 cm^2 area; the mirror inertia is approximately equal to the armature inertia, and the complete mirror-loaded galvanometer natural resonant frequency is approximtely 10^3 Hz. With proper drive-signal conditioning, sawtooth rates that are 40% of the natural resonant frequency can be obtained. Therefore, this device is capable of 400 scans per second with 500 microseconds retrace time; clearly the 20% blanking time at the maximum sawtooth rate is excessive for most applications. However, at the 60 scans per second rate required for television vertical deflection, the device operates well within the allowed 5% (750-microsecond) blanking time.

4. The Frequency Response of Deflected Beams

4.1 General Formulation

The most convenient way to describe quantitatively the performance of beam-deflection systems is to calculate the spatial intensity varia-

---

* General Scanning, Inc., 80 Coolidge Mill Road, Watertown, Mass. 02172, Model GS-108.

tions that result when the beam is modulated by a periodic signal. We shall consider both intensity and position (wobble) modulation. Intensity modulation is the common technique, well known from television practice; the beam intensity is modulated and its position is advanced, usually in a linear fashion. Position modulation refers to the technque where a "wobble" is superimposed on a linear scan to produce a spatial carrier. By controlling the "wobble" amplitude, the amplitude of the spatial carrier can be modulated. Appropriate light-valve structures must then be used for display purposes.

We are primarily interested in the performance of acousto-optic Bragg deflectors. Most of the calculations presented here, however, are more general; they are applicable to a wide range of beam-deflection systems, including electron beams. Following common practice, the calculations are restricted to the one-dimensional case (i.e., we assume that the beam is scanned in the x,y plane in the x direction and that there is no y variation).

Denote the instantaneous beam position as a function of time t by $x'(t)$ and the beam-spread function, describing the intensity distribution of the stationary beam centered at $x = 0$, by $S(x)$. The instantaneous intensity distribution is then $S(x - x'(t))$. The intensity modulation is described by $M(t)$. The instantaneous exposure is then

$$I(x,t) = M(t) \, S \, (x - x'(t)). \tag{19}$$

The total exposure is

$$E(x) = \int_{-\infty}^{\infty} I(x,t) \, dt. \tag{20}$$

In direct-view display systems, integration is accomplished by the human eye; in light-valve and recording structures, it is accomplished by their inherent storage properties.

Two spread functions are especially of practical interest: (1) When the spread of the beam in the scan plane is much smaller than the smallest spatial frequency of interest, the spread function can be approximated by that of an infinitessimally fine beam:

$$S(x) = \delta(x). \tag{21}$$

(2) When the beam size is diffraction limited by a slit of width D,

and the beam-forming focusing optics has focal length f, then

$$S(x) = \left[\frac{\sin Ax}{Ax} \right]^2 , \qquad [22]$$

where

$$A = \frac{\pi D}{\lambda f} , \qquad [23]$$

and λ is the wavelength.

4.2 Intensity-Modulated, Linearly Scanned Beams

a. Uniformly Illuminated Aperture

We assume that the beam intensity is modulated at angular frequency and that the beam is scanned with linear velocity v. Then

$$M(t) = \exp \{j\omega t\}, \qquad [24]$$

$$x'(t) = vt, \qquad [25]$$

and from Eq. [20],

$$E(x) = \int_{-\infty}^{\infty} dt \exp \{j\omega t\} \, S(x - vt). \qquad [26]$$

Set $x - vt = \tau$. Then

$$E(x) = \frac{1}{v} \int_{-\infty}^{\infty} d\tau \exp \left\{ -j \frac{\omega \tau}{v} \right\} S(\tau) \exp \left\{ j \frac{\omega x}{v} \right\}$$

$$\qquad [27]$$

$$= E_\omega \exp \left\{ j \frac{\omega x}{v} \right\}$$

The normalized frequency response, $R(\omega)$, is defined as

$$R(\omega) = \frac{E_\omega}{E_o} = \frac{\int\limits_{-\infty}^{\infty} d\tau \exp\left\{-j\frac{\omega\tau}{v}\right\} S(\tau)}{\int\limits_{-\infty}^{\infty} d\tau\, S(\tau)}. \tag{28}$$

In the most common Bragg deflector arrangement, the acousto-optic cell with aperture D is uniformly illuminated by a collimated beam. There, by substituting Eq. [22] into [28], we obtain

$$R(\omega) = 1 - \frac{\omega}{\omega_{max}} \qquad \omega \leqslant \omega_{max} \tag{29}$$

$$= 0 \qquad \omega \geqslant \omega_{max}$$

where $\omega_{max} = 2Av = 2\pi Dv/(\lambda f)$. Assume that the beam is scanned linearly over distance L in time $T = L/v$. According to the usual definition, the number of resolvable (Rayleigh criterion) spots along the line of length L is $N = LA/\pi = (LD)/(\lambda f)$. Therefore,

$$\omega_{max} = 2\pi \frac{N}{T}. \tag{30}$$

b. Geometric Interpretation and Simple Aperture Examples

In the previous section the direct analytical solution to the frequency-response problem was outlined. Here we will show that Eq. [28] has an important geometrical interpretation that greatly facilitates its evaluation. This interpretation is analogous to the one employed in the calculations of the optical transfer function of incoherent imaging systems.[34]

Consider the deflector arrangement shown in Fig. 13. The deflector element indicated is an acousto-optic cell, located adjacent to a thin positive lens of focal length f. The deflector is illuminated by a plane wave, and the scan line is formed in the back focal plane of the lens.

Denote the field distribution incident on the lens by $P(x_o)$. (We again restrict ourselves to the one-dimensional case.) $P(x_o)$ is determined by the incident plane wave field distribution and by the shading and aperturing that may be introduced by stops and losses in the deflector-lens combination. With the beam stationary and centered at $x = 0$, the field distribution in the focal plane is[35]

$$U_f(x) = \frac{B}{j\lambda f} \exp \left\{ j \frac{\pi x^2}{\lambda f} \right\} \int_{-\infty}^{\infty} dx_o \, P(x_o) \exp \left\{ -j \frac{2\pi}{\lambda f} x_o x \right\}, \qquad [31]$$

where B is proportional to the square root of the incident power in the beam. The spread function is given by the intensity distribution:

$$S(x) = U_f(x) \, U_f^*(x). \qquad [32]$$
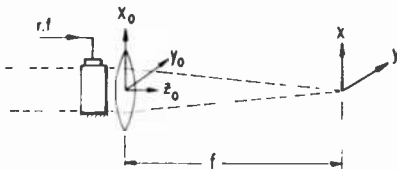
Fig. 13—The basic acousto-optic deflector arrangement.

Therefore the instantaneous intensity distribution of the scanning beam is

$$S(x - vt) = \frac{B^2}{\lambda^2 f^2} \int_{-\infty}^{\infty} \int_{-\infty}^{\infty} dx_o dx_o' P(x_o) P^*(x_o') \exp \left\{ -j \frac{\pi 2}{\lambda f} [x_o(x - vt) \right.$$

$$\left. - x_o'(x - vt)] \right\} \qquad [33]$$

From Eq. [27],

$$E_\omega = \int_{-\infty}^{\infty} \frac{d\tau}{v} S(\tau) \exp \left\{ -j \frac{\omega \tau}{v} \right\}$$

$$= \frac{B^2}{v\lambda^2 f^2} \int\limits_{-\infty}^{\infty} \int\limits_{-\infty}^{\infty} \int\limits_{-\infty}^{\infty} d\tau dx_o dx_o' P(x_o) P^*(x_o') \exp\left\{ -j\frac{2\pi}{\lambda f}(x_o \right.$$

[34]

$$\left. -x_o')\tau \right\} \exp\left\{ -j\frac{\omega\tau}{v} \right\}$$

Note that

$$\int\limits_{-\infty}^{\infty} d\tau \exp\left\{ -j\left[\frac{2\pi}{\lambda f}(x_o - x_o') - \frac{\omega}{v} \right]\tau \right\}$$

[35]

$$= \lambda f \delta\left[x_o - \frac{\lambda f\omega}{2\pi v} - x_o' \right].$$

Therefore

$$E_\omega = \frac{B^2}{v\lambda^2 f^2} \int\limits_{-\infty}^{\infty} dx_o P(x_o) P^*\left(x_o - \frac{\lambda f\omega}{2\pi v} \right).$$

[36]

Then we can rewrite the frequency response, Eq. [28], as

$$R(\omega) = \frac{\displaystyle\int\limits_{-\infty}^{\infty} dx_o P(x_o) P^*\left(x_o - \frac{\lambda f\omega}{2\pi v} \right)}{\displaystyle\int\limits_{-\infty}^{\infty} dx_o |P(x_o)|^2}.$$

[37]

Eq. [37] indicates that the frequency response can be calculated

simply as a normalized overlap integral. This geometric interpretation is especially useful and easy to use when the incident field distribution $P(x_o)$ is real and positive (i.e., no phase-shifting stops are employed). Three simple examples are shown in Fig. 14. It is easily seen from
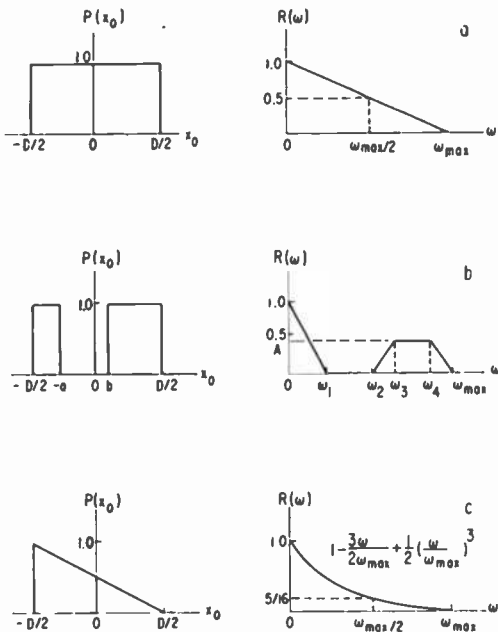

Fig. 14—Three simple examples easily calculated with the aid of the geometric interpretation. $P(x_o)$ is the amplitude distribution across the aperture and $R(\omega)$ is the freqcency response of the scanner.

Eq. [37] that if the deflector–lens combination has a beam-limiting aperture of width D, then, independently of any shading and stops internal to the aperture, the overlap integral is zero for displacements greater than D. Therefore in all these cases

$$\omega_{\max} = \frac{2\pi v}{\lambda f} D. \qquad [38]$$

The example in Fig. 14a corresponds to the uniformly illuminated slit treated in the previous section. Fig. 14b is a uniformly illuminated slit with an arbitrarily located stop within it. The various amplitude and frequency values indicated on the figure are

$$A = \frac{\dfrac{D}{2} - a}{D - a - b},$$

$$\omega_1 = \omega_{max} \frac{a}{D}, \qquad\qquad \omega_2 = \omega_{max} \frac{a + b}{D}, \qquad\qquad [39]$$

$$\omega_3 = \omega_{max} \left(\frac{1}{2} + \frac{b}{D} \right), \qquad \omega_4 = \omega_{max} \left(\frac{1}{2} + \frac{a}{D} \right).$$

Note from Fig. 14b that by employing a suitable stop, the high-frequency response can be significantly improved, but only at the expense of the response at intermediate frequencies. Also, it is easy to show that the maximum possible high-frequency peaking results in a response that is one half of the zero frequency response. Fig. 14c shows a uniformly shaded aperture; as indicated, uniform shading always reduces the response at all frequencies.

Another example, of practical interest occurs when the incident field amplitude distribution is Gaussian,

$$P(x_o) = \exp \left\{ - \frac{x_o^2}{w_o^2} \right\}, \qquad\qquad [40]$$

corresponding to a fundamental-mode laser beam.

Clearly if the Gaussian parameter w_o is much larger than the limiting aperture (e.g., size of the Bragg deflector), the frequency distribution is well approximated by the uniformly illuminated aperture case treated above. In the opposite case, i.e., when $w_o \ll D$, then from Eq. [37] one easily determines that the frequency roll-off is also a Gaussian:

$$R(\omega) = \exp \left\{ - \frac{\omega^2}{\omega_o^2} \right\} \qquad\qquad [41]$$

where

$$\omega_o = \frac{\sqrt{8}\pi v w_o}{\lambda f}.$$

Results of numerical solutions for the intermediate range, $w_o \approx D$, are

shown in Fig. 15. It can be easily seen that since the illumination function is peaked at the center, the spread function will broaden (a trend opposite to that indicated on Fig. 14b). Therefore the high-frequency response with Gaussian illumination will always be poorer than with uniform illumination. The limiting resolution, ω_{max}, is again given by Eq. [38].
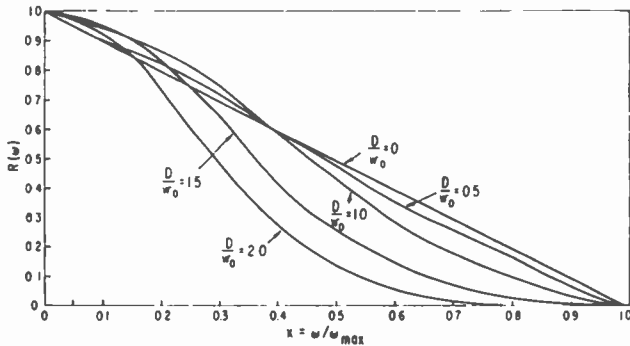

Fig. 15—The frequency response of deflector illuminated by a Gaussian beam. D is the full width of the aperture and $w_{\bullet}$ is the Gaussian parameter of the amplitude distribution across the aperture.

c. The Effect of Acoustic Losses on the Resolution of Bragg Deflectors

The characteristic exponential sound-wave absorption lengths of the best acousto-optic materials at frequencies that are well within the capability of current transducer technology are comparable to the useful optical apertures (approximately 1 cm). Therefore it is of great practical interest to estimate the effect of acoustic losses on the resolution of acousto-optic deflectors.

We restrict our analysis to weak acousto-optic interactions in the Bragg regime. There,

$$I_1 = I_o \left(\frac{\Delta\phi}{2} \right)^2 , \qquad [42]$$

where I_o is the intensity of the light beam incident on the deflector, I_1 is the deflected beam intensity, $\Delta\phi$ is the sound-wave-induced phase retardation and is proportional to the square root of the acoustic power. The acoustic-wave power attentuation coefficient is 2α and the aperture of width D is centered at $x_o = 0$. The effect of the decreasing sound power across the aperture is an exponential shading. The

spread function can be calculated in a straightforward manner; one obtains

$$S(x) = \exp\left\{-\alpha D\right\} \left| \frac{\sin\left(Ax - \dfrac{j\alpha D}{2}\right)}{Ax - \dfrac{j\alpha D}{2}} \right|^2 \qquad [43]$$
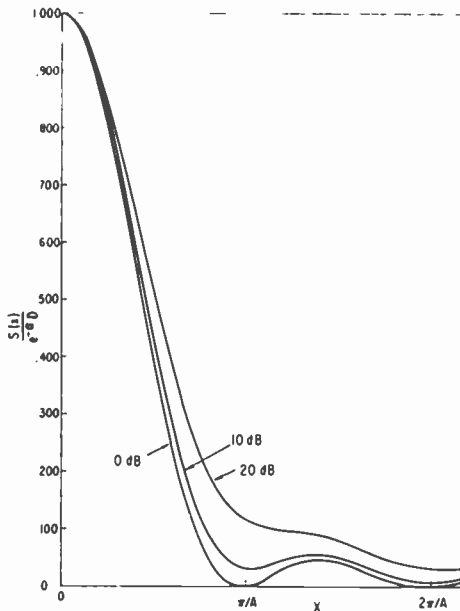

Fig. 16—The spread function with 0, 10, and 20 dB acoustic attenuation across the aperture.

Fig. 16 is a normalized plot of $S(x)$ for 0, 10, and 20 dB acoustic power loss across the aperture. The effect of the losses on the broadening of the spread function is very small; therefore the effect on the frequency response is rather small, too. The frequency response $R(\omega)$ is plotted in Fig. 17 for various acoustic losses. Clearly, the main effect is a slight lowering of the high-frequency response, but for all practical purposes this decrease in resolution is negligible up to ~10 dB. By integrating Eq. [42] across the aperture one can easily calculate the effect of sound attenuation on the deflector efficiency. Let η denote the

normalized efficiency (i.e., the optical efficiency with acoustic losses, divided by the efficiency without losses where, in the lossy case, the induced phase retardation, $\Delta\phi$, at the transducer is equal to that over the entire aperture in the lossless case);
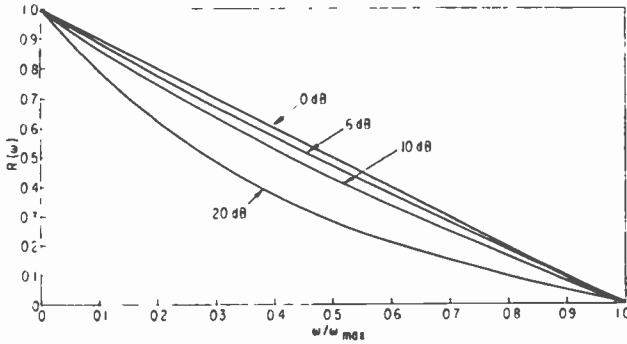

Fig. 17—The frequency response of a scanner with uniformly illuminated aperture and 0, 6, 10, and 20 dB acoustic attenuation across the aperture.

$$\eta = \frac{1}{D}\int_{-D/2}^{D/2} \exp\left\{-2\alpha\left(x_o + \frac{D}{2}\right)\right\} dx_o$$

[44]

$$= \frac{1}{2\alpha D}(1 - \exp(-2\alpha D)).$$

Fig. 18 is a plot of Eq. [44]. Note that over 6 dB acoustic loss across the aperture is permissible before the deflector optical efficiency drops by a factor of two.

From the above we can conclude that for most practical cases of interest the effect of a few dB acoustic loss in the deflector is negligible as far as either the resolution or the optical efficiency is concerned. A far more serious problem associated with acoustic losses is the heating of the deflector that can result in thermal distortions (thermal lens effects).

Because of the thermal distortions, the acoustic losses must be kept below some experimentally determined acceptable maximum (typically in the few-dB range). The resolution of a Bragg deflector is given by the product of the acoustic transit time and the rf bandwidth; the

maximum allowed bandwidth is limited by image overlap to an octive

$$N = \frac{D}{v_a} \frac{f_{max}}{2}, \qquad\qquad [45]$$
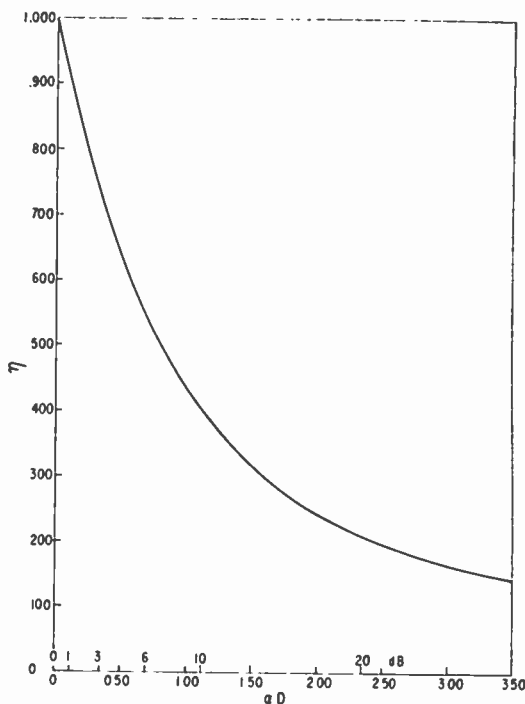
Fig. 18—The normalized efficiency of an acousto-optic deflector with acoustic attenuation across the aperture. The exponential acoustic power attenuation coefficient is 2α, and the aperture width is D.

where v_a is the acoustic velocity and f_{max} is the highest operating rf frequency. Over the typical operating frequency range, the acoustic losses can be well described by a simple power law;

$$G(\text{db}) = D\lambda f^p_{max}. \qquad\qquad [46]$$

where G is the acoustic power loss in dB across the aperture of length D at the maximum operating frequency, and γ and p are constants of the acousto-optic material. For device optimization, one wishes to determine optimum f_{max}, subject to the constraints that the deflector retrace time requirement sets the maximum allowed aperture size and

the thermal lensing effects allow a maximum acoustic loss G_{max}. Denote the retrace time by T_o. Then

$$D_{max} = v_a T_o,$$ [47]

and from Eq. [46]:

$$f_{max} = \left[\frac{G_{max}}{D_{max} \gamma} \right]^{1/p} = \left[\frac{G_{max}}{\gamma v_a T_o} \right]^{1/p} .$$ [48]

By substituting Eqs. [47] and [48] into Eq. [45] we obtain

$$N_{max} = \frac{T_o}{2} \left[\frac{G_{max}}{\gamma v_a T_o} \right]^{1/p} .$$ [49]

To indicate the significance of Eq. [49], let us evaluate the optimum conditions for a Bragg deflector, constructed out of lead molybdate,[22,23] by assuming that the deflector is going to operate at horizontal television deflection rate ($T_o = 10 \, \mu\text{sec}$) and that the acoustic loss should not exceed 1 dB. From the published values we find that $\gamma = 10^{-17}$ (dB-sec^2)/cm, $v_a = 3.75 \times 10^5$ cm/sec, and $p = 2$. Then from Eqs. [48] through [49], we find $N_{max} = 800$ spots, $f_{max} = 163$ MHz, and $D_{max} = 3.75$ cm.

d. Effect of Cleavage Planes on Bragg-Deflector Performance

The best currently known technique for attaching transducers to acousto-optic materials requires cold bonding. This cold bonding requires high pressures that frequently result in cleavage planes perpendicular to the sound-propagation direction. By comparing faultless and cleaved deflectors employed in a complete, intensity-modulated laser scanner, we have observed that (1) the limting resolution ω_{max} is very little affected by the presence of cleavage, and (2) at best overall focus, the scanned pattern is slightly fuzzy with some frequency components, $\omega < \omega_{max}$, appearing completely out of focus. A possible explanation for this behavior can be obtained by assuming that the result of the cleavages is a complex field distribution in the aperture.

For simplicity's sake, assume that a clean cleavage is present in
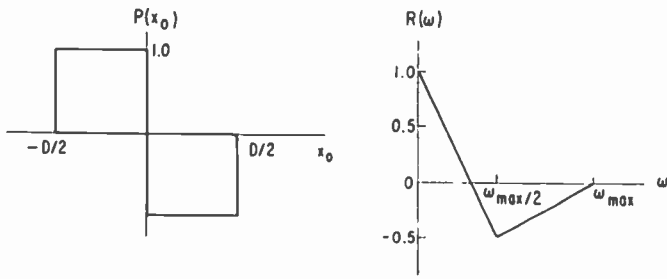
Fig. 19—The frequency response of a scanner with phase shift across the aperture.

the deflector at $x_o = 0$ and that, as it is commonly observed, the cleavage plane is perpendicular to x_o (see Fig. 13). In this case, the upper $(x_o > 0)$ half of the deflector is slightly displaced with respect to the lower half. This displacement results in an amplitude illumination function $P(x_o)$ such that there is a constant phase shift between the regions $x_o > 0$ and $x_o < 0$. Fig. 20 shows an example in which this shift was assumed to be π (one half optical wavelength). Then $P(x_o) = +1$ for $-D/2 < x_o < 0$ and $P(x_o) = -1$ for $0 < x_o < D/2$. Using the geometric interpretation of Eq. [37], $R(\omega)$ can be readily obtained and is also shown on Fig. 19. Note that when $R(\omega) = 0$ for $\omega < \omega_{max}$, the corresponding frequency burst in a test pattern appears washed out, as if it were out of focus. When $R(\omega)$ is negative, the display
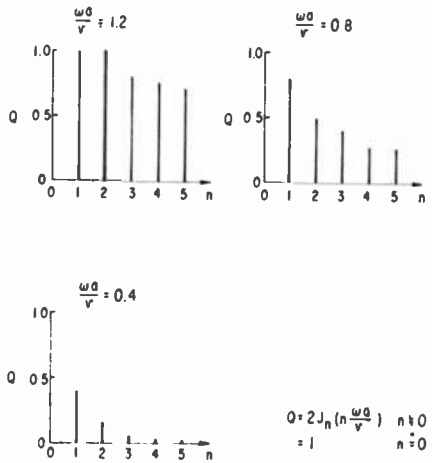

Fig. 20—The relative amplitudes of the harmonic terms in the response of a very high resolution deflection modulated beam. (See the discussion following Eq. [53] in the text.)

system produces a contrast reversal, corresponding to 180° phase shift in a burst pattern. In general, $R(\omega)$ can be complex. Thus, depending on the phase variation of $P(x_o)$, any phase shift in a burst pattern is possible. Frequency-dependent phase shifts, will, however, always lead to a degraded fuzzy display that is somewhat reminiscent of a slightly misfocused image.

4.3 Deflection-Modulated Beam Scanning

All the examples treated in the previous sections involved the intensity modulation of linearly advancing beams. A time-variant signal can also be converted into spatial intensity variations by modulating the instantaneous beam position, $x'(t)$, of a constant-intensity beam. Clearly, this modulation technique is not suiltable for direct-view display systems, but it has been successfully used in electron-beam-controlled light valves.[36, 37*] It may find application in laser-beam-addressed recording and light-valve arrangements. This technique has one main advantage over the simple intensity modulation; because the beam intensity is constant, the average exposure over large areas is also constant. This feature is very useful when addressing deformable-medium-type light valves (e.g., thermoplastics, oil films, etc).

First we treat the simple problem when a very fine beam has a constant-amplitude sinusoidal wobble modulation at angular frequency ω superimposed on its linear scan. Then

$$x'(t) = vt + a \cos \omega t, \qquad [50]$$

and since $M(t) = 1$, from Eq. [20] we have

$$E(x) = \int_{-\infty}^{\infty} dt\, \delta\,(x - vt - a \cos \omega t). \qquad [51]$$

By making use of the following mathematical identities, Eq. [51] can be integrated in a straightforward manner:[†]

---

* Even though wobble-modulated light valves have been built, to the authors' knowledge no detailed analysis of this modulation technique has been published.

† The authors express their appreciation to R. W. Cohen of RCA Laboratories for the analytical evaluation of the wobble modulation exposure integrals.

where A is given by Eq. [23]. By making use of Eqs. [52] and of the identity

$$\frac{\sin^2 A\,(x-\xi)}{(x-\xi)^2} = \frac{1}{2\pi} \int_{-2A}^{+2A} dk\pi \left(A - \frac{|k|}{2} \right) \exp \left\{ -jk\,(x-\xi) \right\}. \quad [59]$$

Eq. [58] can be integrated and the result is

$$E(x) = \frac{\pi}{vA} \left[1 + 2 \sum_{n=1}^{[n_{\max}]} \left(1 - \frac{n\omega}{2vA} \right) J_n \left(\frac{n\omega a}{v} \right) \cdot \right.$$

$$\left. \cos \left[n \left(\frac{\omega x}{v} - \frac{\pi}{2} \right) \right] \right], \quad [60]$$

where

$$n_{\max} = \frac{2Av}{\omega} = \frac{2\pi Dv}{\lambda f \omega} = \frac{\omega_{\max}}{\omega}, \quad [61]$$

and $[n_{\max}]$ denotes the maximum integer that does not exceed $n_{\max}$.

Note that the first bracketed term in the summation corresponds to the linear roll-off associated with the finite beam size, and is shown in Fig. 14a. The summation is carried out only for those harmonics that are below the cutoff frequency $\omega_{\max}$. If $\omega_{\max}/2 \leqslant \omega < \omega_{\max}$, only the fundamental term is present. At $\omega = \omega_{\max}/2$

$$E(x) = \frac{\pi}{vA} \left[1 + J_1 \left(\frac{\omega_{\max} a}{2v} \right) \cos \left(\frac{\omega_{\max} x}{2v} \right) \right], \quad [62]$$

and since the maximum value of J_1 is 0.58 at $(\omega_{\max} a)/(2v) \cong 2$, over 50% of the beam intensity can be utilized in writing the carrier. (The spatial modulation is on top of a 42% dc component.) The required peak wobble excursion is

$$a = \frac{4v}{\omega_{\max}} = \frac{2vT}{\pi N} = \frac{2L}{\pi N}, \quad [63]$$

(See Eq. [30] and the discussion preceding it). Recall that the full scan-line length L is scanned with N Rayleigh criterion spots. Therefore, the required resolution, N_W, of the wobble producing deflector is

$$N_W = N \frac{a}{L} = \frac{2}{\pi}. \qquad [64]$$

Eq. [64] indicates that the required wobble modulator resolution is less than one Rayleigh spot. In a high-quality television-type system $\omega = \omega_{max}/2$ must be higher than the highest video frequency of interest, i.e., it should be set at around 10 MHz. One-spot resolution at these rates is achievable with both electro-optic and acousto-optic deflectors. The main deflector is then required to have a limiting frequency $\omega_{max} \simeq 20$ MHz; with 50 microseconds active line time, this corresponds to $N = 1,000$. We therefore conclude that wobble modulation of a television raster is a realistic goal with currently known laser deflection methods.

Acknowledgments

References:

[1] D. J. Woywood, Private Communication.

[2] M. J. Cowan, D. R. Herriott, A. M. Johnson, and A. Zacharias, "The Primary Pattern Generator, Part I—Optical Design," **Bell Syst. Tech. J.**, Vol. 49, p. 2033, Nov. 1970.

[3] R. F. Kenville, "Noise in Laser Recording," **IEEE Spectrum**, Vol. 8, No. 3, p. 50, March 1971.

[4] S. M. Ravner, Private Communication.

[5] Y. Yamada, M. Yamamoto, and S. Nomura, "Large Screen Laser Color TV Projector," 1970 Sixth International Quantum Electronics Conference, Digest of Technical Papers, p. 242, Kyoto, Japan, Sept. 7-10, 1970.

[6] R. H. McMann and R. Walker, "Laser Beam Recorder for Color TV Film Transfer," Novel Audio-Visual Imaging Systems, Sept. 23-24, 1971, New York, N. Y. Two Day Seminar, organized by the Society of Photographic Scientists and Engineers, Inc.

[7] B. Sherman, J. F. Black, and C. J. Summers, "Scanned Laser Photoluminescence Microscope," 1971 IEEE/OSA Conference on Laser Engineering and Applications, Washington, D.C., June 2-4, 1971 (Digest of Technical Papers, p. 29).

[8] V. J. Fowler and J. Schlafer, "A Survey of Laser Beam Deflection Techniques," **Applied Optics**, Vol. 5, No. 10, p. 1675, Oct. 1966.

[9] C. E. Baker, "Laser Display Technology," **IEEE Spectrum**, Vol. 5, No. 12, p. 39, Dec. 1968.

[10] P. J. Brosens, "Fast Retrace Optical Scanning," **Electro-Optical Systems Design**, Vol. 3, No. 4, p. 21, April 1971.

[11] W. Kulcke, K. Kosanke, E. Max, M. A. Habegger, T. J. Harris, and H. Fleisher, "Digital Light Deflectors," **Applied Optics**, Vol. 5, No. 10, p. 1657, Oct. 1966.

[12] M. L. Dakss and C. G. Powell, "A Fast Digitalized Scan Laser," **IEEE J. Quant. Electr.**, Vol. QE-4, No. 10, p. 648, Oct. 1968.

[13] J. D. Beasley, "Electro-Optic Laser Scanner for TV Projection Display," **Applied Optics**, Vol. 10, No. 8, p. 1934, Aug. 1971.

[14] G. Hepner, "Digital Light Deflector With Prisms and Polarization Switch Based on the Pockels Effect with Transverse Field," **IEEE J. Quant. Electr.**, Vo. QE-8, No. 2, p. 169, Feb. 1972.

[15] J. M. Hammer, "Digital Electro-Optic Grating Deflector and Modulator," **Appl. Phys. Lett.**, Vol. 18, No. 4, p. 147, 15 Feb. 1971.

[16] E. I. Gordon, "A Review of Acousto-Optical Deflection and Modulation Devices," **Proc. IEEE**, Vol. 54, No. 10, p. 1391, Oct. 1966.

[17] R. Adler, "Interaction Between Light and Sound," **IEEE Spectrum**, Vol. 4, No. 3, p. 42, May 1967.

[18] R. W. Dixon, "Acousto-Optic Interactions and Devices," **IEEE Trans. Elec. Dev.**, Vol. ED-17, No. 3, p. 229, March 1970.

[19] W. R. Klein and B. D. Cook, "Unified Approach to Ultrasonic Light Diffraction," **IEEE Trans. Sonics and Ultrasonics**, Vol. SU-14, No. 3, p. 123, July 1967.

[20] G. A. Coquin, J. P. Griffin, and L. K. Anderson, "Wide Band Acousto-Optic Deflectors Using Acoustic Beam Steering," **IEEE Trans. Sonics and Ultrasonics**, Vol. SU-17, No. 1, p. 34, Jan. 1970.

[21] A. Korpel, R. Adler, P. Desmares, and Watson, "A Television Display Using Acoustic Deflection and Modulation of Coherent Light," **Appl. Optics**, Vol. 5, No. 10, p. 1667, Oct. 1966.

[22] D. A. Pinnow, L. G. Van Uitert, A. W. Warner, and W. A. Bonner, "Lead Molybdate: A Melt Grown Crystal with High Figure of Merit for Acousto-Optic Device Applications," **Appl. Phys. Lett.**, Vol. 15, No. 3, p. 83, 1 Aug. 1969.

[23] N. Uchida and Y. Ohmachi, "Elastic and Photoelastic Properties of TeO_2 Single Crystal," **J.A.P.**, Vol. 40, No. 12, p. 4692, Nov. 1969.

[24] N. Uchida and Y. Omachi, "Acousto-Optical Light Deflector Using TeO_2 Single Crystal," **Japan J. Appl. Phys.**, Vol. 9, p. 155 (1970).

[25] Y. Omachini and Uchida, "Acoustic and Acousto-Optical Properties of Pb_2MoO_5 Single Crystal," **J.A.P.**, Vol. 42, No. 2, p. 521, Feb. 1971.

[26] T. Yano, Y. Nabeta, and A. Watanabe, "A New Crystal $Pb_5(GeO_4)(VO_4)_2$ for Acousto-Optic Device Applications," **Appl. Phys. Lett.**, Vol. 18, No. 12, p. 570, 15 June 1971.

[27] W. H. Watson and A. Korpel, "Equalization of Acousto-Optic Deflection Cells in a Laser Color TV System," **Appl. Optics**, Vol. 9, No. 5, May 1970.

[28] J. S. Gerig and H. Montague, "A Simple Optical Filter for Chirp Radar", **Proc. IEEE** (Correspondence), Vol. 52, p. 1753, Dec. 1964.

[29] G. A. Coquin, D. A. Pinnow, and A. W. Warner, "Physical Properties of Lead Molybdate Relevant to Acousto-Optic Device Applications," **J.A.P.**, Vol. 42, No. 6, p. 2162, May 1971.

[30] D. A. Pinnow, "Guide Lines for the Selection of Acousto-Optic Materials," **IEEE J. Quant. Electr.**, Vol. QE-6, No. 4, p. 223, Apr. 1970.

[31] S. Timoshenko, **Theory of Elasticity**, McGraw Hill Book Co., Inc., New York, 1934, p. 68.

[32] Ibid, p. 7.

[33] F. A. Jenkins and M. E. White, **Fundamentals of Optics**, 3rd Edition, McGraw Hill Book Co., New York, 1957, p. 20.

[34] J. W. Goodman, **Introduction to Fourier Optics**, McGraw-Hill Book Co., New York, 1968, p. 146.

[35] Ibid, p. 85.

[36] W. E. Good, "A New Approach to Color Television Display and Color Selection Using a Sealed Light Valve," **Proc. National Electronics Conf.** Volume XXIV, pp. 771-74 (1968).

[37] W. E. Good, T. T. True, R. W. Granville, and H. J. Vanderlaan, "Systems Concepts and Recent Advancements in a Light Valve Color-TV Projector," 1971 SID International Symp., May 4-6, 1971, Philadelphia, Pa. (Digest of Technical Papers, pp. 24-25).

A Television Rate Laser Scanner
II. Recent Developments

I. Gorog, J. D. Knox, P. V. Goedertier, and I. Shidlovsky

RCA Laboratories, Princeton, N. J.

Abstract—An anisotropic Bragg device, fabricated out of paratellurite, has been used as the acousto-optic horizontal deflector in a television-rate laser scanner that previously employed an isotropic lead molybdate acousto-optic device as the horizontal deflector. With approximately 50mW average drive power, at television horizontal scan rate, the TeO_2 deflector produces an average deflection efficiency of 50%. The limiting TV resolution of the scanner is greater than 10 MHz (52 μsec active line time).

Introduction

In the preceding paper[1] we described in detail a television-rate laser scanner that uses an isotropic Bragg device, constructed out of lead-molybdate, as the horizontal deflector. In this paper we report on the performance of a modified version of the same scanner. This version uses an anisotropic Bragg device, constructed out of paratellurite (TeO_2), as the horizontal deflector. Contrary to previous expectations,[2] we found that when an anisotropic TeO_2 deflector is operated at television horizontal scan rate, the peak deflection efficiency need not be restricted to less than 40% in order to restrict the midband dip to less than 20%. With less than a 20% dip, an average deflection efficiency (including 15% blanking time) in excess of 50% is achievable.

A TeO$_2$ acousto-optic deflector was described by Uchida and Oh-machi,[3] who built a single-element, two-dimensional (x-y) deflector utilizing the slow shear waves in TeO$_2$. Their results showed that TeO$_2$ has a very high acousto-optic figure of merit and that the slow shear waves should allow the construction of high-resolution deflectors with small optical apertures. Recently, Warner, et al[2] succeeded in constructing an anisotropic Bragg deflector that makes use of the large optical activity exhibited in TeO$_2$ for light traveling along the c-axis.

The utilization of anisotropic Bragg scattering for light-deflection purposes was suggested by Dixon.[4] He showed that if the velocity of propagation of the scattered light is different from that of the incident light, then for a given deflector resolution the required acoustic dif-fraction spread is less than that required in isotropic media. There-fore, anisotropic acousto-optic devices can be operated deeper in the Braggs regime (higher efficiency) over a wider acoustic bandwidth (higher resolution) than is possible with isotropic acousto-optic devices without acoustic beam steering. Anisotropic Bragg deflectors have been constructed in the past from other materials,[5] but, to the authors' knowl-edge, TeO$_2$ is the first practical anisotropic acousto-optic material.

The overall design of our TeO$_2$ deflector is the same as that of War-ner, et al[2]; however, the details of the crystal-growth conditions, the transducer design, and its bonding are somewhat different. These de-tails will be reported in a separate publication at a later date.

Results

The acousto-optic interaction length of our TeO$_2$ deflector is 0.225 cm. This interaction length is sufficiently long to allow operation deep in the Bragg regime over an acoustic bandwidth in excess of an octave. The useful sweep band was found to be 65 MHz wide, extending from 30 to 95 MHz. The optical aperture used was 0.5 cm. Then the dif-fraction-limited resolution is $N = 524$ spots ($v = 0.62 \times 10^5$ cm/sec)[3], which corresponds to a limiting TV resolution in excess of 10 MHz (52 μsec active line time).

Fig. 1 shows the deflector roll-off characteristics when it is operated at television horizontal scan rate. The upper trace shows a horizontal ramp with rf frequency markers superimposed on it. These markers are spaced 10 MHz apart; the marker on the extreme left corresponds to 90 MHz and the marker on the extreme right corresponds to 30 MHz. The lower trace shows the deflected light intensity as a function of rf frequency (or horizontal sweep time). The average rf power input was approximately 50 mW, and the average deflection efficiency, defined as

the average deflected optical power divided by the optical power transmitted through the deflector with rf off, was 50%. The incident light (4880 Å) was circularly polarized.
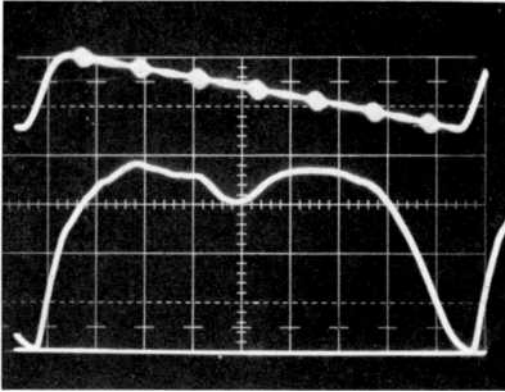

Fig. 1—Roll-off characteristics of the TeO₂ horizontal deflector. Horizontal scale is approximately 7 μsec, or approximately 8.75 MHz acoustic sweep per major division. Upper trace is horizontal deflection ramp signal with rf frequency markers spaced 10 MHz apart superimposed on it; extreme left marker: 90 MHz, extreme right marker: 30 MHz. Lower trace is deflected light intensity when the average deflection efficiency is 50%. Optical wavelength is 4880 Å.

The peak deflection efficiency in the swept mode, shown in Fig. 1, is in excess of 70%. The figure clearly shows a central dip, indicating a reduction in deflection efficiency at the midband rf frequency. This midband dip has been analyzed by Warner et al[2]; it is due to two-phonon scattering. Warner et al concluded that if a flat response (less than 20% dip) is desired, operation of the deflector must be restricted to a maximum efficiency of approximately 40%. Their conclusion is correct, provided that the deflector is operated in a random-access mode or at slow scan rates. At television rates, however, as our data indicates and as will be explained below, the deflection efficiency need not be restricted to this low a value.

In the scanned mode, the depth of the central dip depends on the ratio of the frequency width of the midband dip* to the bandwidth of the acoustic waves that occupy the optical aperture at a given time.

---

* Here we define the frequency width of the midband dip as that frequency width of the midband reduced-deflection-efficiency region (due to two phonon scattering) which is observed in static (i.e. nonscanned) measurements of the deflection efficiency versus rf-drive-frequency characteristics.

If this bandwidth ratio is much less than unity, then the effect of the midband dip is that of a narrow aperture stop that moves across the optical aperture with the sound velocity. The physical width of this equivalent moving aperture is equal to the width of the optical aperture multiplied by the bandwidth ratio. Such a narrow moving aperture will have very little effect on the midband deflection efficiency. It will have some effect on the modulation transfer function of the deflector, but as our results indicate, this effect is also negligible.
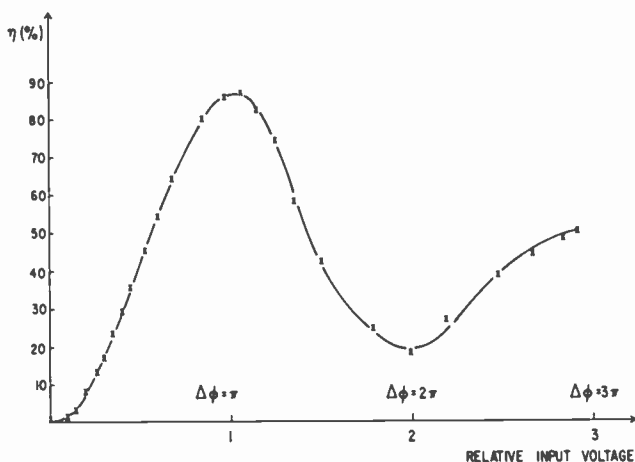

Fig. 2—The deflection efficiency, η, of the TeO_2 horizontal deflector at 75 MHz sound wave frequency as a function of rf drive level (optical wavelength is 4880 Å).

The width of the useful optical aperture of our TeO_2 deflector is 0.5 cm. When the deflector is operated at television rate (63.5 μsec horizontal line time) and at its maximum attainable resolution (65 MHz acoustic sweep for 3 dB roll-off), the acoustic bandwidth appearing across the aperture at a given time is approximately 10 MHz. From static (not swept) measurements of the deflection efficiency as a function of rf frequency we found that at 70% peak efficiency the deflection efficiency at the central dip is approximately one half of the peak value, and that the dip is approximately 2.5 MHz wide. Therefore, the effect of the central two-phonon scattering on the deflector performance is equivalent to moving a stop that has 50% transmission and covers 25% of the aperture, across the optical aperture. Therefore, the midband dip should be approximately 12.5% deep and its duration should correspond to 10 MHz rf sweep. The data shown in Fig. 1 is in good agreement with these expectations.

The deflection efficiency at a constant 75-MHz rf frequency, as a function of rf drive level, is shown in Fig. 2. Again, 4880Å circularly polarized light was used. The rf power required for 70% deflection efficiency is approximately 40 mW. (The deflector admittance at 75 MHz was 2.4×10^{-2} ohms^{-1} and was purely resistive.) At approximately 70 mW of rf drive level, a maximum deflection efficiency of
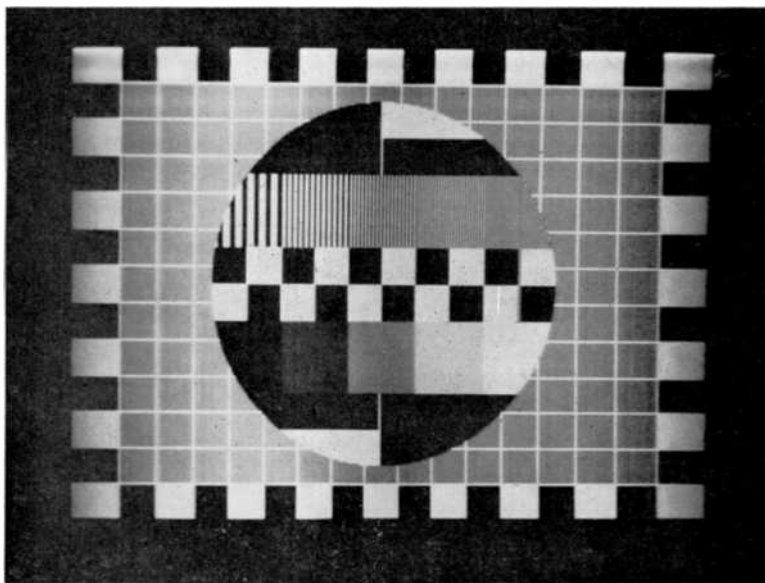

Fig. 3—Television test pattern produced by the laser scanner, indicating the shading characteristics. This pattern was photographed in reflection from a viewing screen.

86% is reached; at higher drive levels the deflection efficiency decreases, indicating that at these levels the induced phase shift is $\Delta\phi > \pi$ (the deflection efficiency is theoretically given by sin^2 ($\Delta\phi2$)). At still higher rf drive levels, the deflector performance deviates from that of an ideal Bragg device—the intensity of the second-order beam increases and the minimum diffraction efficiency at $\Delta\phi = 2\pi$ does not reach zero.

The anisotropic Bragg device was incorporated into the TV-rate laser scanner described previously.[1] The only additional modification of this scanner apart from the replacement of the previously used lead molybdate deflector by the new TeO$_2$ deflector, consisted of introducing a quarter-wave plate between the intensity modulator and the first lens of the optical chain. This quarter-wave plate changes the linearly polarized beam that exits from the modulator into the circularly polar-
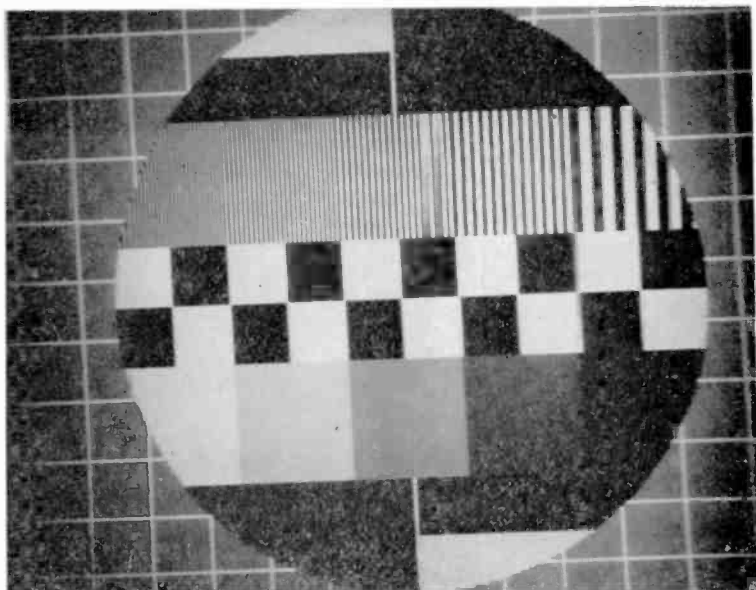
Fig. 4—Central portion of the test pattern shown in Fig. 3, indicating the image definition and resolution capability of the laser scanner. The frequency bursts correspond to 1, 2, 3, 4, and 5 MHz square-wave video input signals. This pattern was photographed in transmission from a viewing screen.

Fig. 5—Photograph of a typical television test subject displayed by means of the laser scanner on a viewing screen.

ized beam needed for the most efficient operation of the TeO_2 device. The overall optical efficiency of the scanner was found to be 14%, without antireflection coating of the deflector. Photographs of sample images produced by the scanner on a viewing screen are shown in Figs. 3, 4, and 5. Fig. 3 was photographed from a reflecting screen; it shows a complete test pattern and indicates the overall shading characteristics. Fig. 4 was photographed from a ground-glass transmission screen; it shows the central region of the test pattern and indicates the image definition and resolution capabilities of the scanner. In Figs. 3 and 4, the frequency bursts correspond to 1, 2, 3, 4, and 5 MHz square-wave video inputs signals. Fig. 5 shows a standard test subject.

Conclusion

Anistropic TeO_2 Bragg devices are excellent deflectors for TV-rate laser scanners. They operate at low rf drive power levels, are efficient, require small optical apertures, and don't require acoustic beam steering to attain high enough resolution to produce high-quality television images.

References:

[1] I. Gorog, J. D. Knox, and P. V. Goedertier, "A Television Rate Laser Scanner. L," **RCA Review,** Vol. 33, No. 4, p.   , Dec. 1972 (this issue).

[2] A. W. Warner, D. L. White, and W. A. Bonner, "Acousto-Optic Light Deflectors Using Optical Activity in Paratellurite," **J. Appl. Phys.**, Vol. 43, p. 4489, No. 11, Nov. 1972. (Also see: D. L. White, D. Maydan, and A. W. Warner, VII International Quantum Electronics Conf., May 8-11, 1972, Paper No. T.5, Digest of Technical Papers, p. 92.)

[3] N. Uchida and Y. Ohmachi, "Acousto-Optical Light Deflector Using TeO_2 Single Crystal," **Japan J. Appl. Phys.,** Vol. 9, p. 155 (1970).

[4] R. W. Dixon, "Acoustic Diffraction of Light in Anisotropic Media," **Proc. Symposium on Modern Optics,** Polytechnic Press of the Polytechnic Inst. of Brooklyn, N. Y., 1967, pp. 265-286.

[5] E. G. M. Lean, C. F. Quate, and H. J. Shaw, "Continuous Deflection of Laser Beams," **Appl. Phys. Lett.,** Vol. 10, No. 2, p. 48, 15 Jan. 1967.

Thin-Film Lasers

J. P. Wittke

RCA Laboratories, Princeton, N.J.

Abstract—The requirements on materials, pumping sources, and geometrical configurations that must be met in the development of practical thin-film laser light sources are discussed. Active materials with "100% doping" of the active ions will be required in special lattices that do not lead to concentration quenching of the fluorescence. Single-crystal materials will probably be required. Neodymium offers the most promise for the active ion. Incoherent pumping sources are considered for practical reasons (regardless of the spectral output of the source, only a small portion of the pump power can be effectively utilized). Heat dissipation, gain saturation and feedback methods are also discussed in connection with these devices. Many difficult material and crystal-growth problems will have to be solved before thin-film lasers can be considered useful, but they offer hope of providing a new and valuable class of optical sources.

Introduction

Recently, lasers have been demonstrated in which the optical waves are confined to single-waveguide modes of a thin-film structure.[1-5] Interest in lasers with such a geometry has been stimulated by the recent activity in the field of integrated optics, which concerns the processing of light signals in an optical system confined to a small planar region on a substrate chip. If integrated optics techniques are to find application in long-distance, high-data-rate communications

systems, some method of amplifying and/or regenerating signals weakened by propagation losses is required. Thin-film laser amplifiers seem to be the only way in which this can be done practically. However, the possible applications of thin-film lasers are much broader than their use in integrated optics. They can, in principle at least, provide a cheap, compact, efficient source of coherent radiation that can be used for numerous purposes: for alignment, holographic read-out, image-processing systems, card readers, etc. They can have many of the characteristics and virtues of injection lasers (which may indeed be considered a form of thin-film laser), but with better mode control than has yet been attained with injection lasers.

It is not clear, however, that useful thin-film lasers can be made. The basic problem is in providing enough gain in a thin-film device to overcome the losses that occur in single-mode propagation in thin films. A high gain per unit length of device implies a large concentration ΔN of excited centers in the film. (The active centers can be located either in the high index of refraction film that forms the optical waveguide or in the adjoining substrate. For convenience, the present discussion will be couched in terms of an active high-index film; the case of an active substrate will be discussed later.) One obtains a large ΔN by pumping a material with a high density N of potentially active centers at a high rate.

Excitation can be provided in several ways—optical pumping, direct injection (as in semiconductor lasers), and electron-beam pumping. Since injection lasers are a well-known type of device, they will not be considered in this paper. Similarly, while electron-beam-excited lasers have been demonstrated, problems associated with the required vacuum system (and possibly with laser degradation under the electron-beam bombardment) make this approach unattractive, and it, too, will not be considered further here. Thus, this paper is concerned with *optically excited* thin-film lasers only.

It is appropriate at this point to consider the present "state of the art". The need for such devices has been recognized, and several attempts have been made to meet it. Dye molecules have been dissolved in plastic films (e.g., rhodamine 6G in polyurethane) and pumped by pulsed lasers (nitrogen, ruby, or doubled YAG:Nd).[1-3] However, not only must such lasers be operated in a pulsed condition, but, after about 10^5 pulses, the dye decomposes and laser oscillation ceases.[6] This approach is clearly ruled out unless much more stable dyes can be found. To avoid the decay problem, liquid dye solutions interacting with the evanescent part of the guided-wave mode, with decomposed dye replaced by diffusion or circulation, have been proposed.[4] This

approach does not seem very practical. A neodymium-doped glass film has also been used as the active medium[5] (neodymium-doped glass fibers were made to oscillate a number of years ago). The gains attainable are rather low, however, and the need for intense flash-lamp excitation limits operation to a relatively low pulsed rate. For applications where such pulsed operation is satisfactory, it would probably be more satisfactory to use an alternative system in which YAG:Nd is the active substrate material, with the waveguide formed by depositing on the YAG a thin film of low-loss material of slightly higher index. By adjusting the film index and thickness, a mode of propagation can be achieved in which most of the optical energy propagates in the substrate, rather than in the film. Nevertheless, for most purposes, a continuously operating amplifier or oscillator, with a suitable long-life excitation source, is required. This is the case even for pulse-modulation communications applications.
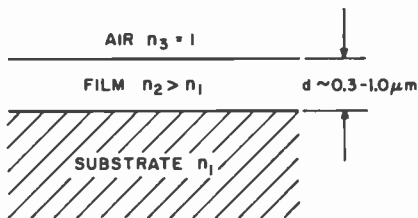

Fig. 1—Geometry of a thin-film laser (n_1, n_2, and n_3, respectively, are the indexes of refraction of the substrate, film, and air).

An Illustrative Example

To give some feeling for the type of laser envisioned and some of the problems involved, consider a thin film of high-index material consisting of a "100%-doping" laser host, supported on an (inert) substrate of lower index. No protective cladding is assumed over the active film. Thus, the situation is as indicated in Fig. 1. Optical propagation in only one (TE_0) mode is assumed; with a reasonable choice of materials, this implies a film thickness d of the order of one-half micrometer. A laser wavelength of 1 micrometer and a pump wavelength of 620 nanometers will be assumed, with the gain provided by rare-earth ions in the film. For "100% doping", most materials have ion concentrations N of about 10^{22} cm^{-3}. Taking a transition cross section of $\sigma = 10^{-19}$ cm^2 and an optical linewidth of 3 nanometers as typical, the film will have an absorption coefficient of the order of $\alpha = 10^3$ cm^{-1} for the

pump radiation. Since a thickness of $d = 5 \times 10^{-5}$ cm has been assumed, only about 5% of the incident pump radiation can be absorbed (in one pass). This can roughly be doubled by the use of a reflector.

Despite the fact that lasers have generally been used to pump active films,[1-3] we assume that the excitation source is incoherent. This assumption is made on the basis of considerations of efficiency, reliability, complexity, size, and cost. It is obvious that a gas (or perhaps a frequency-doubled YAG:Nd) laser, used as a pump, adds one more quite inefficient element to the system, and clearly is undesirable with regard to the other mentioned characteristics. It is possible that a fortuitous coincidence of pump laser and thin-film laser absorption wavelengths would permit all of the pump light to be usefully absorbed, resulting in no overall loss in system efficiency because of the laser pump. Moreover, with a coherent pump, pumping in a waveguide mode can perhaps permit efficient use of space in the neighborhood of the optical circuit and can ease cooling requirements. Nevertheless, although coherent pumping should be kept in mind as a possibility, it is unlikely to be used in any practical system.

There are perhaps only two practical light sources—tungsten filament–iodine vapor incandescent lamps, and incoherent semiconductor electroluminescent diodes. Both can be operated continuously with high surface brightness and long lifetime. Assuming an effective tungsten filament temperature of 3200°K and an emissivity of 0.4, the power emitted into a 3-nanometer linewidth ranges from about 0.15 watt/cm² in the blue-green to about 0.5 watt/cm² in the near infrared (900 nanometers). An incoherent electroluminescent diode (at 900 nanometers) can give about 10 watts/cm² in a 50-nanometer bandwidth or 0.6 watt/cm² in a 3-nanometer width.

If we assume that 20 milliwatts/cm² can be absorbed in each pump transition and that ten pumping transitions are effective, 2-eV pump photons (620 nanometer pump) correspond to about 6.2×10^{17} ions excited/cm²-sec. The density of excited ions ΔN will depend on the lifetime τ of the upper laser level. For $\tau = 10^{-3}$ sec, the above figures correspond to $\Delta N = 1.25 \times 10^{19}$ cm^{-3} excited ions in the film. A laser transition cross section of $\sigma = 10^{-19}$ cm^{-2}, therefore, gives a gain coefficient in the active film material of $\alpha = 1.25$ cm^{-1}, or 5.4 dB/cm. It must be remembered that all of the numbers leading to this estimate are little more than crude guesses and that any actual system may correspond to a significantly different gain. However, the above figures do point up some of the problems and indicate why active materials with "100% doping" may be required; any significantly lower doping level will result in gain coefficients that may well be less than the

corresponding loss coefficients associated with imperfections of various sorts in the film.

Laser Materials

The ability to make useful thin-film lasers hinges primarily on whether or not suitable active materials can be obtained in appropriate configurations. The problem is basically one of attaining sufficient gain with continuous pumping. Neodymium-doped YAG is the best crystal laser material that has been found to date. In Appendix I, the available "bulk" gain is computed for a tungsten-lamp-pumped YAG crystal doped with 1.2% neodymium. It is shown there that gains of only 0.02 dB/cm can be achieved. Thus, even the best known crystal laser material is inadequate, and new classes of materials must be considered.

Host Materials

As indicated above, to get useful gains, "100% doping" probably must be used. However, concentration-quenching phenomena generally become important when doping levels of active ions are increased much above the 1% level, in most systems.

There are at least two possible solutions to the problems associated with concentration quenching. Van Uitert and Iida[7] have shown that if the crystal structure of a "100% doped" material is such that neighboring rare-earth ions are separated by other, suitably inert ions, the f-shell electronic transitions of interest to lasers are essentially those of isolated ions, and are not quenched. A study of several mixed-oxide lattices showed that nearest-neighbor sites for the rare-earth ions, or sites separated only by one oxygen ion, can lead to quenching, while $(WO_4)^{2-}$ groups, for example, can provide effective isolation. Thus, a proper choice of crystal host may eliminate the problem, e.g., van Uitert found essentially no concentration quenching of Eu^{3+} ions in $NaEu (WO_4)_2$. P. N. Yocom has suggested[8] that other materials, such as alkali rare-earth halides (e.g., K_3NdCl_6), might prove equally acceptable for this purpose.

Still another possible solution exists. It is generally supposed (see, e.g., van Uitert[7]) that quenching can occur when the excitation energy can be transferred to a coupled ion pair that, because of the coupling, has many more energy levels and interacts much more strongly with the lattice vibrations. Thus, concentration quenching occurs when excitation energy can migrate from the ion that absorbed the pump radiation to an ion pair that can give it up to the lattice as thermal

vibrations. Dipolar (and other) coupling mechanisms that can transfer energy between sites have been discussed in detail by Forster[9] and by Dexter.[10] At "100% doping", in many lattices, one can expect excitation energy to be effectively completely delocalized, moving freely throughout the whole volume of the crystal. However, this does not necessarily imply a rapid quenching of luminescence. With a perfect crystal, the individual ion energy levels will be broadened into bands, but the fluorescent efficiency of excitation energy in one of these bands may aproach unity. This is apparently the explanation of high (29%) fluorescent efficiency observed in HoF_3 by Devor et al[11] and in $PrCl_3$ by Varsanyi.[12] Both materials have exhibited laser action. What would appear to be of the utmost importance in all such materials is the avoidance of all impurity centers at which the electronic excitation can be quenched to lattice vibrations. Hence, disorder, dislocations, and impurities can form de-excitation centers, and a high crystal quality, coupled with extreme purity, may be required.

Because fluorescence quenching is a serious problem, the use of amorphous materials, with their inherent high disorder, may be ruled out. If this is so, the problem of making thin-film lasers becomes much more severe, for many methods of preparing thin films with the requisite thickness control (for example, evaporation) generally result in amorphous (or polycrystalline) films. On the other hand, if single-crystal films are required, the problems are legion. The difficulties of growing single-crystal films by liquid- or vapor-phase epitaxy are well known. Generally, such films grown by hetero-epitaxy on substrates of a different material are subject to mismatchs between substrate and film, in lattice parameters and/or in thermal expansion coefficients. This generally leads to strained, imperfect films, with high dislocation densities and high optical losses when used as optical waveguides. Better films can be grown by homo-epitaxy on (undoped) substrates of the same material as the active film. The resultant index discontinuity from active film to substrate is apt to be very small, however, and may provide inadequate optical waveguiding. Thus, in addition to the usual problems associated with epitaxial film growth, the use of such films as thin-film lasers introduces yet other constraints.

One possible solution is to use some variation of Bridgman–Stockbarger growth techniques to produce single crystals of materials. To adapt these methods to the growth of contaminant-free thin films of sub-micrometer thickness would be no easy task, however. The fluorides, which are one class of materials that might prove desirable, are stable in normal atmosphere, but when molten, attack many materials that might provide suitable substrates, such as silicates. This problem

can be reduced or eliminated by use of, e.g., the corresponding chlorides or bromides. These have lower melting points than the fluorides, making them easier to work with. However, they are generally attacked by atmospheric moisture, and would have to be grown and used in some encapsulated form.

Other possibilities exist for the preparation of suitable materials for thin-film lasers, but perhaps enough has been said to indicate the nature of the challenge presented.

Active Ions

As implicity assumed above, trivalent rare-earth ions offer the most hope for the active centers. Organic materials, especially those containing hydrogen (not completely fluorinated, for example), are apt to be unstable under conditions of laser pumping. Transition-metal ions tend to interact more with their surrounding lattice than do rare-earth ions, making the problem of attaining high fluorescent efficiency more severe. Finally, divalent rare-earth lasers have only been operated at cryogenic temperatures. Trivalent rare-earth ions will therefore be assumed in all of the following.

In deciding which rare-earth ion is most promising, the energy level schemes must be considered. Several ions can be ruled out immediately: cerium has only one excited $4f$ electronic state, and this is too low in energy (0.28 eV) to be useful; promethium is radioactive; and gadolinium has no transitions in the visible or infrared, the first level lying about 4.0 eV above the ground state.

Ytterbium can also be ruled out as a choice for the active ion since relatively weak, cw pumping is being considered. From the estimate made above, assuming ten pumping transitions are effective (probably a high number for Yb), only about 200 milliwatts/cm² of pump power can be absorbed. This corresponds to $\Delta N = 1.9 \times 10^{19}$ cm⁻³ for $\tau = 10^{-3}$ and a 1.3-eV pump photon energy. For a total ion concentration $N = 1.9 \times 10^{22}$ cm⁻³, this gives $\Delta N/N = 10^{-3}$ for the fraction of Yb ions that can be maintained in an excited state. The ground $^4F_{7/2}$ state of ytterbium is generally split into four Kramers doublets. The thermal population N' of the highest of these sub-levels, at an energy ΔE above the ground state, is therefore

$$N' \geqslant \frac{1}{4} N \exp\left(-\frac{\Delta E}{kT}\right).$$

To have net stimulated emission,

$$\Delta N \geqslant N'$$

or

$$10^{-3} \geqslant \frac{1}{4} \exp \left(- \frac{\Delta E}{kT} \right).$$

This condition can only be met if $\Delta E \geqslant 1100$ cm^{-1} for room-temperature operation. This is greater than has been observed in several materials.[13,14] Thus, it appears that the $^4F_{7/2}$-state splittings are not large enough to depopulate the upper level sufficiently for cw (four-level) laser action.

In choosing among the remaining ions, one must consider cross-relaxation processes, as these can be of great importance in quenching luminescence. In cross relaxation, an ion in an excited state can interact with an unexcited ion (of the same or of a different kind) and exchange some of its energy by a radiationless multipolar process, leaving the originally excited ion in a lower energy state and exciting the originally unexcited ion to some state above its ground level. Since energy must be conserved in this transfer process, there must be an equality of the transition energies involved or phonons must simultaneously be emitted or absorbed. Since the coupling of the electronic states of the rare-earth ions to the lattice vibrations is generally quite weak, this relaxation process generally is important only when there is a close match (resonance) of the two transition energies. Ions whose energy level scheme is such as to provide such resonances will be much less favorable for obtaining laser action than ions that do not provide close resonances. It is important to realize that higher-order cross-relaxation processes can exist between three (or even more) ions, with, e.g., one excited ion giving up part or all of its excitation energy to *two* unexcited ions simultaneously, leaving both of them excited.

The strength of these cross-relaxation processes depends critically on just how close to exact resonance the various possible transitions are.[15] The separations between the various $4f$ electronic levels in rare earths are approximately the same, regardless of host.[16] In any specific system, however, just how close resonance is approached, and hence how important the various cross-relaxation processes are, can only be determined by detailed spectroscopic studies.[17]

Of all the remaining trivalent rare-earth ions, only neodymium, holmium, and thulium have given cw laser action,[18] and of these only neodymium lasers have been operated cw at room temperature. Thus, this ion seems the most promising for such thin-film lasers. However, if only neodymium can be used, the resultant infrared output beam

poses detection problems that might rule out the use of such lasers for many otherwise promising applications.

Location of Active Centers

a. High-Index-of-Refraction Film

There are several advantages in placing the active centers in the high-index film: (1) the optical electromagnetic fields are highest here and hence couple best to the active centers, (2) heat-removal geometry is optimized, and (3) the least active material is required. To avoid dispersive effects, one wants to operate in a single waveguide mode; the TE_0 mode will be assumed. There will therefore be a (displaced)
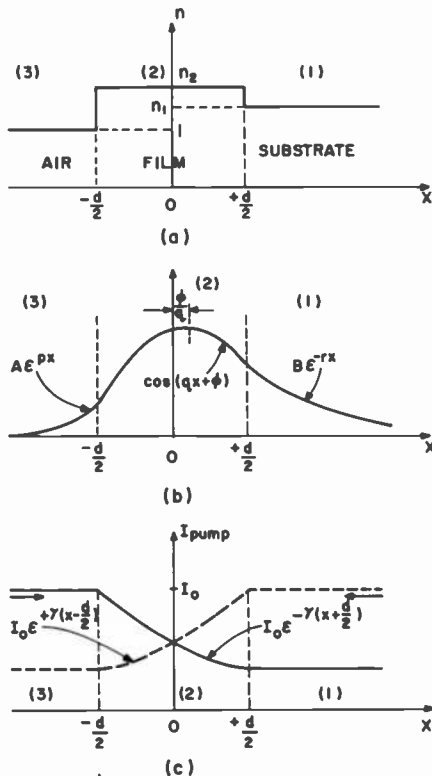
Fig. 2—Distributions across the thin-film structure: (a) index of refraction variations; (b) electrical field distribution in the guided optical wave (TE_0 mode); (c) distribution of pumping radiation intensity for light incident from the substrate (dashed line) and for light incident from the air (solid line). The density of active centers in the film is proportional to the pumping light intensity (assuming no saturation).

sinusoidal distribution of energy across the film in the optic wave and, because of the absorption of the pump radiation, an exponential distribution of excited ions across the film. This is illustrated in Fig. 2. (In principle, one could use pump radiation in a waveguide mode[4] as well, but this requires a coherent pump source and thus violates the assumptions behind this paper.) Since the largest optical field is not at the film surface, there will be an optimum absorption coefficient γ for the pump radiation to maximize gain. Assume the pump light is incident from the substrate side of the film and that the pump intensity distribution is given by

$$I = I_o \exp\left[-\gamma\left(x + \frac{d}{2}\right)\right].$$

The excited state population density ΔN is then given by:

$$\Delta N = -\frac{\tau}{\hbar\omega_p}\left(\frac{dI}{dx}\right) = \frac{I_o\tau}{\hbar\omega_p}\gamma\exp\left[-\gamma\left(x + \frac{d}{2}\right)\right],$$

where τ is the lifetime of an excited ion and $\hbar\omega_p$ the energy of a (representative) pump photon. The effective gain coefficient α_{eff} in the waveguide is then

$$\alpha_{eff} = \frac{\displaystyle\int_{-d/2}^{+d/2} n_2^2 E^2(x)\Delta N(x)\sigma dx}{\displaystyle\int_{-\infty}^{\infty} n^2(x)E^2(x)dx}.$$

Here $n(x)$ is the index of refraction at the position x. For the TE_0 mode, the fields in the various regions of the waveguiding structure are given by Anderson,[19] whose notation will be used. In the thin film,

$$E_2(x) = \cos(qx + \phi),$$

while in the substrate and in the air above the film (see Fig. 2) the fields are, respectively,

$$E_1(x) = \frac{q\lambda_o}{2\pi\sqrt{n_2^2 - n_1^2}} \exp\left[-p\left(x - \frac{d}{2}\right)\right]$$

and

$$E_3(x) = \frac{q\lambda_o}{2\pi} \sqrt{\frac{n_2^2 - n_1^2}{n_2^2 - n_3^2}} \exp\left[+r\left(x + \frac{d}{2}\right)\right],$$

where λ_o is the free-space wavelength of the optical wave. All expressions are considerably simplified by putting them in a normalized, dimensionless form. This is done by multiplying all distances by the factor $(2\pi/\lambda_o)\sqrt{n_2^2 - n_1^2}$, i.e.,

$$X \equiv \frac{2\pi\sqrt{n_2^2 - n_1^2}}{\lambda_o}\, x$$

$$D \equiv \frac{2\pi\sqrt{n_2^2 - n_1^2}}{\lambda_o}\, d$$

$$Q \equiv \frac{\lambda_o q}{2\pi\sqrt{n_2^2 - n_1^2}},$$

and similarly for R, P, and Γ. In terms of such dimensionless parameters, the effective gain coefficient becomes, for pumping light incident on the film from the substrate side,

$$A_{eff} = \left(\frac{I_o\sigma\tau}{\hbar\omega_p}\right) n_2^2 \int_{-D/2}^{+D/2} \Gamma \exp\left[-\Gamma\left(X + \frac{D}{2}\right)\right] \cos^2(QX + \phi)\, dx$$

$$\left\{ n_1^2 \int_{+D/2}^{\infty} Q^2 \exp(PD) \exp(-2PX)\, dx + n_2^2 \int_{-D/2}^{+D/2} \cos^2(QX + \phi)\, dx \right.$$

$$\left. + n_3^2 \int_{-\infty}^{-D/2} \frac{Q^2}{\eta} \exp(RD) \exp(2RX)\, dX \right\}^{-1}$$

where

$$\eta \equiv \frac{n_2{}^2 - n_3{}^2}{n_2{}^2 - n_1{}^2} \ .$$

From this,

$$A_{\text{eff}} \propto \left(\frac{2Q}{\Gamma}\right) \frac{\left\{ \exp\left(-\Gamma D\right) \left[\frac{2RQ}{\eta} - \frac{Q\Gamma}{\eta} - \frac{2Q}{\Gamma} \right] + \left[2QP + Q\Gamma + \frac{2Q}{\Gamma} \right] \right\}}{\left[\left(\frac{2Q}{\Gamma}\right)^2 + 1 \right]}$$

$A_{\text{eff}} \propto \Gamma$ as $\Gamma \to 0$.

Since[19]

$$P \equiv \sqrt{1 - Q^2}, \quad R \equiv \sqrt{\eta - Q^2}.$$

and

$$QD = \cos^{-1} Q + \cos^{-1}\frac{Q}{\sqrt{\eta}}$$

for TE_0 modes, there will be an optimum γ for any given thin-film structure, where d, the n_i's, and λ_o are known, determined by maximizing the expression for A_{eff} above. This can be readily, if tediously, found numerically for different choices of the parameters η and Q. Similar calculations can be made for the case where the pump radiation is incident from the "air side". In this case, since the effect of the substrate is to move the peak optical field nearer to the film–substrate boundary than to the film–air interface (see Fig. 2), a somewhat lower attenuation coefficient for the pump radiation is desired. The results of calculations for the two cases $n_1 = 1.5$, $n_2 = 1.6$ and $n_1 = 1.5$, $n_2 = 1.8$ are shown in Fig. 3, where the variation of (normalized) gain coefficient A with the pump radiation absorption coefficient is plotted for the pump light incident from the substrate and from the air sides. From this, it is apparent that, regardless of the pump absorption coefficient, higher gains are *always* achieved when the pump light comes from the substrate side. However, for values of $\Gamma < 0.02$, there is no significant difference between *any* of the curves. In Fig. 4,
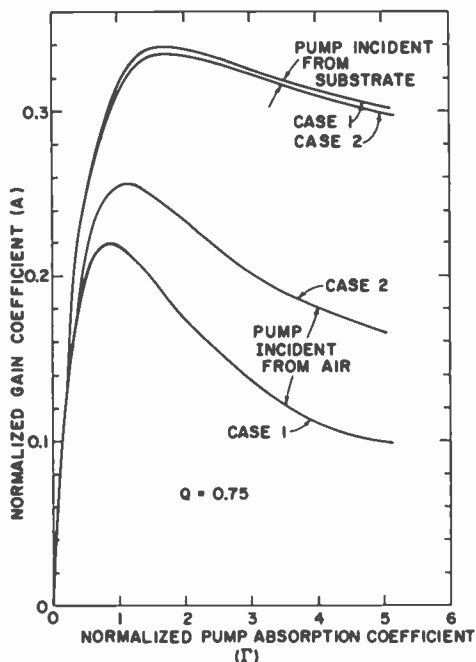
Fig. 3—Normalized gain coefficients as a function of pump absorption coefficient (constant incident pump intensity) for the two cases (1) $n_1 = 1.5$, $n_2 = 1.6$, and (2) $n_1 = 1.5$, $n_2 = 1.8$. The two different directions of incident pump radiation, from the substrate side and from the air side, are shown. The curves are for a value of Anderson's[19] Q-parameter of 0.75.

the optimum pump absorption coefficients are shown as a function of the Q-parameter, for the same cases.

In Fig. 5, the (normalized) film thickness is plotted against the Q-parameter. From this, it can be seen that a reasonable choice of thickness to obtain TE_0 single-mode operation corresponds to $Q \sim 0.75$. (This value was assumed for the curves of Fig. 3.) For this value, $D \sim 2.5$, and at the optimum absorption coefficient (Fig. 3), $\Gamma_{opt} \sim 1$ or $\Gamma_{opt} \sim 1.7$, depending on the direction of incidence of the pump light. In either case, over 95% of the incident pump radiation is absorbed under optimal conditions. However, even with "100% doping", the transitions in rare earths are so weak that the optimum absorption cannot be attained ($\Gamma_{max} \sim .03$). Thus, as indicated in Fig. 3, one must operate far from the maximum, at conditions where the effective gain coefficient is roughly proportional to the absorption coefficient ($A_{eff} \propto \Gamma$) and where it does not matter whether the pump radiation is incident from the substrate or air side.

It might be thought that by making the active film thick enough
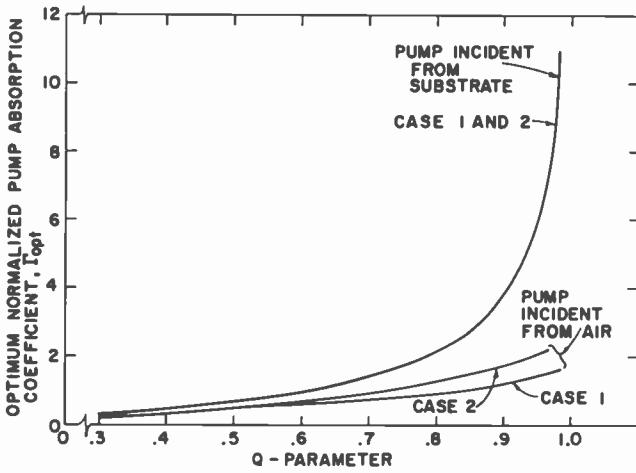
Fig. 4—Optimum (normalized) absorption coefficient for pumping radiation as a function of Anderson's Q-parameter for the cases of Fig. 3. Film thickness decreases as Q increases, reaching the TE_0 mode cut-off at $Q = 1.0$ (see Fig. 5).
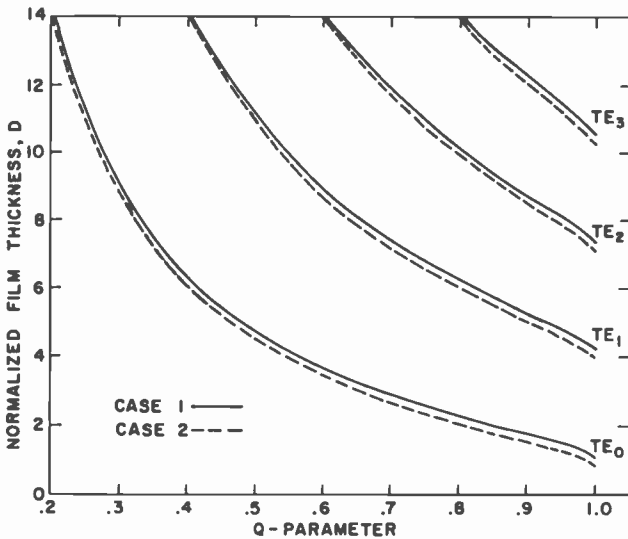

Fig. 5—Normalized film thickness as a function of Anderson's Q-parameter for the first few TE_0 modes for the two choices of film and substrate indexes of Fig. 3.

so that essentially all the pump radiation is absorbed, the gain co-efficient would increase. This is true in that as the film thickness is increased, a greater fraction of the optical energy is found in the active region, but in no case can the gain coefficient exceed that of the "bulk" material pumped to the same excitation level.

b. Substrate

If the active material can only be grown as a (thick) single crystal and cannot conveniently be made in a thin-film form, it can only be used by making the substrate the active region and applying a high-index film to one surface of it to form the waveguide.

If the active centers are located in the substrate, the situation is much simpler to analyze. Since now the maximum optical field strength (in the substrate) occurs at the boundary of the high-index thin film and decays monotonically with depth, the higher the pump absorption coefficient, the better. As before, one wants to maximize

$$A_{eff} \propto \int_{0}^{\infty} \Gamma \exp{(-\Gamma X)} \exp{(-2PX)} \, dx = \frac{\Gamma}{2P + \Gamma},$$

which is a monotonically increasing function of Γ. Again, $2P \gg \Gamma$, and $A_{eff} \propto \Gamma$. Now the pump radiation must be incident from the air side to avoid attenuating the pump in the useless part of the substrate that does not couple to the optical wave.

Heat Dissipation

For the case of an active thin film, all pumping radiation not absorbed in the film is presumably transmitted through the entire structure and need not be considered further. (In practice, heat-sinking structures used to remove the heat may themselves absorb most of the unused pump radiation, and so may have to remove effectively *all* the original pump radiation.) For Nd^{3+} ions, an "effective" pump energy is about 1.7 eV/photon. For our estimated 6×10^{17} ions excited/cm²-sec, this corresponds to about 0.16 watt/cm² absorbed/pump line, or perhaps 200 milliwatts/cm² for the total absorption. Neglecting the part re-moved as radiation, this energy must be conducted away as heat through the film and by the substrate. The film itself is so thin ($\sim 5 \times 10^{-5}$ cm) that one can neglect temperature gradients across it. For a 5-millimeter-thick glass substrate ($k \sim 10^{-2}$ watt/cm-°C), a

temperature drop of about 10°C across the substrate can be expected. Since the above estimates are conservative, with adequate cooling (e.g., flowing water) at the bottom of the substrate, the active film can be kept within a few degrees of ambient.

For the case of the substrate containing the active ions, it has been shown that one cannot have more than 5-10% of the incident energy (at the pump lines) absorbed in a thickness corresponding to the penetration of the optical waves into the substrate. Thus 90-95% of the pump light will be absorbed in the substrate at depths useless for contributing to the gain. This increases the heat loading by a factor of from 10 to 20 and proportionately increases the temperature drop across the substrate. The cooling problem clearly is much more serious in this case, and cooling may have to be applied directly to the thin film itself to keep it at (or near) room temperature.

Saturation

A crude estimate can be made of the power-handling capabilities of a thin laser as follows. For propagation of a plane wave through a laser medium with gain, the gain coefficient can be written

$$\alpha = \frac{8\pi\mu^2\Delta N}{\hbar\lambda\Delta\nu},$$

where μ is the transition dipole moment and $\Delta\nu$ is the (homogeneous) linewidth of the transition. Since

$$\alpha \equiv \sigma\Delta N,$$

this can also be written

$$\frac{\mu^2}{\Delta\nu} = \frac{\hbar\lambda\sigma}{8\pi}.$$

The transition will saturate when the optical fields are such that

$$\left(\frac{\mu E}{\hbar}\right)^2 \frac{\tau}{\pi\Delta\nu} \approx 1$$

Here τ is the lifetime of the (upper) laser state. Thus, the saturation field, E_{sat}, is given by:

$$E_{\text{sat}} \approx \left(\frac{8\pi^2 \hbar}{\lambda\sigma\tau} \right)^{1/2}.$$

The corresponding power density P in a plane wave in a medium with index of refraction n is

$$P = \frac{ncE^2}{8\pi}.$$

The saturation power then is

$$P_{\text{sat}} \approx \frac{\pi nc\hbar}{\lambda\sigma\tau}.$$

For $n = 1.8$, $\lambda = 10^4$ cm, $\sigma = 10^{-19}$ cm^2 and $\tau = 10^{-3}$ sec, this is

$$P_{\text{sat}} \approx 1700 \text{ watts/cm}^2.$$

For a beam of width 10^{-2} cm traveling in a thin-film guide of thickness of the order of 10^{-4} cm, this corresponds to a power flow of about

$$P_{\text{sat}} \approx 1.6 \text{ milliwatts}.$$

Feedback

The final topic that will be discussed is how feedback can be applied to a thin-film laser to make it oscillate. For thin-film lasers that have been built thus far, different forms of feedback have been used. Kaminow et al[2] used separated phase gratings (variable index layers) in polymethyl methacrylate, Kogelnik and Shank[1] used distributed feedback (periodic index variations throughout the laser medium), and Bjorkholm and Shank[3] used spatially periodic pumping to provide feedback. The last of these approaches clearly cannot be used with our postulated incoherent pump. With an active, single-crystal thin film, feedback must either be provided at the ends of the active region, by a high-reflectivity-index discontinuity or deposited multilayer film, or along the length of the film by periodic (effective) index variations in the substrate (or in a top-surface cladding.) For example, by coating an (active) high-index film with a polymer in which periodic index variations can be impressed, the evanescent part of the optical wave that penetrates the cladding will "see" the variation and provide feedback. For the case where the substrate contains the active med-

ium, if a periodic variation can be impressed on the high-index film, feedback can be supplied in this way. In either case, well-known techniques appear to provide the feedback necessary to turn a thin-film amplifier into an oscillator.

For a modulated index of refraction, Kogelnik and Shank[1] show that the required modulation to achieve sufficient feedback for oscillation depends on the gain as

$$n_1 = \left(\frac{\lambda_o}{L}\right) \frac{1}{\pi} \frac{\ln G}{G^{1/2}} \,,$$

where L is the length of the distributed feedback region, $G = \exp(2 \, \alpha_o L)$ is the single-pass (power) gain and the index can be written as a function of the distance along the guide z as

$$n = n_o + n_1 \cos Mz$$

with $M = 2k = 4\pi n_o/\lambda_o$, and $n_1 \ll n_o$.

The above indicates that a modulation of the effective index of refraction $n_1 > 10^{-4}$ is required to produce enough feedback to sustain oscillations. This amount of modulation should be readily attainable.

As in the case of the best-known thin-film-geometry laser, the semiconductor injection laser, multimoding may be a severe problem if a collimated beam is desired. However, since the expected gain coefficients are much smaller for the optically excited laser than for the injection laser, a much longer path length is needed, and one can use geometrical effects (e.g., diffraction losses) to mode-select. For example, if a gain length a of about 1 centimeter is used and one confines the distributed feedback index variations to a width b of 0.1 millimeter along the film, one has a structure with a Fresnel number N of

$$N = \frac{a^2}{b\lambda} \approx 1.$$

This is low enough that diffraction losses must be considered, and transverse mode selectivity will occur.

Conclusions

It is clear that many problems must be solved before practical cw thin-film lasers can be made. However, if they can be made at all, they

probably can be made quite cheaply and, with integral distributed feedback, would be free from the mirror alignment problems of other lasers. Thus, successful cw thin-film lasers would represent an important technological advance and would find many applications.

Considerations of gain indicate that new laser materials that approach "100% doping" with active ions will be required. Relatively little study has been given to such concentrated luminescent materials, and spectrocopic work is required to discover materials with suitable properties. Such investigations must include detailed study of quenching and energy-tranfer mechanisms.

Although the considerations given above indicate that it is unlikely that amorphous materials with high concentrations of active ions can possess the requisite fluorescent efficiencies, ease of working with materials in this form dictates that experimental investigations of amorphous systems be carried out. Beyond this, progress will require the active cooperation of skilled materials synthesists, both to grow promising materials in single-crystal form for spectroscopic study and to solve the problems associated with fabricating any material with useful properties into appropriate thin-film configurations.

Appendix 1

To evaluate YAG:Nd, the absorption spectrum of a high-quality YAG:Nd slab (1.2% doping) was measured on a commercial spectrophotometer. All pumping was assumed to occur in the spectral range between 500 and 910 nanometers. The absorption spectrum was convoluted with the emission spectrum of a tungsten–halogen lamp at an effective temperature of 3200°K, assuming a (constant) emissivity of 0.4, giving the total number of photons absorbed per second in a unit cube of YAG. (This assumes a unity optical efficiency of the lamp-focusing geometry and an optically "thin" active material.) The result is a total of 7.8×10^{19} photons/sec absorbed per cubic centimeter. It has been shown[20] that ions decay from all higher excited states to the $^4F_{3/2}$ upper laser levels in YAG:Nd with unity quantum efficiency. Therefore, the concentration of excited ions in the excited $^4F_{3/2}$ states is given by multiplying this number by the observed lifetime of ions in the $^4F_{3/2}$ state, $\tau = 2.30 \times 10^{-4}$ sec.[21] This gives an excited state population density of $\Delta N = 1.79 \times 10^{16}$ cm^{-3}. This figure can then be combined with measured[22] values for the cross sections for the laser transitions at 1.0641 micrometer to give a gain coefficient for bulk YAG:Nd pumped in the assumed way. As shown by Kushida et al,[21] the laser transition is really a com-

bination of two overlapping lines, one originating from the lower $^4F_{3/2}$ level and one from the upper. With the two states thermalized at $300°$ K, the effective transition cross section is

$$\sigma_{eff} = p_u\sigma_u + p_l\sigma_l$$

where σ_i is the cross section for the ith transition, p_i the probability an ion in the $^4F_{3/2}$ level is in the ith state, and u and l refer to "upper" and "lower" states respectively.

$$\sigma_{eff} = .393 \times 8.0 \times 10^{-19} + 0.607 \times 0.46 \times 10^{-19}$$
$$= 3.42 \times 10^{-19} \text{ cm}^2.$$

This gives a "bulk" gain coefficient in the YAG:Nd when pumped as above of

$$\alpha_{gain} = \Delta N \times \sigma_{eff}$$
$$= 0.0061 \text{ cm}^{-1}$$
$$= 0.026 \text{ dB/cm}.$$

Since only part of the optical wave propagates in the film, the single-mode gain coefficient for the guided wave will be somewhat less than this.

References:

[1] H. Kogelnik and C. V. Shank, "Stimulated Emission in a Periodic Structure," **Appl. Phys. Lett**, Vol. 18, p. 152 (1971).

[2] I. P. Kaminow, H. P. Weber, and E. A. Chandross, "Poly (Methyl Methacrylate) Dye Laser with Internal Diffraction Grating Resonator," **Appl. Phys. Lett.**, Vol. 18, p. 497 (1971).

[3] J. E. Bjorkholm and C. V. Shank, "Distributed-Feedback Lasers in Thin-Film Optical Waveguides," Paper ThA1, Topical Meeting on Integrated Optics—Guided Waves, Materials, and Devices, Feb. 7-10, 1972, Las Vegas, Nevada.

[4] E. P. Ippen and C. V. Shank, "An Evanescent Field Pumped Dye Laser," Paper ThA4, Topical Meeting on Integrated Optics—Guided Waves, Materials, and Devices, Feb. 7-10, 1972, Las Vegas, Nevada.

[5] H. Yajima, S. Kawase, and Y. Sekimoto, "Amplification of 1.06 μm Using Nd Glass Thin-Film Waveguide," Paper ThA9, Topical Meeting on Integrated Optics—Guided Waves, Materials, and Devices, Feb. 7-10, 1972, Las Vegas, Nevada.

[6] E. P. Ippen, C. V. Shank, and A. Dienes, "Rapid Photobleaching of Organic Laser Dyes in Continuously Operated Devices," **IEEE J. Quant. Elect.**, Vol. QE-7, p. 178 (1971).

[7] L. G. van Uitert and S. Iida, "Quenching Interactions Between Rare-Earth Ions," **J. Chem. Phys.**, Vol. 37, p. 986 (1962).

[8] P. N. Yocom, private communication.

[9] T. Förster, "Zwischenmolekulare Energiewandrung und Fluoreszenz," **Ann. der Physik**, Vol. 2, p. 55 (1948).

[10] D. L. Dexter, "A Theory of Sensitized Luminescence in Solids," **J. Chem Phys.**, Vol. 21, p. 836 (1953).

[11] D. P. Devor, B. H. Soffer, and M. Robinson, "Stimulated Emission from Ho^{3+} at μm in HoF_3," **Appl. Phys. Lett.,** Vol. 18, p. 122 (1971).

[12] F. Varsanyi, "Surface Lasers," **Appl. Phys. Lett.,** Vol. 19, p. 169 (1971).

[13] R. A. Buchanan, K. A. Wickersheim, J. J. Pearson, and G. F. Herrmann, "Energy Levels of Yb^{3+} in Gallium and Aluminum Garnets. I. Spectra," **Phys. Rev.,** Vol. 159, p. 245 (1967).

[14] G. R. Jones, "Optical Absorption Spectrum and Optical Zeeman Effect in $CaWO_4$: $Yb^3\dagger$," **J. Chem. Phys.,** Vol. 47, p. 4347 (1967).

[15] J. P. Wittke, I. Landany, and P. N. Yocom, "Y_2O_3:Yb:Er—New Red-Emitting Infrared-Excited Phosphor," **J. Appl. Phys.,** Vol. 43, p. 595 (1972).

[16] E. H. Dieke, **Spectra and Energy Levels of Rare Earth Ions in Crystals,** Interscience Publishers, N. Y., N. Y. (1968).

[17] M. R. Brown, J.S.S. Whiting, and W. A. Shand, "Ion-Ion Interaction in Rare-Earth-Doped LaF_3," **J. Chem. Phys.,** Vol. 43, p. 1 (1965).

[18] **Handbook of Lasers,** R. J. Pressley, ed., Chemical Rubber Co., Cleveland, Ohio (1971), Chap. 13, Table 13-5.

[19] W. W. Anderson, "Mode Confinement and Gain in Junction Lasers," **IEEE J. Quant. Elect.,** Vol. QE-1, p. 228 (1965).

[20] R. A. Brandewie and C. L. Telk, "Quantum Efficiency of Nd^{3+} in Glass, Calcium Tungstate, and Yttrium Aluminum Garnet," **J. Opt. Soc. Am.,** Vol. 57, p. 1221 (1967).

[21] J. K. Neeland and V. Evtuhov, "Measurement of the Laser Transition Cross Section for Nd^{3+} in Yttrium Aluminum Garnet," **Phys. Rev.,** Vol. 156, p. 244 (1967).

[22] T. Kushida, H. M. Marcos, and J. E. Geusic, "Laser Transition Cross Section and Flourescence Branching Ratio for Nd^{3+} in Yttrium Aluminum Garnet," **Phys. Rev.,** Vol. 167, p. 289 (1968).

A New Earth-Station Antenna for Domestic Satellite Communications

Peter Foldes

RCA Limited, Montreal

Abstract—The concept, basic design, and measured performance characteristics of a new earth station antenna are described. The feed system with various subreflectors can be used for main reflectors in the 22 to 50-foot-diameter range in a shaped Cassegrainian configuration. The measured data was taken with a 33 1/3-foot-diameter antenna in the 3.7-4.2 GHz and 5.925-6.425 GHz bands. The antenna is capable of sum-mode-based tracking and it has rotatable linear or adaptable quasi-circular polarization modes in single spectrum or spectrum re-use configurations. With added module, the system can provide independently rotatable linear or independently adaptable quasi-circular polarizations for the up and down links of a communications satellite system. The main intended use of the new equipment is in domestic satellite communications systems with relatively simple antenna systems.

1. Introduction

During the first decade of the development of commercial satellite communications systems, earth stations were characterized by large antennas. These systems had monopulse autotracking capability and about 60-dB antenna gain at 4 GHz. The large antenna size was

selected, because initially the available low Effective Isotropically Radiated Power (EIRP) from the satellite was low. The monopulse autotracking was introduced initially to operate with nonsynchronous satellite and was kept later because it was not practical to maintain a satellite within the beam of a high-gain stationary antenna.

As the amount of total traffic carried by the communication system increased, larger and more sophisticated space repeaters became economical. This meant larger EIRP and better station keeping for the satellite and the possibility of smaller, non-tracking antennas on the ground. Due to existing specifications,[1] these possibilities are not presently utilized in the basic Intelsat network, except for short-term assignments. However, all domestic satellite communications systems presently being built or planned[2,3] are based on antennas in the 50 dB or smaller gain category.

This paper describes the basic requirements, design, and achieved characteristics of such an antenna. The initial design was developed for the Telesat Canada domestic satellite system, which utilizes 8 such antennas. Additional units were used in transportable earth stations for various international telecast applications, such as the coverage of President Nixon's visit to China.

2. Requirements

The intended use of the feed and overall antenna system is in satellite communication earth stations with moderate complexity. The main requirements for such an antenna can be summarized as follows:

a. Frequency bands of 3700-4200 MHz (receive), and 5925-6425 MHz (transmit).

b. Two orthogonal polarizations in the receive and two orthogonal polarizations in the transmit frequency bands. Orthogonal polarizations must be either rotatable linear or circular. Independent adjustability of polarizations for the receive and transmit bands is desirable.

c. A main reflector diameter of 22 to 50 feet; the size and position of the subreflector are determined by the diameter, but the same radiating source is used in all cases.

d. Antenna efficiency of better than 70% for receive and better than 60% for transmit.

e. Antenna noise temperature of less than 40°K at 10° elevation angle.

f. Sidelobes lower than [32-25 log $\theta°$] dB relative to isotropic level, where $\theta°$ is the angle from main beam.*

g. Spectrum re-use‡ isolation better than 30 dB between 1-dB points of the main beam.

h. Antenna mount should permit hour-angle declination or az-el with limited steerability compatible with synchronous satellites.

i. Erection and alignment should require less than 10 days for a 4 man crew.

3. Description of Basic Antenna

The requirements listed in Section 2 above define a 4-port antenna in its fully developed version for spectrum re-use in both the receive and transmit frequency bands. However, initial requirements are mostly for 1 receive and 1 transmit terminal with orthogonal polarizations. Thus, the basic feed was developed for this simpler case, but in such a manner that the expansion capability can be achieved by add-on components without modifying the already installed hardware. At the same time, the components for this expanded operation were developed and tested.

For operational convenience and high G/T versus weight ratio, dual reflector microwave optics with shaped reflector profiles was selected.† The third element in this optics system is the radiating source, which is situated in the vertex region of the main reflector.

The basic geometry and a photograph of the overall antenna system are shown in Figs. 1 and 2. In this configuration, the feed is used with a 33⅓-foot-diameter antenna structure.# The feed was also used in a similar arrangement with a 24-foot-diameter antenna. Fig. 3 shows the block diagram of the basic feed.

---

* The interference characteristics of a communication antenna is defined by the level of its side lobes relative to the level of an isotropic antenna. At 1° from the main beam, the side lobe level must be a maximum of 32 dB above the isotropic; from there it must fall according to the defined logarithmic envelope.

‡ "Spectrum reuse" is an antenna operational mode in which a frequency band is used simultaneously two or more times for independent communications. Spectrum reuse can be based either on orthogonality of polarizations, isolation between independent beams, or on both. Typically, 30-dB isolation is desirable between the independent channels.

† The most important electrical characteristic of an earth station antenna is its gain (G) over noise temperature (T) ratio. The cost effectiveness of antennas can be compared if this G/T ratio is normalized to the weight (cost) of the antenna structure.

Constructed by LTV Electrosystems Division, Garland, Texas.

The operation of the antenna and the function of its main components can be described by following the path of the transmitted signal. For domestic-type earth stations, the transmitter typically has 1-5 kW output power and it is located in a trailer-type shelter on
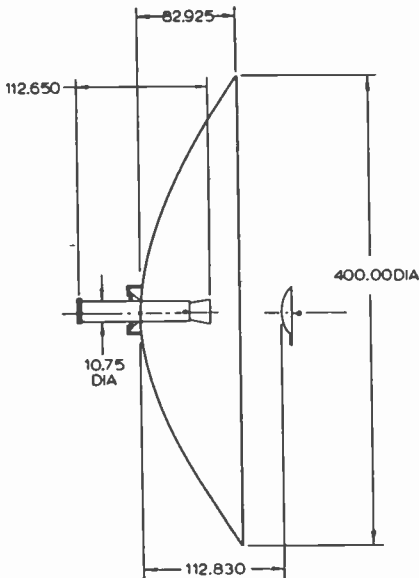

Fig. 1—Geometry of microwave optics for the antenna.

the rear of the antenna. Typically, a 24-foot-long flexible elliptical waveguide is used to connect this transmitter to the input of the feed allowing limited antenna steerability. Typically, ±20° hour-angle* steerability is adequate to choose between an operational and spare satellite. The transmit port of the feed is fixed on the rear panel of the feed housing; inside the housing, the signal goes through a flexible waveguide section to one port of an orthocoupler. The antenna end terminal of the orthocoupler is connected to a noncontacting type of rotary joint.

---

* Assume that one main axis of the antenna mount is parallel to the axis of the earth and the main beam axis of the radiating aperature is integrated with the mount so that it is directed toward the desired point on the synchronous orbit. Under these conditions the described axis of the mount can be called an "hour-angle axis" and rotation around this axis assures that the antenna beam remains directed approximately toward the synchronous orbit for small ± rotations from the North–South plane. For such mounts, the precise tracking of synchronous satellites requires essentially only one degree of freedom, with very small (typically ±0.1°) declination corrections.

This arrangement permits rotation of the orthocoupler by about ± 55°, thus assuring a total of 110° polarization rotation capability of the outgoing wave. If the desired polarization mode of the antenna is linear, then the rotary joint is connected via a straight circular waveguide section to a horn. If the desired polarization mode is circular, then the straight waveguide section is replaced by a differential phase

Fig. 2—Antenna system mounted on an hour-angle declination pedestal.

shifter designed to produce 90° phase shift between a horizontal and vertical incoming wave component. Thus, this unit is capable of producing right or left circular polarization depending on whether the orthocoupler is rotated +45° or −45° relative to its nominal (linearly polarized) position.

If the orthocoupler position is varied by a small angle around its 45° or −45° positions, then an elliptically polarized wave with various ellipticity ratios can be generated, thus allowing the antenna to
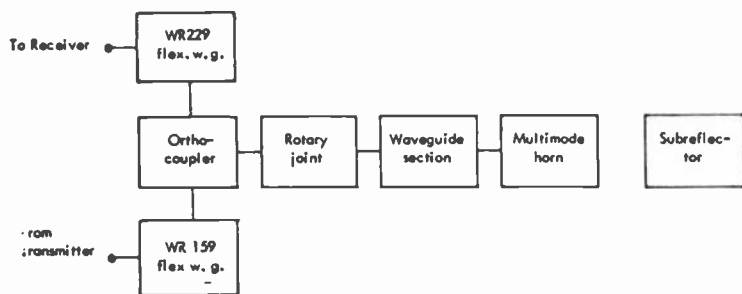
Fig. 3—Block diagram of feed for the basic mode of operation.

synthesize various polarization ellipses as may be required for cancellation of cross-polarized components in spectrum re-use applications. The position of the orthocoupler can be set by a drive from the front panel. In a more versatile version, the orthocoupler and phase shifter can be set independently, and thus virtually any polarization ellipse can be synthesized.

After the transmitted wave reaches the throat of the horn in a TE_{11} mode, mode conversion is employed to obtain an approximately Gaussian axially symmetrical amplitude distribution in the horn aperture. This aperture is then used to illuminate the subreflector, which in turn illuminates the main reflector. The main part of the subreflector is axially symmetrical. However, an asymmetrical flat plate reflector is attached to its perimeter to scatter unwanted wide-angle radiation from the horn into unimportant directions. The main reflector is axially symmetrical and produces a constant phase–amplitude distribution in the main aperture.

For the receive operation, the antenna operates similarly, except that the signal flows in the opposite direction. The received signal is decoupled from the feed circuit by the remaining port of the orthocoupler and, typically, is brought down to the equipment shelter via another elliptical flexible waveguide.

In the above described simple antenna circuit, four elements required special design considerations, namely, the orthocoupler, the phase shifter, the multimode horn, and the microwave optics.

Orthocoupler

The orthocoupler is a 3-waveguide port device, with two equipment terminals and one antenna (common) terminal.[4] All terminals are usable in the 3700-4200 MHz and 5925-6425 MHz frequency bands. The equipment terminals are double ridged rectangular waveguides to allow the 1:1.73 relative bandwidth operation. The antenna terminal is a square waveguide. The better than 26 dB reflection coefficient and better than 40 dB isolation between the equipment terminals in this very wide frequency band are achieved by a series of polarizer plates perpendicular to the input polarization of the straight arm and a double-window type of coupling arrangement for the side arm. A number of tuning screws are used to cancel the junction effect.

The outgoing wavefront from the orthocoupler toward the antenna is essentially perpendicular to the axis of the waveguide except for the straight arm input around 6425 MHz. At this frequency, a small beam squint occurs in the pattern when the orthocoupler is used. Because this squint is so small (causing less than 0.1 dB on axis gain reduction), it was decided to use the presently described (asymmetrical) orthocoupler instead of the more complicated symmetrical type.

Phase Shifter

The phase shifter is an approximately $5\lambda_g$ long circular waveguide section that is loaded in one plane by two symmetrically located series of posts. The number of posts and their penetration was determined experimentally to produce the necessary 90° differential phase shift. Their envelope follows an essentially Gaussian-function shape in order to maintain impedance matching and avoid higher order mode generation. Essentially, this phase shifter has an octave bandwidth, but some fine optimization was necessary to achieve high-quality axial ratio values for the actually used 3700-4200 MHz and 5925-6425 MHz frequency bands. It was found that some degree of independent optimization for the two frequency bands was possible by selecting the total length of the phase shifter and average penetration of the posts to control the phase shift in the receiver frequency band and by choosing the density of posts to control the phase shift in the transmitter frequency band. The axial ratio possible with the phase

shifter under ideal terminating conditions is about 1.2 dB. However, in the actual circuit terminated by the orthocoupler and multimode horn, the peak axial ratio deteriorates to about 1.5 dB due to internal reflections.
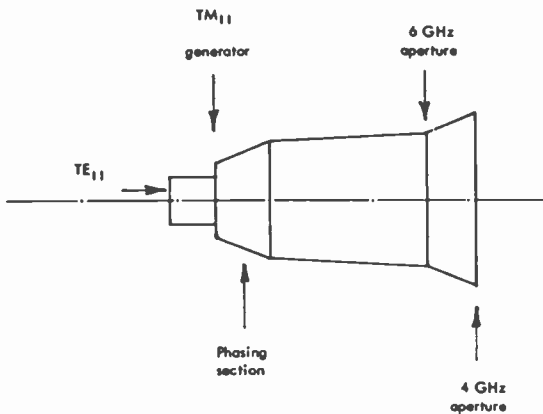
Fig. 4—Generation and phasing of higher-order modes in stepped variable-flare-angle horn.

Multimode Horn

The design of the multimode horn was dictated by the contradicting requirements of axially symmetrical main lobe and low side lobes for the main polarized component, low crosspolarized side lobes, low loss, simple structure for fabrication, and acceptable sensitivity to tolerances. The principle of the horn is shown in Fig. 4. A step in the throat is used as a multimode generator. Depending on the frequency and antenna end diameter of this step, a number of modes can be propagated to the aperture.[5] Depending on the size of the step, the amplitude of these modes relative to the basic mode can be adjusted. As a function of this relative amplitude and relative phase, the combination of these modes with the basic mode can be either useful or harmful insofar as the shape of the radiated pattern is concerned.

Usually the generated higher-order modes carry a cross-polarized component. Thus, the pattern optimization must be carried out not only for the main polarized component, but also for the entire vector field and for a very wide frequency band.

Attempts were made to handle this case analytically, but the author's experience is that even elaborate calculations are adequate only for initial guidance. Thus, much of the detailed design was carried out experimentally. These experiments yielded a compromise step size that did not generate an intolerably large cross-polarized component. The step was followed by a rapidly flaring section to get out fast from the cutoff region of the generated higher order modes. In this manner, it was possible to establish a reasonably frequency-independent phase relationship between the basic mode and higher order modes. This flare section is then followed by a slowly varying flare section. This permitted reaching the required aperture diameter without generating intolerable large quadratic phase error in the aperture.

At the joint of the first and second flare sections, some additional higher order modes are generated, which are used to control the 4 and 6 GHz bands separately and thus to achieve a wider overall bandwidth. Finally, just before the aperture, the flare angle is changed again, mainly for the purpose of widening the pattern of the horn at the high end of the frequency band.

The resultant horn is geometrically simple, easy to fabricate and it is not too sensitive to tolerances.

Microwave Optics

The last important element in the r-f design of the antenna is the set of reflector profiles in the microwave optics. This design was determined by the simultaneous requirement of 70% antenna efficiency and a $[32 - 25 \log \theta°]$dB type of side lobe envelope in a Cassegrainian configuration.

The key to achieving such performance is the axial symmetry and frequency independence of the pattern of the radiating horn. At a given frequency, the horn pattern can be made as perfect as measuring accuracy. For instance, the main beam of the pattern at 4.2 GHz is axially symmetrical down to the 30-dB level within ±1 dB and side lobes are better than 32 dB. For such a case, it appears possible in principle to design an optical system that has 30-dB up taper,* thus a constant amplitude distribution in the main aperture can be pro-

---

* "Up taper" in the microwave optics system represents a redistribution of the power radiated by the primary source in such a way that it increases the power density of the beam radiated by the subreflector in the edge region of the aperture. If the primary source generates a sector beam then the "uptaper" is the power density level difference between the edge and center of the main (reflector) aperture.

duced yielding an antenna for which the aperture illumination efficiency, η_A and spillover efficiency η_s would simultaneously be nearly unity.

Unfortunately, the above case cannot be realized even at the given frequency. The area of the subreflector would be about twice as big as desirable for low blockage but still only about 15λ in radius, which is too small for the necessary very rapid up taper in the edge region. Actually, the width of the primary pattern cannot be maintained absolutely constant with frequency. For instance, if the edge of the subreflector were at $\theta = 24°$ from the axis of the system as it is viewed from the phase center of the horn, then at 3.7 GHz, the previously described 30 dB type of up taper would generate 8 dB higher field at the edge of the main reflector than at its center—a clearly undesirable situation. At the same time, at 6.4 GHz, side lobes from the primary pattern would fall on the main reflector causing gain reduction and high secondary pattern side lobes.

In the actual antenna, $\theta = 14°$ was selected, with a 7 dB up taper for the optical system. A shroud to $\theta_s = 16°$ was attached to the subreflector to take care of the spillover radiation side lobes at 3.7 GHz. The resulting microwave optics produces not only a respectable aperture efficiency, but also the specified wide-angle side-lobe envelope structure, which is quite difficult for a Cassegrainian configuration.

Actually, the side-lobe envelope is considerably better than the $[32 - 25 \log \theta°]$ value for most of the frequency band and angular range. The limiting case is 3.7 GHz around 20° and 96° from the main beam. The 20°-region contains the maximum of the spillover radiation around the subreflector, the 96° region has the maximum of the spillover radiation around the main reflector. This latter value can be further reduced by adding an approximately 2-foot-long cylindrical shroud to the main reflector.

4. Additional Operational Functions

4.1 Spectrum Re-Use with Locked Receive-Transmit Polarizations

The basic mode operation described in Section 3 can be expanded to 3- or 4-port spectrum re-use operation by using the circuit configuration indicated in Fig. 5. In this case, 1 or 2 duplexers can be added to the system. These duplexers can be attached to any equipment terminal of the orthocoupler. The duplexer consists of a Y junction, a 4 GHz band-pass filter and a cutoff section stopping the 4-GHz band but passing the 6-GHz band.

The band-pass filter is built in a double-ridged waveguide and

contains a series of posts. It is designed to have a minimum of 60-dB isolation at 5925 MHz and a maximum loss of 0.06 dB at 4200 MHz. The cutoff section is designed with more than 100 dB attenuation at 4200 MHz and a maximum of 0.04 dB loss at 6 GHz. Once the duplexers are connected to the orthocoupler, the integrated unit has 2 orthogonal 4-GHz ports and 2 orthogonal 6-GHz ports. For the circularly polarized case, the overall assembly can be fixed. However, for the rotatable linear or adaptable circular polarization mode, some rotation of the orthocoupler–duplexer assembly is necessary. This is obtained by a set of 4 flexible waveguide sections attached between the terminals of the duplexer and the input panel of the feed housing.
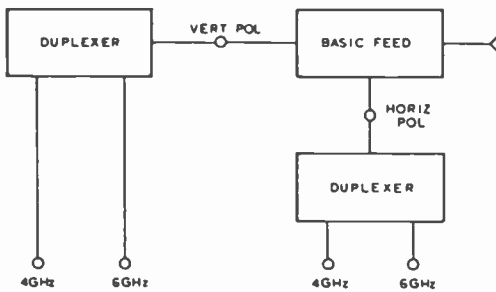
Fig. 5—Block diagram of feed for spectrum re-use mode of operation.

For the spectrum re-use case, the position of the duplexer assembly is remotely controllable, since very precise alignment of the polarization attitude is necessary to utilize the available spectrum re-use isolation. This isolation is generally limited by the characteristics of the incoming signal from the satellite. Alternatively, the isolation available at the satellite is limited by the characteristics of the incoming signal at the input of the satellite.

For high antenna elevation angles, the effect of the propagational medium is negligible; thus for an ideal stable satellite antenna polarization, the earth-station antenna polarization can be set, and orthogonality between the transmit and receive polarization is adequate. The above-described circuit is adequate for most antenna locations.

4.2 Spectrum Re-use with Independently Rotatable Receive–Transmit Polarizations

For earth stations with low elevation angles toward the satellites, the Faraday polarization rotation effects of the propagation medium are

not negligible.[6] Furthermore, the sense of polarization rotation is opposite for the up and down links. Thus, the ideal earth-station antenna must have a capability of rotating the up-link and down-link polarizations independently. Such capability can be added to the feed circuit described in Section 4.1. The block diagram of the required circuit is shown in Fig. 6. Two polarizers make up the dual polarizer
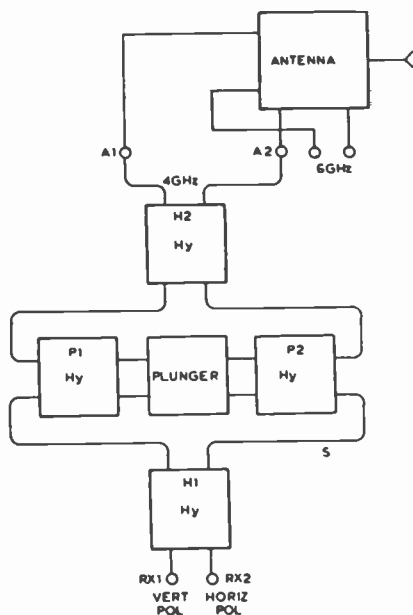
Fig. 6—Block diagram of feed for independently rotatable receive and transmit polarizations.

circuit, one for the 4-GHz band and one for the 6-GHz band. Their layouts are identical. One polarizer consists of 4 short-slot hybrids, 4 identical S-shaped waveguide sections, a plunger assembly; and some connecting waveguide elements.

The H_1 and H_2 short slot hybrids and P_1 and P_2 adjustable phase shifters form an adjustable power divider. The P_1 and P_2 phase shifters are locked together in such a way that the ϕ and $(90 - \phi)$ relationship between their respective phases is maintained for all values of ϕ. Then, for an input signal at Rx_1:

$$A_1 = 0, A_2 = \;\; 1 \;\; \text{if} \;\; \phi = \;\; 45°$$
$$A_1 = A_2 = 0.707 \;\; \text{if} \;\; \phi = \;\; 90°$$
$$A_1 = 1, A_2 = \;\; 0 \;\; \text{if} \;\; \phi = 135°$$

Since A_1 is connected to the "horizontal" and A_2 to the "vertical" input port of the orthocoupler, the output polarization is gradually changed from vertical to horizontal while ϕ is adjusted from $45°$ to $135°$. At the same time, for an input signal at Rx_2, the output polarization is changing from $-45°$ to $+45°$.

Actually, the outputs of H_2 are not connected directly to the input of the orthocoupler since the same orthocoupler must accept the transmit band signals as well. Thus, a pair of duplexers are inserted that combine the two frequency bands.

Physically, the P_1 and P_2 adjustable phase shifters are built up from the same type of short slot hybrids used for H_1 and H_2. They are connected as shown in Fig. 6. There is a double plunger in the middle of the system that is moved by a motor. There is a short straight section for the plungers between the short-slot hybrids, and there are 4 identical electroformed S bends to connect the differential phase shifters with the hybrids H_1 and H_2.

The described 4-hybrid polarizer is for one frequency band; another 4-hybrid polarizer can be provided for the other frequency band. In such a configuration, no flexible waveguides are required in the feed. However, in practice, a single polarizer is adequate to obtain independence between receive and transmit frequency bands if the flexible waveguides are retained. For 30 dB type of spectrum re-use isolation, very high quality short-slot hybrids are required, and the electrical path lengths of the various connecting waveguide elements must be carefully equalized. In the actual circuit, about 26 dB linear axial ratio was measured in the primary pattern in 500-MHz band-width for $\pm5°$ polarization rotation. Such a primary axial ratio results in 32 dB or better polarization isolation in the secondary pattern. It is believed that further improvements are possible by refining the dual polarizer.

5. Some Selected Results

The full description of a spectrum re-use antenna system by experimental data is beyond the scope of the present paper. Instead, a few selected test results are presented. These results were chosen to illustrate the previous discussions and to draw attention to some of the more interesting features.

5.1 Primary Patterns

Fig. 7 shows the main and cross-polarized patterns of the radiating source in the middle of the 4- and 6-GHz frequency bands in the E,

$45°$, and H planes, for linear polarization. Fig. 8 shows the patterns for circular polarization. Note the high degree of axial symmetry, low side lobes, and low cross-polarized side-lobe levels. The exhibited patterns are fairly representative of the overall frequency band as can be concluded from Table 1. This table shows the summary of primary pattern characteristics, such as the gain, G; 3-dB and 10-dB beam widths, θ_3 and θ_{10} respectively; first sidelobe level, κ_1; axial ratio, A; and spectrum re-use isolation I (minimum level difference between main and cross-polarized pattern) within the 1-dB and 3-dB beam-width region of the main lobe.
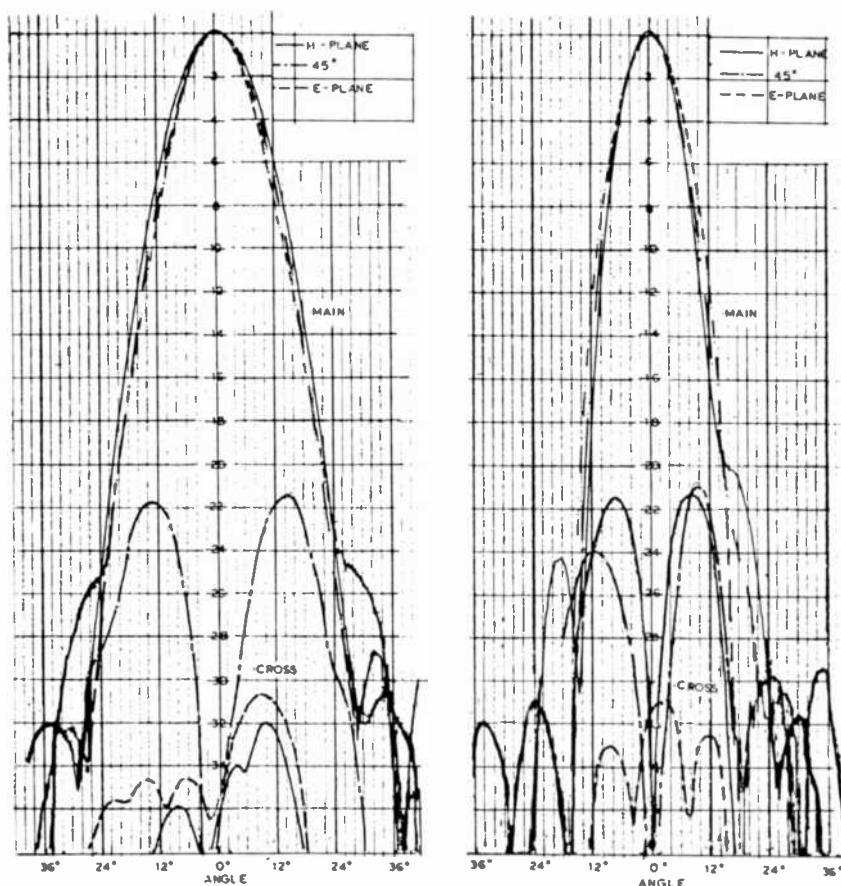
Fig. 7—Main and cross-polarized patterns of the horn for linear polarization (3950 and 6175 MHz frequency bands).

For spectrum re-use applications, the value of A and I_{1dB} has particular significance. The lowest value for A (38dB) determines the ideal spectrum re-use isolation available with this antenna if the angular alignment of the earth station antenna toward the satellite is perfect. A more practical characteristic is I_{1dB}, which stands for the available isolation when the satellite is permitted to drift within the 1-dB beam width of the antenna. This value is $\pm 0.08°$ at 6425 MHz. For such a case, the worst level of I_{1dB} is only 23 dB in the primary pattern. However, an analysis of the cross-polarized primary patterns shown in Fig. 7 indicates that I is always much better in the secondary pattern than in the primary radiation. For the cross-polarized component the spillover efficiency,
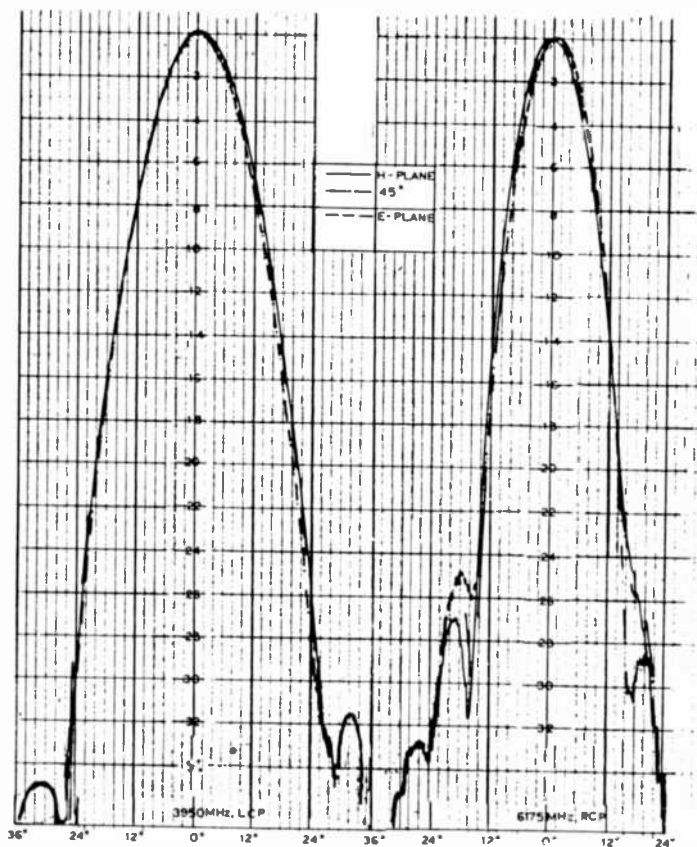
Fig. 8—Patterns of horn for circular polarization.

Table 1—Summary of Primary Pattern Characteristics

f(MHz)	3700						
Plane Pol. att. Pol. mode	Vertical		AZIMUTH 45°		Horizontal		LCP
	Main	Cross	Main	Cross	Main	Cross	Main
G(dB)	21.78						
$\theta_3°$	17		15.5		3.5		15.5
$\theta_{10}°$	31.5		28		26		28
κ_1(dB)	33	33	30	18.8	23	33	30
A(dB)	43		43		43		
I_{1dB}(dB)	36		32		36		
I_{3dB}(dB)	34		22.5		34		

f(MHz)	3950						
Plane Pol. att. Pol. mode	Vertical		AZIMUTH 45°		Horizontal		LCP
	Main	Cross	Main	Cross	Main	Cross	Main
G(dB)	21.60						
$\theta_3°$	17		15		14		15.5
$\theta_{10}°$	30.5		28		27		28.5
κ_1(dB)	29	32	25	21	29	31	32
A(dB)	45		45		45		
I_{1dB}(dB)	32		31		32		
I_{3dB}(dB)	30.5		24.5		31.5		

f(MHz)	4200						
Plane Pol. att. Pol. mode	Vertical		AZIMUTH 45°		Horizontal		LCP
	Main	Cross	Main	Cross	Main	Cross	Main
G(dB)	21.98						
$\theta_3°$	16		15		13.5		13.5
$\theta_{10}°$	29		27.5		26		27.5
κ_1(dB)	32	34	32	24.5	32	34	34
A(dB)	41		41		41		
I_{1dB}(dB)	34		33		34		
I_{3dB}(dB)	33.5		26.5		33.5		

Table 1—Continued

f (MHz)	5925						
Plane Pol. att. Pol. mode	Vertical Main	Cross	AZIMUTH 45° Main	Cross	Horizontal Main	Cross	RCP Main
G (dB)	24.53						
$\theta_3°$	12		12		12		12
$\theta_{10}°$	20		24		22		22
κ_1 (dB)	26.5	33	31	19	24	30	29
A (dB)	45		45		45		
I_{1dB} (dB)	36		34		36		
I_{3dB} (dB)	35		23		35		

f (MHz)	6175						
Plane Pol. att. Pol. mode	Vertical Main	Cross	AZIMUTH 45° Main	Cross	Horizontal Main	Cross	RCP Main
G (dB)	25.80						
$\theta_3°$	10		12		10		11
$\theta_{10}°$	18		22		20		20
κ_1 (dB)	20	21	30	20	30	32	25
A (dB)	54		54		54		
I_{1dB} (dB)	24		24		29		
I_{3dB} (dB)	22		22		30		

f (MHz)	6425						
Plane Pol. att. Pol. mode	Vertical Main	Cross	AZIMUTH 45° Main	Cross	Horizontal Main	Cross	RCP Main
G (dB)	25.80						
$\theta_3°$	10		12.5		10.5		10
$\theta_{10}°$	18		19.5		19		18
κ_1 (dB)	17	19.8	24.5	23	27	25	20
A (dB)	38		38		38		
I_{1dB} (dB)	23		25.2		27		
I_{3dB} (dB)	21		25		26		

η_s, is typically 3 dB worse than for the main polarized component because, for this component, at least half the power is lost in spillover radiation. At the same time, the aperture distribution efficiency, η_A, is typically 3 dB worse than for the main polarized component because about half of the aperture is not utilized for this component. Thus, at least 6 dB improvement is predicted from this simple model. Actually, at no frequency was observed improvement less than 8 dB. Thus, the indicated type of primary patterns make it possible to achieve 30 dB or better spectrum re-use isolation values.

5.2 Circular Polarization Axial Ratio

Fig. 9 shows the circular polarization axial ratio of the radiating source measured along the axis of its main beam for all four input feed ports as a function of frequency. The recordings were taken with a slowly sweeping generator and with a relatively rapidly rotating transmit probe. Since the pattern of the radiating source is essentially axially symmetrical, and virtually no depolarization takes place in a Cassegrainian antenna, a similar axial ratio will be available in the whole main aperture plane and within the 3-dB beam width of the secondary main beam.

The production antennas exhibited typically a maximum of 1.5 dB primary axial ratio, which corresponds to about 21 dB cross-polarized level on the axis of the antenna. Again, this cross-polarized pattern is modified by the optics of the antenna, and within the 1-dB beam width of the main beam of the secondary pattern, a certain amount of improvement takes place. This is discussed in connection with the secondary-pattern characteristics.

5.3 Independent Rotation of Receive and Transmit Polarizations

The basic circuit described in Section 4.2 requires two polarizers, which introduce about equal losses in the 4- and 6-GHz circuits. The 4-GHz loss can be reduced by a slight variant of this circuit. In such a case, the coarse polarization adjustment is achieved by the standard rotatable polarizer unit of the feed and only one additional polarizer circuit is used in the 6-GHz band to provide a differential polarization rotation relative to the 4-GHz band. For such a case, the polarizer must cover only the range of differential Faraday rotation, of the order of $\pm5°$. Test results for such a requirement indicate that 25-30 dB polarization isolation in the primary pattern can be achieved for small polarization angle adjustments. Fig. 10 shows the
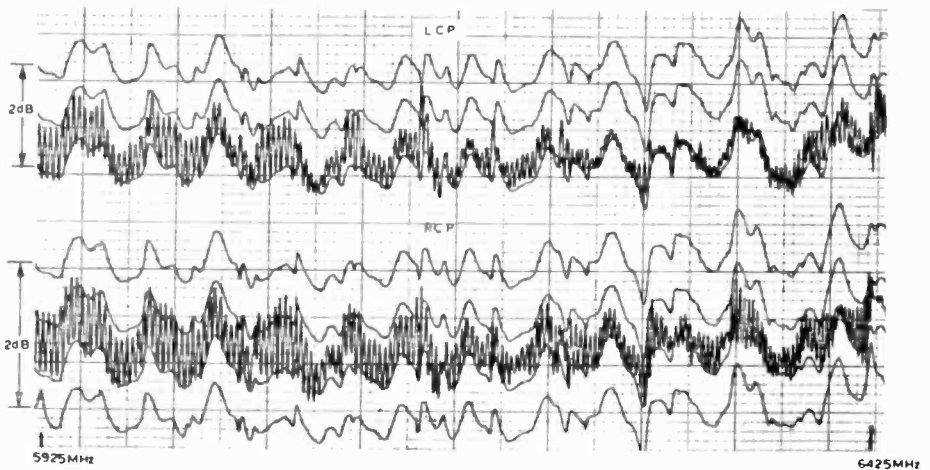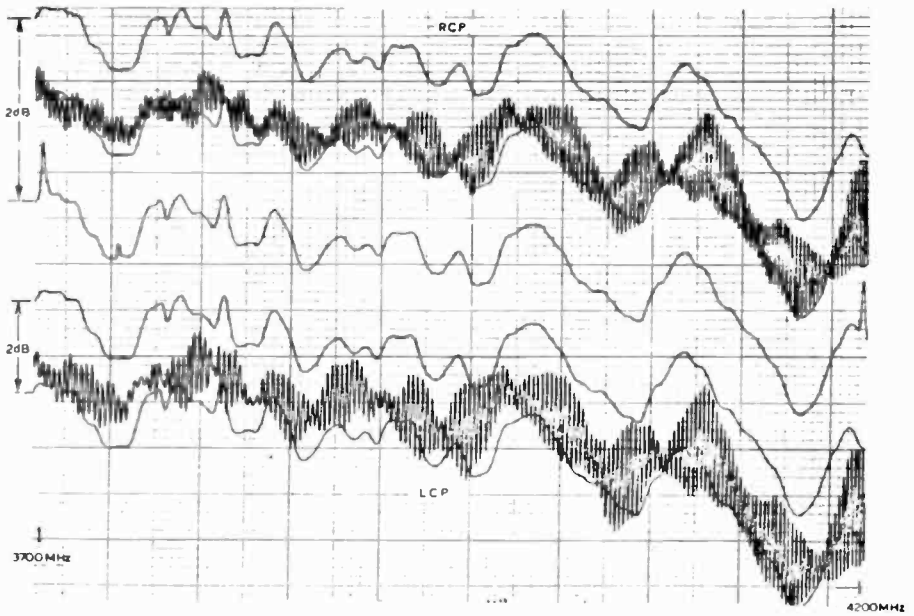
Fig. 9—Right- and left-circular-polarization axial ratio measured in the primary pattern for the spectrum re-use mode for the 4 and 6 Ghz frequency bands (axial ratio is the envelope of the curve recorded with rotating probe; calibration lines are 2 dB apart).

measured polarization isolation with such a circuit over a 500-MHz band for various amounts of polarization angle adjustments.

The polarization angle adjustment can be achieved in two steps.

(a) By the described rotatable orthocoupler, the polarization can be set within $\psi = \pm 55°$ with a minimum of 30 dB isolation and a maximum of at least 35 dB isolation. This adjustment may be called the coarse adjustment, and can provide the proper polar-
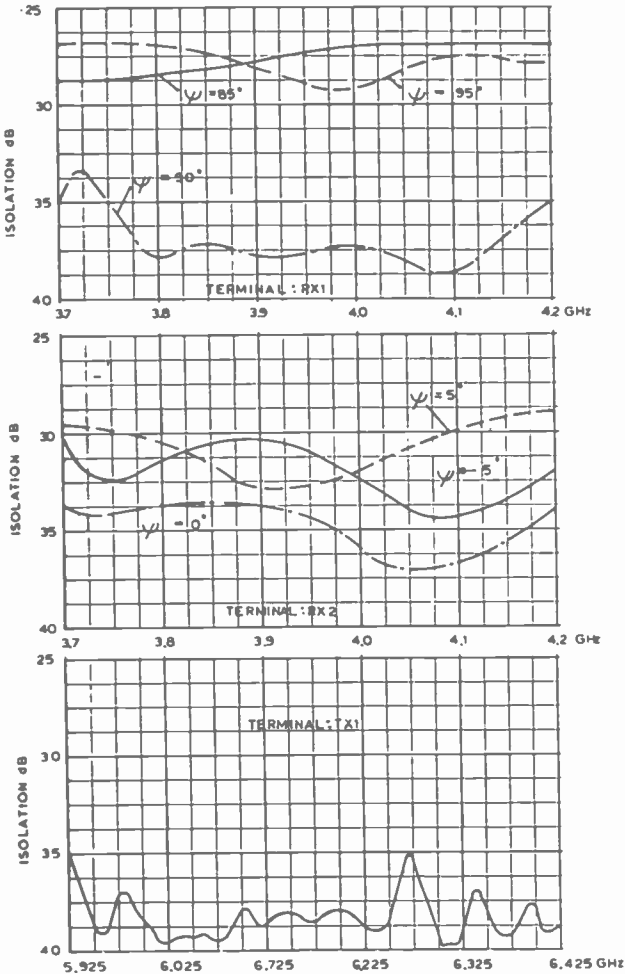
Fig. 10—Measured spectrum re-use isolation on axis of primary pattern versus frequency for independently rotatable receive and transmit polarization (transmit polarization fixed at $\psi = 0°$ and 90°).

ization for corresponding to a given satellite and a given site. Once the rotatable polarizer is set, the nominal polarizations corresponding to the various terminals will be the following:

Rx_1	ψ_1
Rx_2	$\psi_1 + 90°$
Tx_1	$\psi_1 + 90°$
Tx_2	ψ_1

(b) Using the plunger of at least one polarizer operating say in the Rx band, the polarization can be set within $\tau = \pm 5°$ with a minimum of 25 dB and a maximum of at least 30 dB isolation in the vicinity of ψ_1. This adjustment may be called the fine, or differential, polarization angle adjustment since it affects only one frequency band; thus it is able to generate a differential polarization angle relative to the other band. With the application of a dual polarizer, a total of $\pm 10°$ differential polarization angle can be generated between the receive and transmit bands.

Fig. 11 shows the achievable isolation for the circularly polarized case. The incoming signal simulating the one emitted by the satellite was intentionally set to 1.5 dB axial ratio. Under these conditions, by the use of the adjustable plunger and by the rotation of the orthogonal coupler and fixed 90° phase-shifter assembly of the feed, the resultant 23.5 dB cross-polarized level was measured over the 500 MHz frequency band as shown by the figure. Obviously this achievable isolation may be much better when the axial ratio of the incoming signal from the satellite is better.

5.4 Effect of Antenna Panel Misalignment

Domestic satellite communication systems eventually will use hundreds of 50 dB-gain type antennas. These antennas will be assembled on limited-steerability mounts, and due to economical limitations, most of these sites will not have pattern or gain-measuring facilities. Thus, it is of interest to determine how sensitive such antenna systems will be to erection tolerances, and how reproducible the results will be.

During the development and early use of the described antenna, two interesting observations were made that throw some light on these problems. Two prototype tests of this antenna were made. Before the first test, the antenna panels were aligned while the re-

flector was lying on the ground. The usual optical target alignment method was used and an estimated maximum 0.015-inch rms deviation between these targets and the ideal optical surface were achieved.
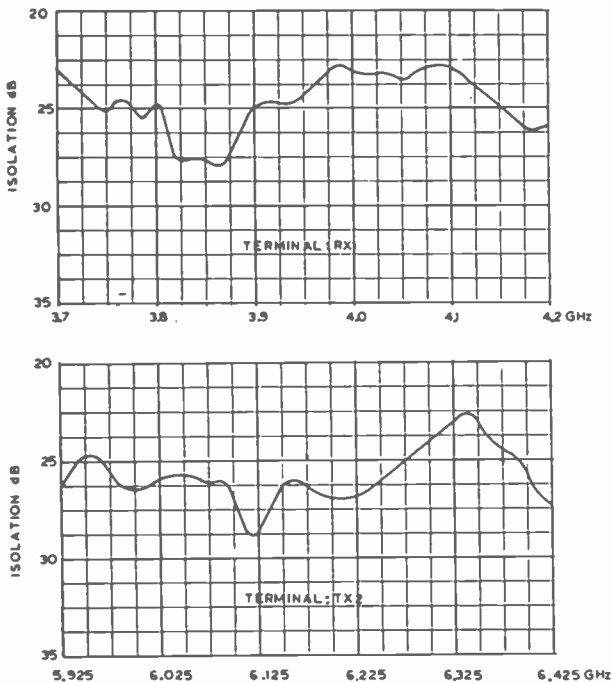
Fig. 11—Measured spectrum re-use isolation on axis of primary pattern versus frequency for circular polarization (incoming wave axial ratio is better than 1.5 dB).

The gaps between the 12 surface panels of the antenna were set to about 1/16 of an inch or better. During the hoisting of the reflector to its test turntable 70 feet above ground, an accident in the crane foundation caused the reflector to drop a few feet in midair and the antenna experienced larger than normal accelerations. This and some other factors caused the panels to shift, and a few gaps between panels more than ¼ of an inch were observed.

Since the shift was estimated to cause only about 0.06-0.08-inch rms surface errors, it was decided to test the antenna electrically and try to minimize the aperture phase errors by a repositioning of the subreflector.

Fig. 12a shows the field contour lines in the vicinity of the main

beam for this condition. This plot was assembled from 39 closely spaced horizontal pattern cuts, separated by 0.1° elevation-angle increments. Although the main plane patterns of the antenna were not catastrophically bad, the mapping revealed that in one of the 45° planes, a side lobe as bad as 6.2 dB existed. The antenna gain was more than 1.5 dB below nominal. After this test, the antenna backframe in the edge region was reinforced and the panels were realigned while the antenna was on the test table. After final panel setting, the optical targets represented a better than 0.010-inch rms deviation from the specified reflector surface. Fig. 11b shows the field contours in the vicinity of main beam after this alignment. The experiment shows the necessity of utmost care in the handling of this type of antenna.

The second observation was more on the cheerful side. During the prototype tests, the y factor of the antenna with the sun was recorded carefully for the purpose of relative gain measurements, since for most operational sites, this is the only readily available boresight source. After this test, the panel-aligning screws and nuts were taped together and the antenna was disassembled and shipped to a location near Shanghai. The erection required 5 days, after which the antenna was ready for test. Again, using the Sun as a boresight, the previously recorded y factors and antenna-gain values were reproduced within 0.25 dB without touching the axial position of the subreflector.

5.5 Secondary-Pattern Characteristics

The secondary patterns of the antenna were measured at a site in Greenville, Texas. The antenna was placed on a test tower, keeping the elevation axis 92 feet above ground level. The boresight antenna 4000 feet distant was a 6-foot-diameter periscope antenna, appearing 0.9° above the local horizon from the main antenna. Due to the relatively large height of both the main antenna and boresight antenna positions, the center of the first Fresnel zone on the ground was 4.4° below the line connecting the centers of the main and boresight antennas. This condition assured that ground reflections had very little influence on any of the pattern and gain measurements in the vicinity of the main lobe. The site was clear except in one azimuth direction (about 81° from boresight) where another nearby test tower gave strong reflections.

The main and cross-polarized patterns for linear and circular polarizations in the horizontal and elevation planes were recorded in great detail. Figs. 13 and 14 show typical patterns for 3950 MHz and 6175 MHz.

Tables 2 and 3 show the summary of the antenna characteristics extracted from the pattern, gain, and noise-temperature measurements. In these tables, $f(\phi)$ is the level of the monotonicaly decreasing pattern envelope below the level of main lobe maximum at the angle ϕ from the axis of main beam. $T_{Ant}(\theta)$ is the antenna noise temperature at an antenna main beam elevation angle θ, T_{Rx} is the noise temperature of the receiver system referred to the receive output port of the feed.

Several interesting conclusions can be drawn from Figs. 13 and 14 and Tables 2 and 3.

1. It is possible to achieve a high antenna efficiency in a 1:1.73 relative bandwidth.

$\theta_{3dB} = 461°$ $\theta_{10dB} = 1.000°$ $\theta_{16dB} = 1.445°$
HORIZ POL f=3950MHz

$\theta_{3dB} = 450°$ $\theta_{10dB} = .795°$ $\theta_{16dB} = .900°$
HORIZ POL f=3950MHz
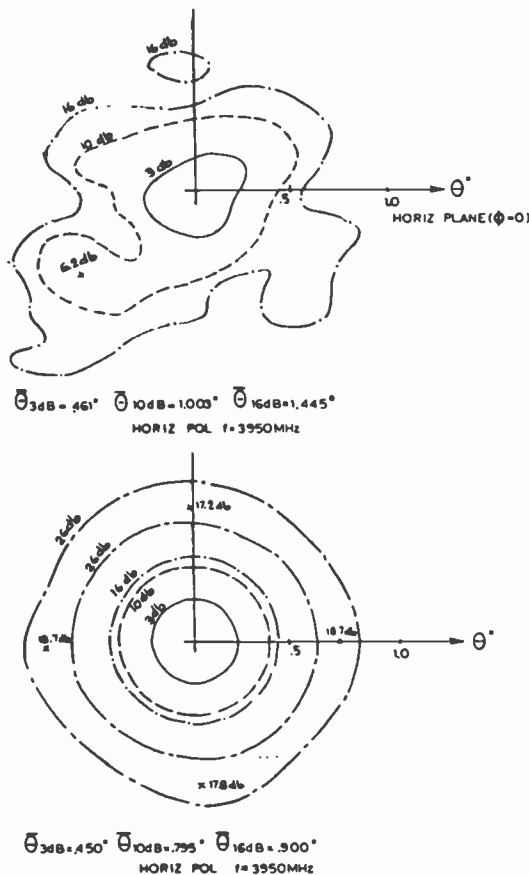
Fig. 12—Field contour lines in vicinity of main beam with (top) mis-aligned and (bottom) aligned reflector.
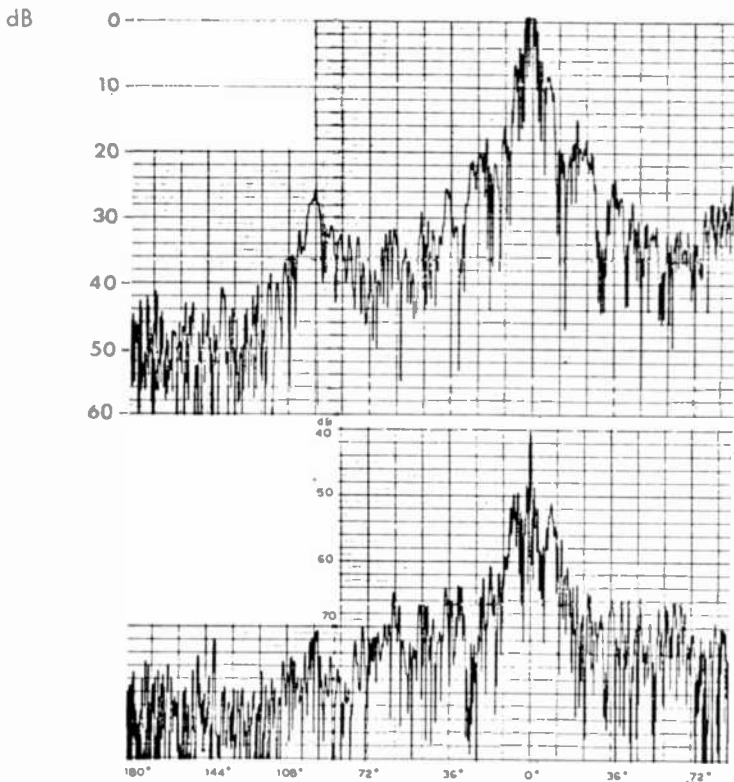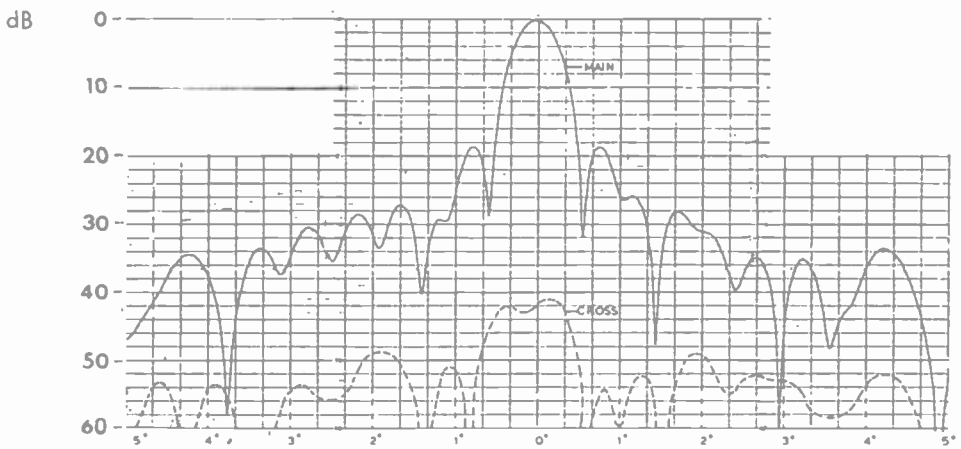
Fig. 13—Main and cross-polarized patterns of the antenna system (3950 MHz), linear polarization.
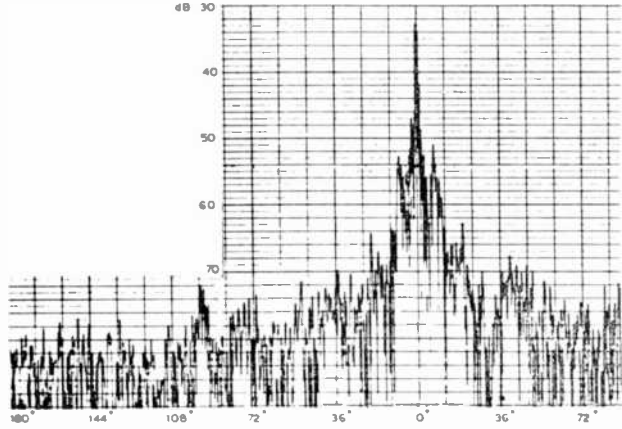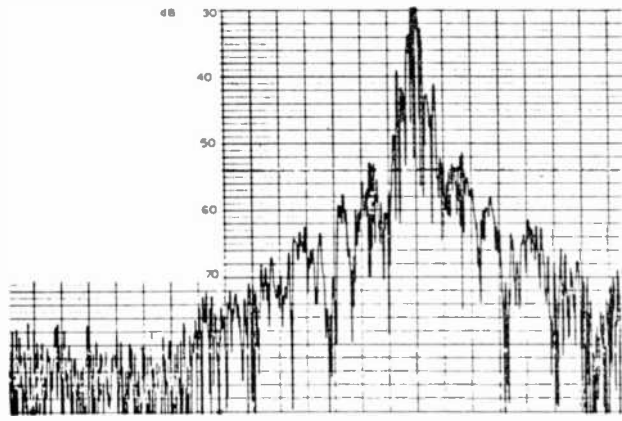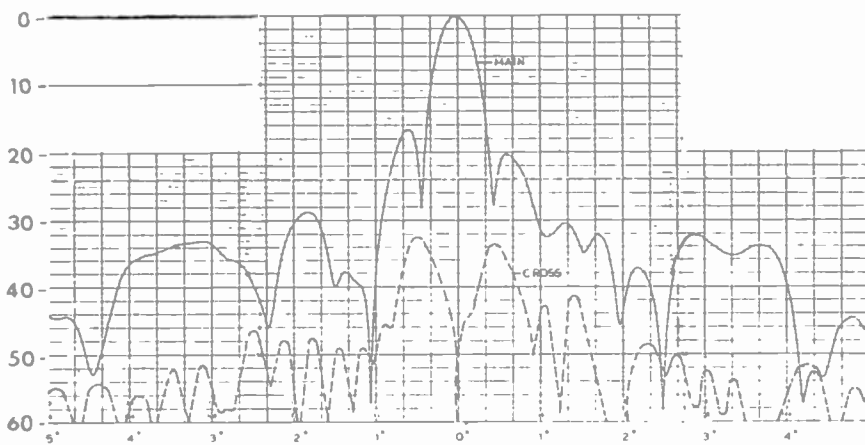
Fig. 14—Main and cross-polarized patterns of the antenna (6175 MHz), linear polarization.

Table 2—Summary of Antenna Characteristics—Receiver Band

f (MHz)	3700						3950						4200					
Plane / Pol. att. / Pol. mode	Azimuth Vertical Main	Vertical Cross	Horizontal Main	Horizontal Cross	Elevation Vert. Main	Hor. Main	Azimuth Vertical Main	Vertical Cross	Horizontal Main	Horizontal Cross	Elevation Vert. Main	Hor. Main	Azimuth Vertical Main	Vertical Cross	Horizontal Main	Horizontal Cross	Elevation Vert. Main	Hor. Main
G (dB)	50.22						50.92						51.65					
θ_1°	.49	—	.50	—	.50	.46	.45	—	.45	—	.46	.45	.45	—	.45	—	.45	.42
η_1°	.82	—	.86	—	.78		.78	—	.89	—	.79	.79	.79	—	.79	—	.77	.75
κ_1 (dB)	16	32.8	16.5	42	17.5	17	16.8	18.7	18.7	42	18.2	17.2	17.3	37.5	17.3	37.5	17.5	17.2
A (dB)		50		42				44		42				37.5		37.5		
I_{mn} (dB)		36						42		40				35.5		37.5		
I_{sm} (dB)		31						40		38				32.5				
$f(15°)$ (dB)	35	52	44	51	40	39	39	49	42	49	39	39	35	48	35	56	40	38
$f(12°)$ (dB)	48	61	46	60	39	45	46	57.5	46	50	42	44.5	50	61	49	65	44.5	46
$f(24°)$ (dB)	49	62	52	60	44	45	50	63	49	54	45	46	54	66	52	66	49.5	45.5
$f(36°)$ (dB)	57	63	56	64	49	52	55.5	66.5	64	54	55	51.8	56	70	58	67	56.5	49
$f(48°)$ (dB)	57	63	57	65	54	56	56	66.5	64	55	57	59.8	58	70	59	69	58	51
$f(60°)$ (dB)	59	65	57	67	58	56	56	66.5	67.5	55	59	60.2	58	70	59	70	64.5	61
$f(72°)$ (dB)	59	70	57	67	58	56	56	71	67.5	70	59.5	60.2	58	70	59	70	65	61
$f(84°)$ (dB)	59	70	57	67	61	56	56	71	67.5	71	60	60.2	58	70	59	70	65	62
$f(96°)$ (dB)	59	70	59	71			56	74	67.5	71			58	72	59	70		
$f(108°)$ (dB)	66	70	67	71			66	74	71	72			67	73	70	73		
$f(120°)$ (dB)	68	70	67	73			70	74	71	72			70	73	70	73		
$f(180°)$ (dB)	70	74	72	73			72	74	71	77			72	76	76	74		
$T_{ant}(10°)$ (°K)					41	36					37	32					35	32
$T_{ant}(20°)$ (°K)					27.5	26					23	20					25	23
$T_{ant}(45°)$ (°K)					18	22					16	15					18	16
$T_{sys}(10°)$ (°K)					141	136					137	132					135	132
$(T_{sys}=100°K)$ (dB)					21.50	21.33					21.37	21.20					21.30	21.20
$G/T(10°)$ (dB)					28.72	28.89					29.55	29.72					30.35	30.65
I_{mn} (dB)	29						38						38					
I_{sm} (dB)	29.6						30						30					

Table 3—Summary of Antenna Characteristics—Transmitter Band

f(MHz) = 5925

Plane Pol. att. Pol. mode	Azimuth Vertical Main	Azimuth Vertical Cross	Azimuth Horizontal Main	Azimuth Horizontal Cross	Elevation Vert. Main	Elevation Hor. Main
G(dB)	54.75					
θ_s°	.31		.32		.32	.32
θ_m°	.58		.56		.60	.60
r_1(dB)	17.8	35	15.2	32.5	16.0	18.0
A(dB)		39		34.5		
I_{sep}(dB)	36		32.5			
I_{mn}(dB)	34		30.5			
f(6°)(dB)	43	48	41	58	43	45
f(12°)(dB)	53	63	53	65	48	48
f(24°)(dB)	56	63	53.5	66	50	50.5
f(36°)(dB)	60	68	60	66	60	59
f(48°)(dB)	62.5	71…	60	66	62	64
f(60°)(dB)	64.5	71	60	71	65	68
f(72°)(dB)	66	71	64	73	69	70
f(84°)(dB)	68.5	71	73	75		74
f(96°)(dB)	68.5	71	73	75		
f(108°)(dB)	74	74	74	75		
f(120°)(dB)	74	74	74	75		
f(180°)(dB)	78	77	75	77		
I_{sep}(dB)	32					
I_{mn}(dB)	24.5					

f(MHz) = 6175

Plane Pol. att. Pol. mode	Azimuth Vertical Main	Azimuth Vertical Cross	Azimuth Horizontal Main	Azimuth Horizontal Cross	Elevation Vert. Main	Elevation Hor. Main
G(dB)	54.75					
θ_s°	.35		.30		.30	.35
θ_m°	.60		.51		.53	.60
r_1(dB)	16.8	32.5	15.2	49.5	15.8	20
A(dB)		60		60		
I_{sep}(dB)	43.2					
I_{mn}(dB)	37					
f(6°)(dB)	44	55	43	57	44	42
f(12°)(dB)	53	64	54	64	49	49
f(24°)(dB)	56	70	55.5	68	52.5	54
f(36°)(dB)	62.5	70	58	68	56	63
f(48°)(dB)	62.5	71	61	75	66	63
f(60°)(dB)	67	72	61	75	66	66
f(72°)(dB)	71	72	61	75	68	73
f(84°)(dB)	72	72	62	75		74
f(96°)(dB)	76	72	75	75		
f(108°)(dB)	77	77	75	77		
f(120°)(dB)	77	77	75	77		
f(180°)(dB)	78	82	80	80		
I_{sep}(dB)	30					
I_{mn}(dB)	24.5					

f(MHz) = 6425

Plane Pol. att. Pol. mode	Azimuth Vertical Main	Azimuth Vertical Cross	Azimuth Horizontal Main	Azimuth Horizontal Cross	Elevation Vert. Main	Elevation Hor. Main
G(dB)	54.75					
θ_s°	.31		.33		.32	.31
θ_m°	.59		.54		.57	.59
r_1(dB)	19	33.5	16.6	30	18	18
A(dB)		42		47		
I_{sep}(dB)	37		33			
I_{mn}(dB)	33		30			
f(6°)(dB)	43	53	- 42	54	42	43
f(12°)(dB)	51	58	51	64	47	45
f(24°)(dB)	54	63	54	67	52	48
f(36°)(dB)	60.5	71	60.5	70	58	68
f(48°)(dB)	60.5	71	60.5	71	64	65
f(60°)(dB)	60.5	71	60.5	71	64	65
f(72°)(dB)	60.5	71	60.5	72	64	65
f(84°)(dB)	61	71	61	72		71
f(96°)(dB)	73	71	73	72		71
f(108°)(dB)	73	75	73	75		
f(120°)(dB)	73	75	73			
f(180°)(dB)	80	79	80	80		
I_{sep}(dB)	30					
I_{mn}(dB)	29					

2. The side-lobe envelope falls below the isotropic level at about 24° from the main lobe for the main polarized component, and at about 5° for the cross-polarized component. In the rear hemisphere, the antenna side lobes are about 20 dB below isotropic level.

3. The spectrum re-use isolation, I_{1dB}, is at least 36 dB for the 4-GHz band and 32.5 dB for the 6-GHz band for linear polarization. For circular polarization, spectrum re-use isolation of at least $I_{1dB} = 29$ dB was achieved, for a given (nonperfect) incoming polarization. Actually, at the 3 frequencies (5925, 6175, 6425 MHz) indicated in Table 3, the axial ratio of the incoming wave was 0.8 dB, 0.7 dB and 0.8 dB, respectively. For this condition, it was possible to set the ellipticity of the feed so that I_{1dB} was 32 dB, 30 dB, and 30 dB, respectively. It may be mentioned that for a given frequency, better polarization matching, and thus polarization isolation, is possible. However, in a wide frequency band, the polarization ellipse of the incoming wave usually varies, and then only the nonvarying component of polarization ellipse can be matched by the available antenna circuit.

5.6 Antenna Noise Temperature

The noise temperature of an antenna generally can be improved by reducing its internal circuit loss and increasing its spillover efficiency. For a Cassegrainian antenna at low elevation angles, an increase of antenna noise temperature is expected with decreasing antenna size, because high spillover efficiency can be maintained only at the expense of increasing blockage; with decreasing antenna size, the side lobes in the vicinity of the main lobe gradually fall more and more on the ground at low elevation angles. On the other hand, decreasing antenna size makes it possible to eliminate the monopulse tracking circuit and its associated noise temperature contribution.

The measured values of antenna noise temperature, shown in Fig. 15, tend to prove the above considerations. Total antenna noise temperature is approximately 15°K in zenith and 45°K at 5° elevation angle. Since the internal noise temperature of the feed is about 4°K and the atmospheric contribution is about 3° and 27°K in zenith and 5° elevation angles, respectively, the noise temperature contribution of the ground via spillover and scatter comes to 8°K and 14°K for the zenith and 5° elevation-angle positions, respectively. These latter values are only slightly larger than customary for 100-foot-diameter antennas in this frequency band.

5.7 Gain/Temperature Tests with Cassiopeia A and Sun

The ultimate test of any earth station antenna is its system gain/temperature (G/T) ratio measured with a celestial source. The present system uses an uncooled parametric amplifier with a noise temperature of the order of $100°K$. Under these conditions, the system noise temperature can be measured adequately only by the strongest of the celestial sources.

Two celestial sources were selected for this measuring program: Cassiopeia A because of its accurately known flux and the sun because it is within the steerability range for antennas directed toward a synchronous satellite. Since no adequately accurate sun flux data was found in the literature for the 3.7-4.2 GHz frequency band and for the period of the measurements, an accurate calibration of the sun flux was obtained against Cassiopeia A.

Star y factors* were recorded with both stars for various elevation angles, polarizations and frequencies for several days. Then the sun flux (ϕ_{sun}) was determined on the basis that the average gain values obtained from the two independent y factor measurements agree. These calculations resulted in $\phi_{sun} = 0.9162 \times 10^{-20}$ W/Hzm^2 $\pm$ 0.20 dB at 3950 MHz.

Tables 4 and 5 exhibit the relationship between the star y factor, $y = (P_{syst} + P_{star})/P_{star}$ where P_{syst} and P_{star} are the system and star-caused noise power respectively, and system G/T for various antenna elevation angles and frequencies and for Cassiopeia A and the sun for January 1972. The Cass. A flux values were taken from the document published by Intelsat.[7] Since the flux values for both of these stars vary with time, some additional correction is necessary to use these tables in the future. For Cassiopeia A, the T_{star} flux is decreasing monotonically with time, approximately 1.1% per year. For the sun, T_{star} is a periodic function of time over the solar cycle as shown in Fig. 16.

The G/T ratio of the overall system with the given receiver noise temperature is of the order of 30 dB. For such conditions, $y \approx 0.6$ dB for Cass. A and $y \approx 21$ dB for sun. In spite of original doubts, the low value of y for Cass. A did not present any serious limitation on the achievable G/T measuring accuracy.

y-factor readouts were reproducible from day to day within ± 0.03

---

* "Star y factor" is defined as the noise power ratio received by the antenna when it is directed toward a star radiating radio frequency power (flux) relative to the noise power the antenna produces when it is directed toward a "low noise" portion of the sky.

Table 4—Conversion Table to Calculate System G/T from y Factor Obtained by Cassiopeia A (28 <D ft <40, 1972)

G/T (db)

γcorr (db)	.20	.25	.30	.35	.40	.45	.50	.55	.60	.62	.64	.66	.68	.70	.72	.74	.76	.78	.80	f MHz
5	24.56	25.54	26.40	27.06	27.60	28.31	28.69	29.13	29.53	29.68	29.83	29.98	30.12	30.25	30.38	30.51	30.64	30.76	30.88	3700
10	24.39	25.37	26.23	26.99	27.49	28.04	28.52	28.96	29.36	29.51	29.66	29.81	29.95	30.08	30.21	30.34	30.47	30.59	30.71	
20	24.30	25.28	26.14	26.90	27.40	27.95	28.43	28.87	29.27	29.42	29.57	29.72	29.86	29.99	30.12	30.25	30.38	30.50	30.62	
30	24.27	25.25	26.11	26.87	27.37	27.92	28.40	28.84	29.24	29.39	29.54	29.69	29.83	29.96	30.09	30.22	30.35	30.47	30.59	
60	24.24	25.22	26.08	26.83	27.34	27.92	28.37	28.81	29.21	29.34	29.51	29.64	29.80	29.93	30.06	30.19	30.32	30.43	30.56	
5	24.86	25.84	26.70	27.36	27.96	28.51	28.99	29.43	29.83	29.98	30.13	30.28	30.42	30.55						3800
10	24.69	25.67	26.53	27.29	27.79	28.34	28.82	29.26	29.66	29.81	29.96	30.11	30.25	30.38						
20	24.60	25.58	26.44	27.20	27.70	28.25	28.73	29.17	29.57	29.72	29.87	30.02	30.16	30.29						
30	24.57	25.55	26.41	27.17	27.67	28.22	28.70	29.14	29.54	29.69	29.84	29.99	30.13	30.26						
60	24.54	25.52	26.38	27.14	27.64	28.19	28.67	29.11	29.51	29.66	29.81	29.96	30.10	30.23						
5	25.12	26.10	26.96	27.62	28.22	28.77	29.25	29.69	30.09	30.24	30.39	30.54	30.68	30.81						3900
10	24.95	25.93	26.79	27.55	28.05	28.60	29.08	29.52	29.92	30.07	30.22	30.37	30.51	30.64						
20	24.86	25.84	26.70	27.46	27.95	28.51	28.99	29.43	29.83	29.98	30.13	30.28	30.42	30.55						
30	24.83	25.81	26.67	27.43	27.93	28.48	28.96	29.40	29.80	29.95	30.10	30.25	30.39	30.52						
60	24.80	25.78	26.64	27.40	27.90	28.45	28.93	29.37	29.77	29.92	30.07	30.22	30.36	30.49						
5	25.22	26.20	27.06	27.72	28.32	28.87	29.35	29.79	30.19	30.34	30.49	30.64	30.78	30.91	31.04	31.17	31.30	31.42	31.54	3950
10	25.05	26.03	26.89	27.55	28.15	28.70	29.18	29.62	30.02	30.17	30.32	30.47	30.61	30.74	30.87	31.00	31.13	31.25	31.37	
20	24.96	25.94	26.80	27.46	28.06	28.61	29.09	29.53	29.93	30.08	30.23	30.38	30.52	30.65	30.78	30.91	31.04	31.16	31.28	
30	24.93	25.91	26.77	27.43	28.03	28.58	29.06	29.50	29.90	30.05	30.20	30.35	30.49	30.62	30.75	30.88	31.01	31.13	31.25	
60	24.90	25.88	26.74	27.40	28.00	28.55	29.03	29.47	29.87	30.02	30.17	30.32	30.46	30.59	30.72	30.85	30.98	31.10	31.22	
5	25.33	26.31	27.17	27.83	28.43	28.98	29.46	29.90	30.30	30.45	30.60	30.75	30.89	31.02						4000
10	25.16	26.14	27.00	27.66	28.26	28.81	29.29	29.73	30.13	30.28	30.43	30.58	30.72	30.85						
20	25.06	26.04	26.90	27.56	28.16	28.71	29.19	29.63	30.03	30.18	30.33	30.48	30.62	30.75						
30	25.03	26.01	26.87	27.53	28.13	28.68	29.16	29.60	30.00	30.15	30.30	30.45	30.59	30.72						
60	25.00	25.98	26.84	27.50	28.10	28.65	29.13	29.57	29.97	30.12	30.27	30.42	30.56	30.69						
5	25.59	26.50	27.36	28.02	28.62	29.18	29.65	30.09	30.49	30.64	30.79	30.94	31.08	31.21						4100
10	25.35	26.33	27.19	27.85	28.45	29.00	29.48	29.92	30.32	30.47	30.62	30.77	30.91	31.04						
20	25.26	26.24	27.10	27.76	28.36	28.91	29.39	29.83	30.23	30.38	30.53	30.68	30.82	30.95						
30	25.23	26.21	27.07	27.73	28.33	28.88	29.36	29.80	30.20	30.35	30.50	30.65	30.79	30.92						
60	25.20	26.18	27.04	27.70	28.30	28.85	29.33	29.77	30.17	30.32	30.47	30.62	30.76	30.89						
5	25.89	26.80	27.66	28.32	28.92	29.48	29.95	30.39	30.79	31.09	31.24	31.38	31.51	31.64	31.77	31.90	32.02	32.14		4200
10	25.65	26.63	27.49	28.15	28.75	29.30	29.78	30.22	30.62	30.92	31.07	31.21	31.34	31.47	31.60	31.73	31.85	31.97		
20	25.56	26.54	27.40	28.06	28.66	29.21	29.69	30.13	30.53	30.83	30.98	31.12	31.25	31.38	31.51	31.64	31.76	31.88		
30	25.51	26.49	27.35	28.01	28.61	29.16	29.64	30.08	30.48	30.78	30.93	31.09	31.22	31.35	31.48	31.61	31.73	31.85		
60	25.48	26.46	27.32	27.98	28.58	29.13	29.61	30.05	30.45	30.75	30.90	31.06	31.19	31.32	31.45	31.59	31.70	31.82		

Table 5—Conversion Table to Calculate System G/T from y Factor Obtained by Sun ($\phi_{sun} = 0.9162 \times 10^{-20}$ W/Hzm^2 for $f = 3950$ MHz, $C = 8.50$ dB, $A = 8.18$ dB for $\theta = 10°$) (Date of calibration: Jan. 20, 1972, Ant. dia.: 33⅓ Ft.)

	G/T(dB)											
Freq. (MHz)	3730				3950				4170			
Diff. (dB)	−.50				0				+.48			
Elev. Angle°	5 / 5	10 / 10	30 / 30	60 / 60	5	10	30	60	5	10	30	60
Diff. (dB)	+.17	0	−.16	−.20	+.17	0	−.16	−.20	+.17	0	−.16	−.20
y_{sun}(dB)												
20.6	28.74	28.57	28.41	28.37	29.24	29.07	28.91	28.87	29.72	29.55	29.39	29.35
.7	.84	.67	.51	.47	.34	.17	29.01	.97	.82	.65	.49	.45
.8	.94	.77	.61	.57	.44	.27	.11	29.07	.92	.75	.59	.55
.9	29.04	.87	.71	.67	.54	.37	.21	.17	30.02	.85	.69	.65
21.0	.14	.97	.81	.77	.64	.47	.31	.27	.12	.95	.79	.75
.1	.24	29.07	.91	.87	.74	.57	.41	.37	.22	30.05	.89	.85
.2	.34	.17	29.01	.91	.84	.67	.51	.47	.32	.15	.99	.95
.3	.43	.26	.10	29.06	.93	.76	.60	.56	.41	.24	30.08	30.04
.4	.53	.36	.20	.16	30.03	.86	.70	.66	.51	.34	.18	.14
.5	.63	.46	.30	.26	.13	.96	.80	.76	.61	.44	.28	.24
.6	.73	.56	.40	.36	.23	30.06	.90	.86	.71	.54	.38	.34
.7	.83	.66	.50	.46	.33	.16	30.00	.96	.81	.64	.48	.44
.8	.92	.75	.59	.55	.42	.25	.09	30.05	.90	.73	.57	.53
.9	30.02	.85	.69	.65	.52	35	.19	.15	31.00	.83	.67	.63
22.0	.12	.95	.79	.75	.62	.45	.29	.25	.10	.93	.77	.73
.1	.22	30.05	.89	.85	.72	.55	.39	.35	.20	31.03	.87	.83
.2	.32	.15	.99	.95	.82	.65	.49	.45	.30	.13	.97	.93
.3	.42	.25	30.09	30.05	.92	.75	.59	.55	.40	.23	31.07	31.03
.4	.52	.35	.19	.15	31.02	.85	.69	.65	.50	.33	.17	.13
.5	.61	.44	.28	.24	.11	.94	.78	.75	.59	.42	.26	.22
.6	.70	.54	.38	.34	.21	31.04	.88	.84	.69	.52	.36	.32
.7	.80	.64	.48	.44	.31	.14	.98	.94	.79	.62	.46	.42
.8	.90	.74	.58	.54	.41	.24	31.08	31.04	.89	.72	.56	.52
.9	31.00	.84	.68	.64	.51	.34	.18	.14	.99	.82	.66	.62
23.0	.10	.94	.78	.74	.61	.44	.28	.24	32.09	.92	.76	.72
.1	.20	31.04	.88	.84	.71	.54	.38	.34	.19	32.02	.86	.82
.2	.30	.14	.98	.94	.81	.64	.48	.44	.29	.12	.96	.92
.3	.40	.24	31.08	31.04	.91	.74	.58	.54	.39	.22	32.06	32.02
.4	.50	.34	.18	.14	32.01	.84	.68	.64	.49	.32	.16	.12
.5	.60	.44	.28	.24	.11	.94	.78	.74	.59	.42	.26	.22
.6	.70	.54	.38	.34	.21	32.04	.88	.84	.69	.52	.36	.32
.7	.80	.64	.48	.44	.31	.14	.98	.94	.79	.62	.46	.42
.8	.90	.74	.58	.54	.41	.24	32.08	32.04	.89	.72	.56	.52
.9	32.00	.84	.68	.64	.51	.34	.18	.14	.99	.82	.66	.62
24.0	.10	.94	.78	.74	.61	.44	.28	.24	33.09	.92	.76	.72
.1	.20	32.04	.88	.84	.71	.54	.38	.34	.19	33.02	.86	.82
.2	.30	.14	.98	.94	.81	.64	.48	.44	.29	.12	.96	.92
.3	.40	.24	32.08	32.04	.91	.74	.58	.54	.39	.22	33.06	33.02
24.4	32.50	32.34	32.18	32.14	33.01	32.84	32.68	32.64	33.49	33.32	33.16	33.12
.5	.60	.44	.28	.24	.11	.94	.78	.74	.59	.42	.26	.22
.6	.70	.54	.38	.34	.22	33.04	.88	.84	.69	.62	.36	.32
.7	.80	.64	.48	.44	.32	.14	.98	.94	.79	.72	.46	.42
.8	.90	.74	.58	.64	.42	.24	33.08	33.04	.89	.82	.56	.52
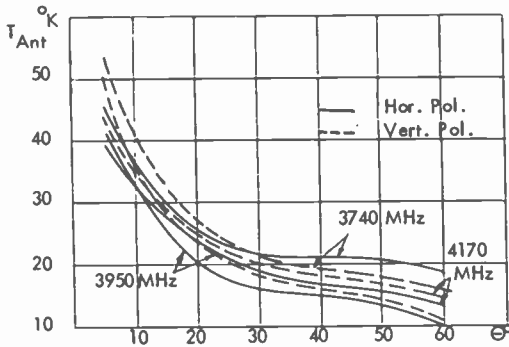
Fig. 15—Measured antenna noise temperature versus elevation angles.

dB, and according to detailed error analysis, inaccuracy limits of G/T values were within $+0.48$ dB and -0.20 dB.

The measured G/T values (normalized to $100°K$ receiving-system noise temperature) are given in Table 2. This table indicates that with the given antenna and receiver system, a G/T between 28.8 dB and 30.7 dB is possible above $10°$ elevation angles depending on the frequency and antenna elevation angle. On the other hand, the antenna is capable of producing nearly 36 dB G/T at $45°$ elevation angle at 3950 MHz with a cooled parametric amplifier at the output of the feed.
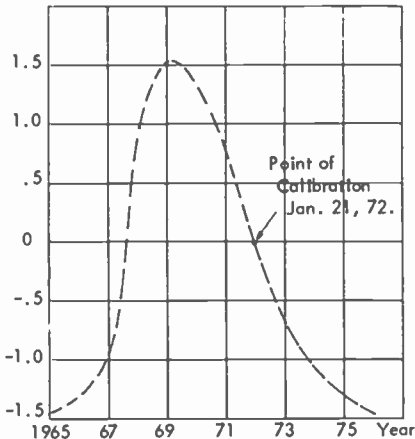
Fig. 16—Relative sun flux versus time for one 11-year solar cycle.

6. Conclusions

The design and prototype testing of a medium-size earth station antenna was completed. The results show the characteristics that can be obtained in practice on this type of system. These characteristics are equal to or better than the characteristics assumed in the design of the Telesat Canada earth station network. The results also agree with most of the assumptions used in the system design of US domestic satellite networks. Investigations into spectrum re-use potentials verified the feasibility of such techniques and the limits possible with the present state of art. Attempts in the direction of noise pollution control through improving wide-angle side-lobe levels of Cassegrainian antennas indicate that improvements are possible without significant reduction of antenna efficiency. The new antenna also exhibits a module add-on type of expansion capability that could become important in the economical design of future expandable earth-station networks.

Acknowledgments

References:

[1] **Performance Characteristics of Earth Stations,** Intelsat Document ICSC-37-38E W/1/69, 31 January 1969 and Annex No. 1 to it.

[2] **Network Television Earth Stations,** Technical specification ESC-003, June 1, 1971, Telesat Canada, Ottawa, Ontario, Canada; J. Almond and R. M. Lester, "Communication capability of the Canadian domestic satellite system," International Conf. on Communications, June 14-16, 1971, Montreal, Canada.

[3] Comsat submission to FCC ". . . satellites . . . as part of a communication satellite system . . . (for) A T and T" Reply to FCC Report and Order of March 20, 1970, Docket No. 16495 (FCC 70-306); **Domestic communications satellite system, a summary,** (RCA Global Communications Inc., March 1971; **Domestic communications satellite system,** MCI Lockheed Satellite Corp., September 1971.

[4] S. G. Komlos, P. Foldes, and K. Jasinski, "Feed system for Clockwise and Counterclockwise circular polarization" **IRE Trans. on Ant. and Prop.,** Vol. AP-9, No. 6, Nov. 1961.

[5] P. D. Potter, **A new horn with suppressed sidelobes and equal beamwidth,** JPL report, Oct. 1962, Pasadena, California.

[6] T. Murakami and G. S. Wickizer, "Ionosphere phase distortion and Faraday rotation of radio waves," **RCA Review,** Vol. 30, pp. 475-503, 1969.

[7] The radio star method of measuring G/T, Intelsat Document, Appendix A to Attachment No. 1 to Annex No. 1 to ICSC/T-23-16 E W/1/68.

Wideband Class-C Trapatt Amplifiers

A. Rosen, J. F. Reynolds, S. G. Liu, and G. E. Theriault

RCA Laboratories, Princeton, N. J.

Abstract—The operation of Trapatt amplifiers under both class C and wideband conditions has been demonstrated. In particular, amplifiers have been developed that deliver 60 watts peak output with 6.5 dB gain and 14.2% (3 dB) bandwidth and 80 watts with 5 dB gain and 12% (3 dB) bandwidth.

Introduction

One of the important potential applications of Trapatt devices is as high-power broadband pulse amplifiers for phased array radar systems. As a result of recent circuit advances, high peak powers can be obtained from these devices even when they are used as broadband (10-20%) power amplifiers.[1,2] In addition to the power and bandwidth requirements, the complexity of the radar systems and the large number of amplifier modules that are involved necessitate that a simple, economical, and efficient method be available to modulate these devices. The conventional method has been to use pulse drivers in the power supply of the amplifiers. These drivers switch the dc power on and off in synchronism with the input rf. Such drivers are, however, bulky, complicated, and expensive since kilowatts of dc must be switched at rapid rates in synchronization with the input rf.

An alternative method of providing modulation is to design the Trapatt amplifiers to operate under class-C condition[3] in a manner similar to conventional transistor amplifiers. This paper reports the results of an amplifier design program that has resulted in broadband, class-C Trapatt amplifiers. In particular, S-band, class-C Trapatt amplifiers have been developed that deliver output powers of 80 watts with 12% instantaneous (3 dB) bandwidth.

Class-C Operation

Unlike other high peak power sources such as LSA or Gunn devices, the junction nature of Trapatt devices allows them to be designed as class-C amplifiers. In class-C operation, the Trapatt diodes are dc biased below their breakdown voltage so that only negligible dc currents (a few microamperes) are drawn by the diodes when there is no rf input to the amplifier. When rf is applied, they are driven to the threshold condition for Trapatt operation by the rf, the diode operating voltage drops, large dc currents are drawn from the power supply, and the rf is amplified. When the rf drive is removed, the conditions for Trapatt operation are no longer met and the diodes automatically shut
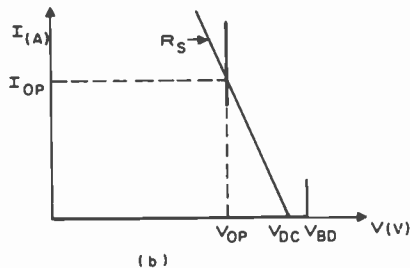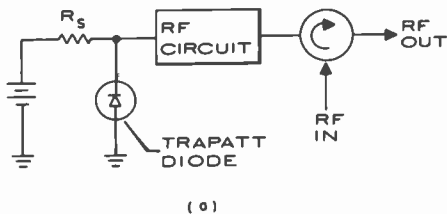
Fig. 1—(a) Circuit for Class C operation of Trapatt amplifier and (b) I-V characteristic of class-C Trapatt amplifier.

off. The circuit for this type of operation and a typical I-V charcteristic are shown in Fig. 1. The biasing requires only a dc supply and small series resistor R_s. As can be seen from the I-V characteristics, this type of operation is possible with Trapatt devices because of their diode characteristic and because the diode operating voltage (V_{op}) is less than its breakdown voltage (V_{BD}) (Fig. 1b).

Broadband Circuit Configuration

A microstrip coupled-line circuit similar to that previously described[4] is employed to achieve broadband amplification from Trapatt diodes. The basic circuit (Fig. 2) consists of two coupled lines that provide a broadband impedance transformation and, thus, proper matching at the device operating frequency. Fig. 3 shows the calculated input impedance as a function of frequency for this configuration as it would apply to an S-band Trapatt amplifier. As can be seen, the real part of the impedance varies only slightly, while the imaginary part varies slowly over a 15% bandwidth. In addition, the impedance levels shown are those typically required for a high power Trapatt amplifier and are readily obtained in practice.

$$N = \text{TRANSFORMATION RATIO} = \frac{Z_{oe} + Z_{oo}}{Z_{oe} - Z_{oo}}$$
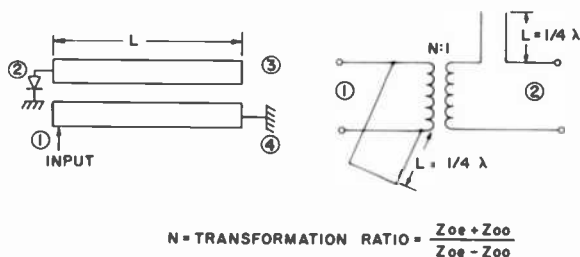
Fig. 2—Schematic and equivalent circuit for present microstrip version of coupled-line circuit.

Efficient, broadband Trapatt amplification requires that the proper voltage and current wave-shape be maintained at the device terminals over the required bandwidth. Since the wave-shape required for Trapatt operation is nonsinusoidal,[5] the proper impedance should be maintained not only at the operating frequency but also at other harmonically related frequencies over the required bandwidth. The coupled-line configuration meets these requirements because it behaves as a bandpass filter providing high reactive impedances out of band. This allows the use of idler circuits to control the harmonic impedances while maintaining the required bandwidth performance. These properties have been used prevously in varactor multiplier work[6] and are ideally suited for Trapatt amplifiers.
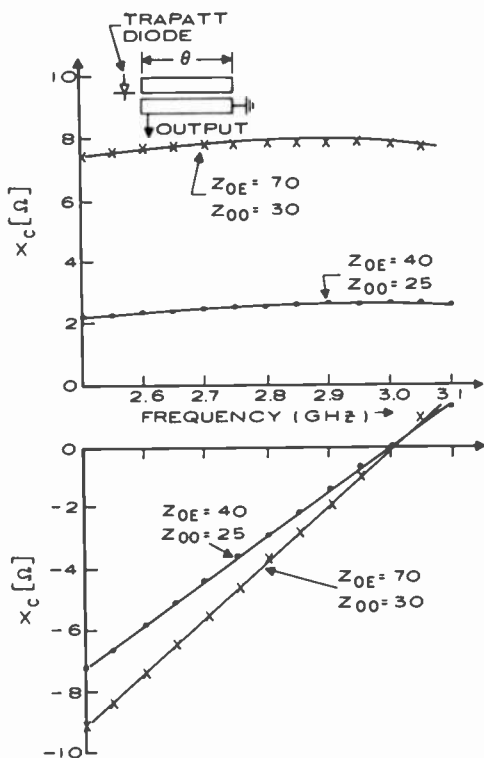
Fig. 3—Calculated input impedance as a function of frequency for typical high power Trapatt amplifier circuit. Impedances for two transformation ratios are shown.

Device Structure

The diodes used in the Trapatt amplifiers are n^+-p-p^+ type (complementary) structures. They are fabricated by diffusion of phosphorus into a p-on-p^+ boron doped silicon epitaxial wafer. Because the boron and phosphorus have nearly identical diffusion coefficients, the device has an almost symmetrical diffusion profile, that is, the out-diffusion depth from the substrate is the same as the in-diffusion depth. The diffusion depth is approximately 3 microns and the doping density and width of the p-layer are $1 \times 10^{15} cm^{-3}$ and 3.5 microns, respectively. The diameter of the diodes is 0.038 cm. Although Trapatt amplifiers have been developed with conventional p^+-n-n^+ diodes, the complementary structure is currently being used for two reasons, both related to its thermal characteristics.[7,8] First, diodes with the complementary structure operate at a lower power density than conventional

diodes, thereby leading to a lower temperature rise for a given power output. Secondly, it is possible to reproducibly fabricate high power large-area diodes with thin diffused regions with the complementary structure. This is due to the symmetric diffusion profile achieved during fabrication and reduces the thermal resistance of the device. These improved thermal properties are especially important for phased array radar systems because of the long pulse width and duty cycles involved.
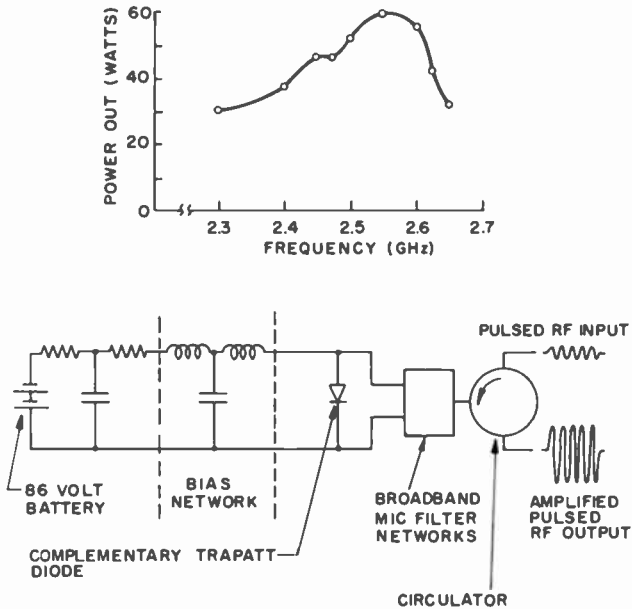
Fig. 4—(a) Power output versus frequency characteristics of class-C wide-band Trapatt amplifier (midband gain = 6.5 dB) and (b) setup for class-C operation.

Amplifier Performance

Trapatt amplifiers employing a single diode have been developed in microstrip form using various coupled-line circuit configurations. They have yielded peak output power up to 80 watts, with 5 dB gain and 12% (3 dB) instantaneous bandwidth centered at 3.3 GHz. Fig. 4b is a diagram of a typical setup for operation of these amplifiers under class-C conditions. The bias network consists of a low-pass filter and a battery source. Fig. 4a shows a typical power output versus frequency response of the amplifiers. For this case, the peak output
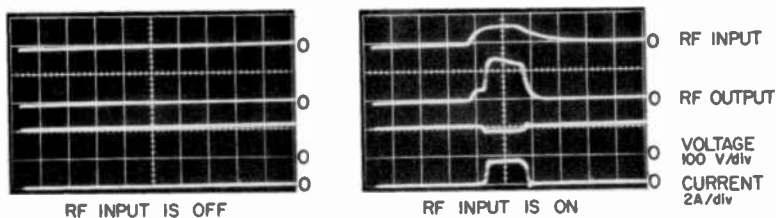
Fig. 5—Rf input, rf output, diode voltage, and current waveforms of a second-harmonic circuit operating in a class-C mode: (a) rf input is "off" and (b) rf input is "on."

power is 60 watts at 6.5 dB gain with a 14.2% (3 dB) bandwidth. Typical efficiencies are 18%.

Fig. 5 shows the voltage, current, and rf waveforms for both on and off conditions under class-C operation. As can be seen, the off state is characterized by the absence of spurious output and negligible
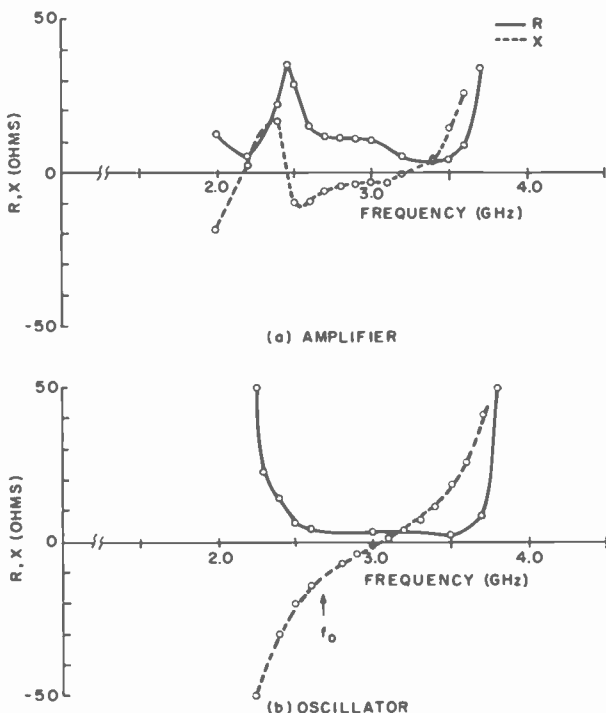
Fig. 6—Real (R) and imaginary (x) components of impedance measured on Trapatt circuit operated (a) as a stable amplifier and (b) as an oscillator.

dc dissipation (less than 1 milliwatt). In the on state, the voltage drop and current rise associated with the Trapatt mode can be observed as well as the amplified rf output.

In order to determine the conditions necessary for Trapatt amplification, impedance measurements were made on a circuit in which both stable amplification or oscillation could be obtained at the 60-watt level. The results of these measurements are shown in Fig. 6. In the oscillator case, the circuit load impedance at the output frequency (2.58 GHz) was $3.54 - j9.61$ ohms compared to $12.1 + j0.06$ for the amplifier case. The impedance at the other harmonic frequencies changed only slightly for both cases. This indicates that the primary distinction between Trapatt oscillator and amplifier performance can be accounted for by the circuit loading at the output frequency, even though Trapatt operation is highly dependent on harmonic impedances.

Fig. 6a also shows the broadband matching capability of the coupled-line circuit. As can be seen, both the real and imaginary part of the circuit impedance vary only slightly over a 15% bandwidth.

Class-C operation has also been obtained for a two-stage amplifier configuration. This type of operation is important for applications where higher gain is required. Total gain as high as 12 dB across a 5% (3 dB) instantaneous bandwidth has been obtained to date.

Conclusion

We have shown that Trapatt amplifiers are capable of broadband, class-C operation. These characteristics, together with their peak power, high efficiency, and duty cycle capability, qualify them for use as solid-state power amplifiers in phased array radar systems, as well as other commercial and military communication systems.

Acknowledgment

References:

[1] A. Rosen, J. F. Reynolds, and J. M. Assour, "Broadband High-Power Trapatt Diode Amplifier at S-Band," **Electronics Lett.**, Vol. 7, No. 26, 1971.

[2] H. Kawamoto and E. L. Allen, "Wideband Microwave Amplifier with Two Anti-parallel High-Efficiency Diode Pairs," **Electronics Lett.**, Vol. 7, P. 602, 1971.

[3] S. G. Liu, H. J. Prager, K. K. N. Chang, J. J. Risko, and S. Weisbrod, "Harmonic Extraction and Triggered Amplification with High-Efficiency Avalanche Diodes," presented at ISSCC, Philadelphia, Feb. 1971.

[4] A. Rosen, J. F. Reynolds, and J. J. Thomas, "Improved Coupled-Line Microstrip for L- and S-Band Oscillators," **Electronics Lett.,** Vol. 8, No. 5, p. 136, 9 March 1972.

[5] A. S. Clorfeine, R. F. Ikola, and L. S. Napoli, "A Theory for the High-Efficiency Mode of Oscillation in Avalanche Diodes," **RCA Review,** Vol. 30, p. 397, Sept. 1969.

[6] A. Rosen and E. Belohoubek, "Coupled Microstrip Line Varactor Doublers," **IEEE Trans. on Microwave Theory and Technique,** May 1969.

[7] S. G. Liu and J. J. Risko, "Microwave Oscillation and Amplification with Complementary Silicon Avalanche Diodes," presented at the Int. Electron Devices Meeting, Washington, D. C., Oct. 1971.

[8] S. G. Liu, **High-Peak-Power, High-Efficiency Microcircuit Avalanche Diode Oscillators,** Final Report for Sandia Laboratories, Albuquerque, New Mexico, Feb. 1972.

1-2 GHz High-Power Linear Transistor Amplifier*

A. Presser and E. F. Belohoubek

RCA Laboratories, Princeton, N. J.

Abstract—An octave-bandwidth transistor power amplifier is described that has performance characteristics that in most respects are superior to those of present traveling-wave tubes. The prototype module provides a large-signal gain of 27 dB with a power output ranging from 8.3 to 11.5 watts over the frequency range from 980 to 1960 MHz. The module, fabricated in hybrid integrated-circuit form, measures 5.65 × 1.5 × 0.93 inches and operates from a 17-volt power supply with an overall efficiency close to 20%.

Introduction

The wide-band microwave amplifier field has been dominated for many years by the traveling-wave tube (TWT). Recently, however, transistor amplifiers have begun to compete with and replace TWT's in many applications, especially in the low-noise area. Class-A transistor amplifiers are now available at frequencies up to C-band that equal or better the general performance characteristics of TWT's, such as noise figure, bandwidth, gain flatness, and linearity. In addition, the transistor amplifier offers the advantages of lower volume and weight, simpler power supply requirements, and higher reliability.

In the area of medium-power amplifiers with power outputs of several watts, the bandwidth of presently available class-C amplifiers is generally limited to less than 10 to 30%, depending upon operating frequency. This limitation is due to the inability to provide a good input match to class-C power transistors over a wide frequency range. The transistor thus does not receive sufficient input power for turn-on. This effect becomes increasingly pronounced at frequencies above 1 GHz, where the input Q of the transistor, which depends upon parasitic lead reactances and the input resistance of the transistor, becomes very high. The output circuit usually can be broad-banded more easily or, at the least, power output and efficiency can be traded for bandwidth.

The input matching limitation can be overcome by class-A operation of the transistor. This not only eliminates the turn-on problem but also results in a larger stage gain that can be used to offset the lower efficiency of class-A operation. The success of this approach depends upon the availability of power transistors suitable for class-A operation and the use of design techniques that permit optimization of power output and gain over a wide frequency range. S-parameter design alone, used very successfully in small signal class-A amplifiers, is not sufficient when high power output and good efficiency are required over a wide bandwidth. Special design techniques based on load-pull measurements are necessary to provide a more systematic approach to the development of class-A power amplifier stages.

This paper describes such techniques as developed and applied to the design of a 1 to 2 GHz power amplifier module with 30 db gain and a nominal saturated power output of 10 watts. The amplifier module consists of three balanced stages. The first two stages employ standard commercial 2N5920 transistors, while the power stage makes use of a modified version of the 2N5921. This power transistor is equipped with emitter ballasts that permit operation under heavy forward bias, as is necessary for class-A power amplification.

General Design Considerations

The successful design of a linear broad-band power amplifier depends upon the realization of a suitable input and output circuit for a particular transistor that produces the required stable gain and bandwidth simultaneously with good power output and efficiency. Unfortunately, there exists no unified transistor circuit model in the microwave region that permits calculation of all these amplifier parameters. The transistor properties at microwave frequencies are usually

characterized by S-parameters[1,2] at some convenient external terminal and reference impedance.

When evaluated over a frequency band of interest, the four S-parameters represent the transistor as a two-port network that specifies its small-signal terminal behavior in that frequency band. Bandwidth, gain, and stability can be predicted for any circuit configuration surrounding the transistor with the aid of these S-parameters. Power output, on the other hand is not predictable by the S-parameters and is a function of the power-handling capacity of the transistor, the dc-bias point, and the load impedance. Since the range of suitable load impedances is also limited by gain, bandwith, and stability requirements, a careful compromise must be made. The additional information is obtained from measured data on an initial amplifier circuit. This data is used to optimize the circuit over the full bandwidth. The flow chart of such a design routine is shown in Fig. 1.
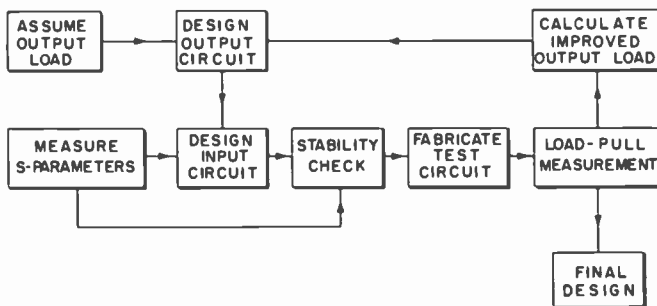
Fig. 1—Design flow chart.

The first task is to devise an output circuit that provides a load resistance corresponding to the power output capability of the transistor. The circuit must also minimize the reactive load presented to the transistor, which includes compensation of the base-collector capacitance. This procedure follows closely the design outline for the output circuit of class-C amplifiers.[3] It is convenient for computational purposes to represent the transistor in its microstrip carrier by an equivalent source circuit as shown in Fig. 2. In this circuit, R_o represents the load resistance required for the desired power output, C_{ob} is the base–collector capacitance, L_P and L_B are parasitic inductances of the transistor carrier in a grounded base configuration, and L and C are tuning elements added to the transistor carrier. Using this circuit and selecting a suitable transmission-line topology for the output network, the

dimensions of the transmission line elements for best match are calculated using a computer optimizing search routine.[4]

The next step is to design the input circuit for the amplifier using the measured S-parameters and the previously determined output circuit. A suitable input-circuit topology is selected and the transmission-line elements for this circuit are computer optimized over the required frequency range. Prior to fabrication of the test circuit, a stability check[2] is performed and, if necessary, circuit modifications are made to ensure stability.
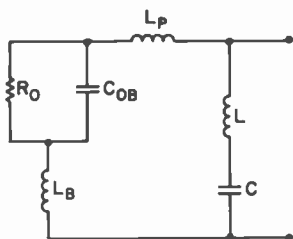
Fig. 2—Transistor equivalent source circuit.

The amplifier design at this point cannot be expected to provide efficient power output over the entire design frequency range, but is used to construct a trial amplifier that is suitable for load-pull characterization.[5,6] Since it is not possible, generally, to devise an output circuit that presents the optimum* load impedance to the transistor at each frequency over a wide bandwidth, the designer needs information about the influence of moderate mismatches in the output on the performance of the amplifier. The load-pull diagram fulfills this function. The output power of the trial amplifier is recorded as a function of load impedance referenced to the transistor carrier. Based on this information, curves of constant power output are plotted on a Smith chart at several frequencies throughout the design band. These data are then used to optimize the output circuit, and the design cycle for the input circuit is repeated until a satisfactory final design evolves. Examples of load-pull diagrams are given later.

It is apparent that the design procedure is rather tedious, and successful application depends on the use of time-saving features such as computer optimization and accurate computer-controlled microwave measurements. Load-pull data evaluation is greatly facilitated by an

_____

* Optimum is defined here as the load impedance that provides maximum power output.

electronically controlled variable mismatch.[7] This instrument, shown in Fig. 3, consists of a modified slotted precision line that is equipped with two moveable dielectric slugs. The distance between the slugs determines the VSWR, while their relative position with respect to a reference terminal provides the phase of the variable mismatch. The separation and position of the slugs are controlled by servo-motors that can be computer controlled for automatic measurements.
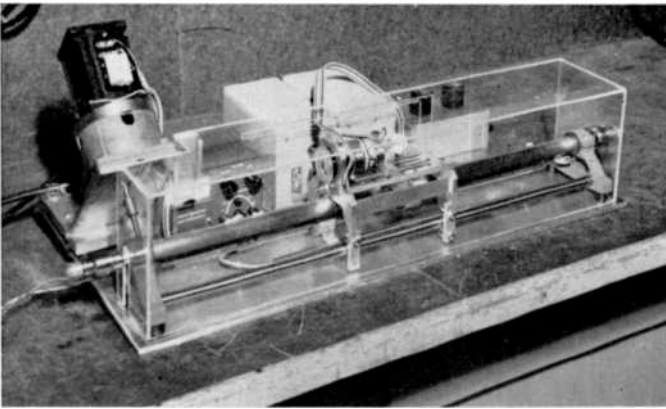
Fig. 3—Servo-controlled variable mismatch.

Driver Amplifier Stages

The driver comprises the first two stages of the amplifier module. The 2N5920 transistor chip is used in both these stages, which together have to provide 20 db gain and a power output of one watt. This transistor is capable of delivering two watts of saturated power output at 2 GHz in class-C operation. The chip is not emitter ballasted, but is small enough to have a fairly even thermal distribution and to permit class-A forward biasing with an approximate power output of 700 mW at the 1-dB gain compression point.

   The transistor chip is mounted in a microstrip carrier suitable for wide-band operation. The construction of the carrier is shown in Fig. 4. The main body of the carrier is made of highly thermal and electrical conductive copper–tungsten, to which both a BeO pedestal and an alumina wafer are brazed. The transistor chip is mounted on the BeO pedestal. Base and emitter bonds as shown complete the carrier, which has a minimum of parasitic reactances and excellent heat conduction and which permits easy inter-connection with microstrip circuitry.

   Employing the design technique outlined in the previous section,
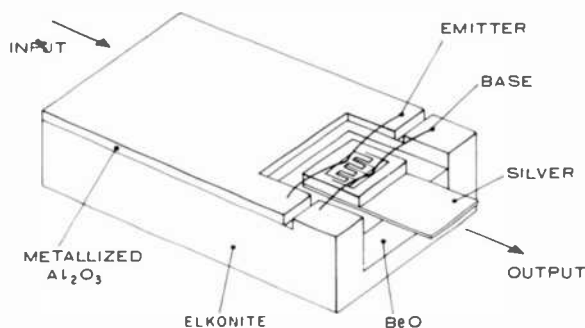
Fig. 4—Microstrip carrier for 2N5920.

the input and output circuits for a single-transistor amplifier are first synthesized using the measured S-parameters of the 2N5920 in the microstrip carrier. The amplifier circuit is next constructed, tested, and experimentally optimized to give best performance over the 1 to 2 GHz frequency band. The final amplifier circuit is used as a building block for both driver amplifier stages and also serves as a test fixture for rf-evaluation of the transistors for these stages.

Each driver stage consists of two amplifiers connected in a balanced configuration[8] between two 3-dB hybrids. This arrangement ensures low input and output VSWRs and thus greatly eases the cascade of amplifiers and provides excellent isolation between successive stages. A photograph of a complete driver stage is shown in Fig. 5. Each transistor is biased separately at a quiescent collector current of 160
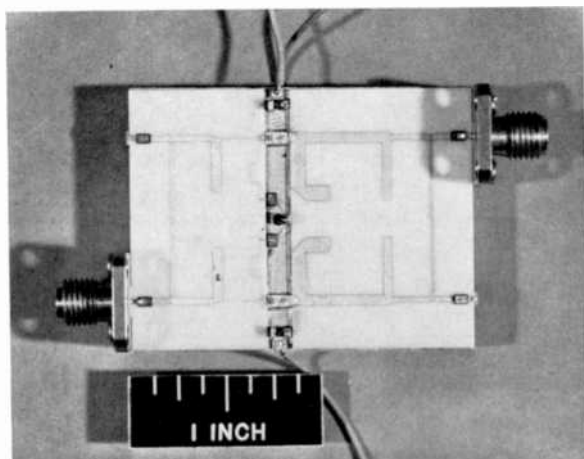
Fig. 5—Photograph of driver amplifier stage.

mA. The broad-band performance of this stage at drive levels of 10 and 100 mW is illustrated in Fig. 6. At the one-watt power output level, the gain deviates by less than 1.5 dB from the small-signal gain over the 1 to 2 GHz frequency range.

The same amplifier configuration is used in the first driver stage, the only difference being that the quiescent collector current is reduced to 80 mA, which improves the efficiency of the amplifier module.
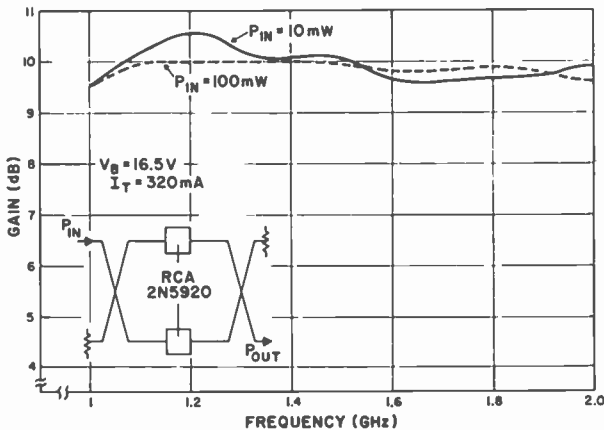
Fig. 6—Performance of driver amplifier stage.

Power Amplifier

Nearly all of the presently available commercial power transistors are designed for class-C operation, and do not permit operation under strongly forward-biased conditions. A typical transistor, such as the 2N5921, is capable of delivering 5 to 10 watts cw in class-C operation in the 1 to 2 GHz frequency band. However, if such a transistor is forward biased for class-A operation, its gain decreases very rapidly for collector currents above 200 mA. Fig. 7 shows the typical gain dependence of an unballasted transistor as a function of collector current. The effect is most pronounced in large-area, high-power transistors in which hot spotting leads to a very strong thermal imbalance above a certain dissipation level. The presence of rf-drive evens this thermal imbalance as illustrated by the gain curves plotted for 10- and 100-mW input power.

Substantial power outputs in class-A operation can be attained either by placing many separately biased small transistors in parallel or by using a large ballasted transistor. The performance of a bal-lasted version of the 2N5921, the TA8170, is illustrated in Fig. 8. This
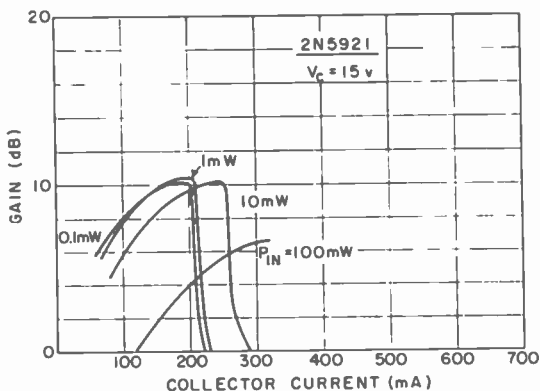
Fig. 7—Gain as function of collector current (2N5921).

transistor shows a gradual gain fall-off for collector currents above 250 mA, but does not exhibit the thermal instability of the 2N5921. Class-A operation with collector currents up to 600 mA at a collector voltage of 15 volts is possible, making this transistor suitable for the power stage of the amplifier module.

The transistor pellet is mounted in a special microstrip carrier that includes both input impedance transformation and output tuning. A sketch of the carrier and its equivalent circuit is shown in Fig. 9. The shunt inductance L is used to compensate C_{OB} and is placed as close as possible to the transistor pellet. The dc blocking capacitor C has to provide a nearly frequency-independent rf-short for the shunt inductor, and thus is in excess of 100 pF.
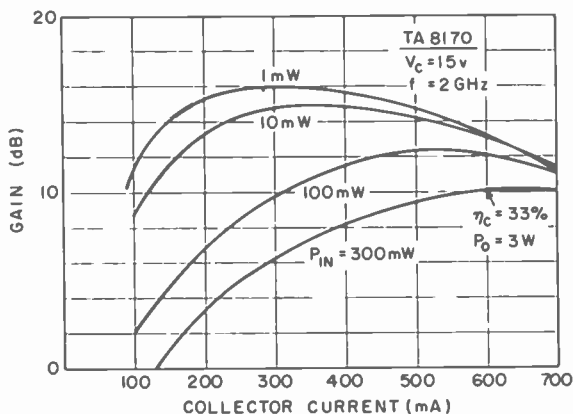
Fig. 8—Gain as function of collector current (TA 8170).

The distributed circuit input and output networks are synthesized for a small-signal gain of 10 dB using a computer-optimization program in conjunction with the measured S-parameters of the transistor in the tuned microstrip carrier and assuming a suitable output load for 2.5 watts power extraction. A photograph of the initial single-transistor trial amplifier fabricated with these circuits is shown in Fig. 10. In this form the amplifier produces a power output of 1.5 to 2 watts with 9 db gain over the 1 to 1.6 GHz frequency range.
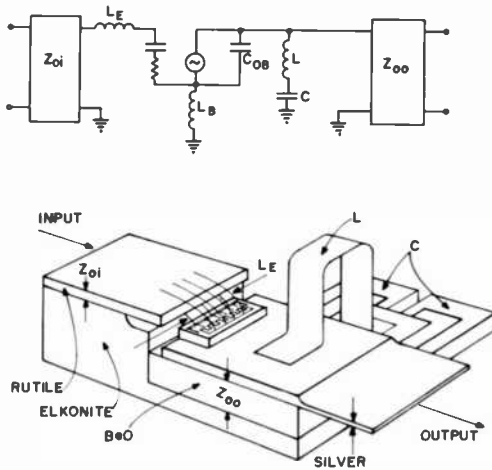
Fig. 9—Microstrip carrier for TA8170.

The load-pull characteristics are then measured to improve the performance of the amplifier over the entire frequency range. The Smith chart plot in Fig. 11 shows a typical load-pull diagram of the trial amplifier at 1.8 GHz. The load-impedance contours for constant power output at a constant power input of 300 mW are plotted. The large-diameter contour set is referenced to the output terminal of the amplifier, while the small-diameter set represents the corresponding calculated values as they appear at the collector terminal of the transistor carrier. These measurements are repeated at several frequencies within the designed operating range.

The solid curve in Fig. 12 shows the location of optimum load impedance values (maximum power output) referenced to the transistor carrier as a function of frequency. At each one of these frequencies a set of constant-power contours (not shown here) determines what power output can be attained for a given mismatch. The topology of the out-
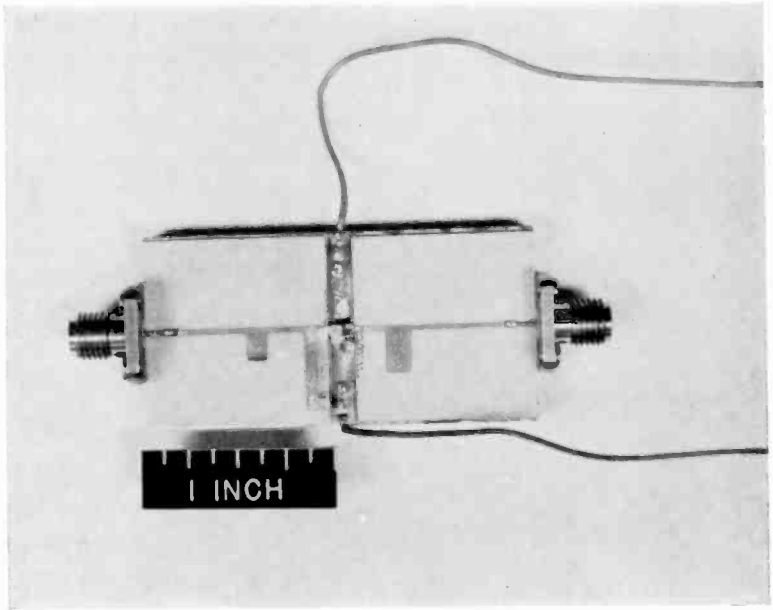
Fig. 10—Photograph of initial single-transistor power amplifier.
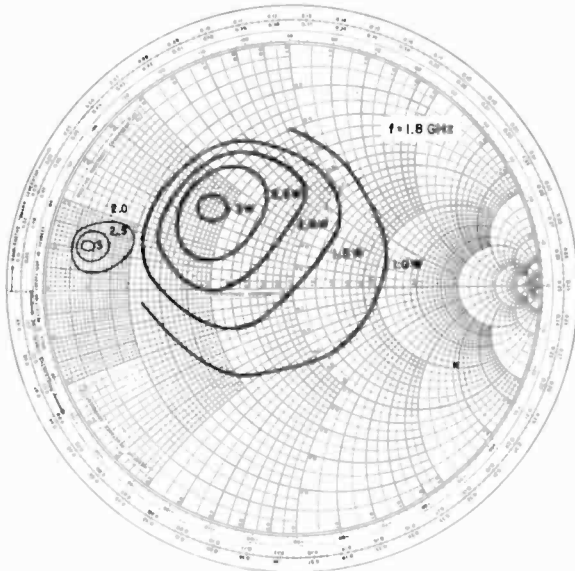
Fig. 11—Load-pull diagram of TA8170.
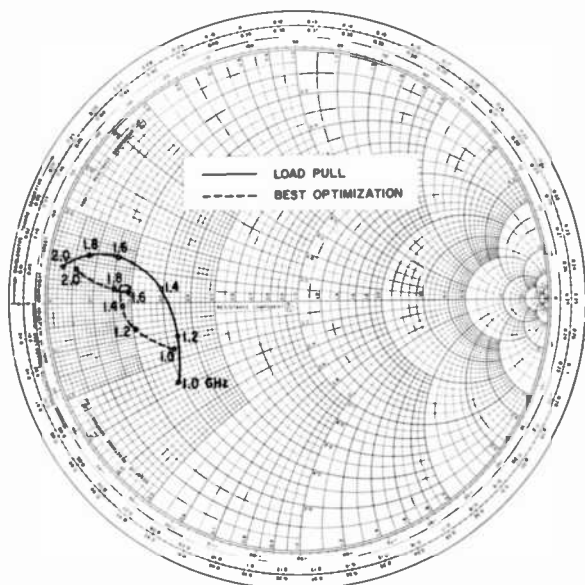
Fig. 12—Optimum load impedance locus versus frequency.

put circuit and the values of the individual circuit elements are then optimized to provide a certain minimum power output (2.5 watts) over the frequency range. The dashed curve in Fig. 12 represents the calculated impedance of the output circuit determined by an optimum search routine. The measured performance of the amplifier with the optimized circuits is presented in Fig. 13. With a constant-power input
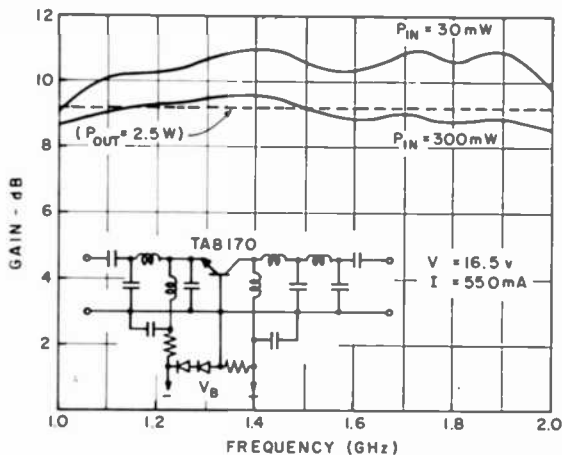
Fig. 13—Performance of optimized updated single-transistor power amplifier.

of 300 mW, the gain varies between 8.3 and 9.5 dB over the 1 to 2 GHz frequency range, which corresponds to a power output of 2.0 to 2.6 watts.

In the final configuration of the power amplifier stage, four TA8170 transistors are combined to achieve the full power output. Two transistors are directly rf paralleled but separately dc biased in a common circuit to form a nominal 5-watt amplifier. The circuits use the same topology as the single-transistor amplifier but different element values. Two of these amplifiers are finally combined in a balanced amplifier arrangement.
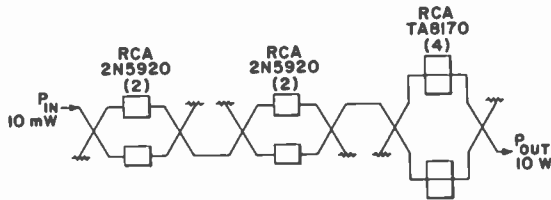
Fig. 14—Block diagram of amplifier module.

Amplifier Module Construction and Performance

The circuit block diagram of the three-stage module is shown in Fig. 14. All stages are balanced and operate class-A. The rf circuits of the module are fabricated on alumina substrates using Cr-Cu-Au thin-film technology. The individual circuit boards and microstrip carriers of the transistors are soldered to brass circuit bases. These bases are joined together after the stages are pretested and then inserted into a hermetically sealable aluminum housing.

The geometrical layout of the amplifier module in Fig. 15 shows the five circuit boards of the three amplifier stages. The ceramic substrates are mounted on circuit bases that are equipped with channels to provide room for the dc bias circuit for all eight transistors of the module. The dc bias diagram, Fig. 16, shows below the dashed line the resistors and diodes that are mounted in the circuit-base channels. The dc-supply terminals are floating, i.e., isolated from rf-ground. The entire module outline, exclusive of the connectors, measures $5.65 \times 1.5 \times 0.925$ inches. A photograph of the complete module before sealing is shown in Fig. 17.

The final measured performance of the amplifier module at a case temperature of 30°C is summarized as follows:
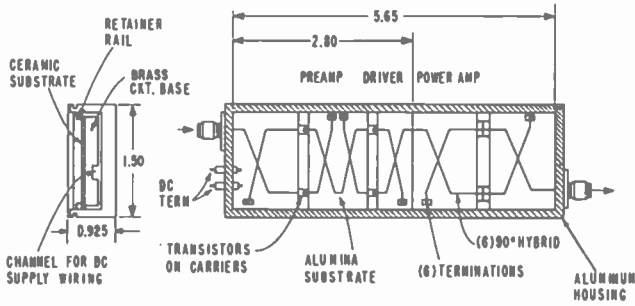
Fig. 15—Layout of amplifier module.
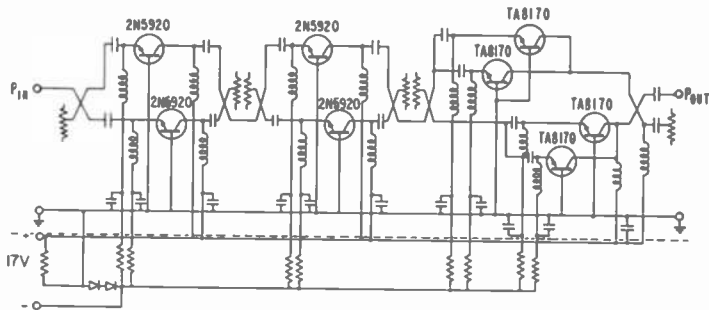
Fig. 16—DC-Bias circuit of amplifier module.
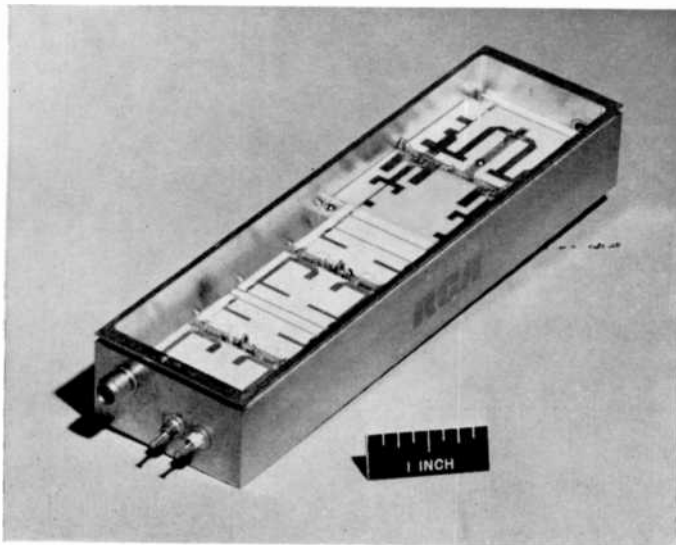
Fig. 17—Photograph of amplifier module.

Frequency	.98 to 1.96 GHz
Power output $(P_{in} = 10 \text{ mW})$	8 ± 1.4 W
$(P_{in} = 20 \text{ mW})$	9.9 ± 1.6 W
Gain $(P_{in} = 10 \text{ mW})$	28.9 ± 0.8 dB
$(P_{in} = 20 \text{ mW})$	26.9 ± 0.7 dB
Efficiency $(P_{in} = 10 \text{ mW})$	$17.5 \pm 3.1\%$
$(P_{in} = 20 \text{ mW})$	$20.8 \pm 3.4\%$
Noise figure	15 dB maximum
Input VSWR	1.33:1 maximum

Fig. 18—Gain and efficiency versus frequency.

The plot in Fig. 18 shows gain and efficiency as a function of frequency for three different power-input levels.

Conclusions

Measurement techniques using power-load contour characteristics originally developed for class-C amplifiers were extended to class-A amplifier design. These techniques together with optimum search computer routines greatly facilitated the development of a full-octave-bandwidth power amplifier having both high gain and high efficiency. Aside from radiation resistance and high-temperature operation, the transistor power amplifier proves to be superior to present-day traveling-wave

tubes in all important characteristics—size, weight, shock resistance, overall efficiency, gain flatness, reliability, and simplicity of power-supply requirements. The latter may be of special importance in air-borne applications in which a single low-voltage supply is superior to the complex high-voltage, converter power supplies for TWTs with their associated rf interference problems.

Class-A operation is the key to successful development of very wide-band amplifiers at frequencies above 1 GHz. This, however, requires the use of well-ballasted transistors capable of heavy forward biasing without thermal runaway. Fortunately, most transistor manufacturers realize this trend, and increasingly greater emphasis is placed on linear operation at microwave frequencies. Recent experimental transistors have shown linear operation at 4 GHz with 8 db gain with 600-mW power output at the 1-dB gain compression point.* A power amplifier, similar to the one described here and having several watts of power output, can thus be expected to cover the 2 to 4 GHz range in the near future.

Acknowledgment

References:

[1] K. Kurokawa, "Power Waves and the Scattering Matrix," **IEEE Trans. MTT,** Vol. MTT-13, p. 194, March 1965.

[2] G. E. Bodway, "Two-Port Power Flow Analysis Using Generalized Scattering Parameters," **Microwave J.,** Vol. 10, No. 6, p. 61, May 1967.

[3] O. Pitzalis and R. A. Gilson, "Broadband Gigahertz Transistor Power Amplifiers," **Digest IEEE 1971 International Conv.,** p. 360.

[4] V. S. Gelnovatch, et al, "A 2-4 GHz Integrated Transistor Amplifier Designed by an Optimal-Seeking Computer Program," **Digest of International Solid-State Circ. Conf.,** (1970).

[5] E. Belohoubek, et al, "S-Band CW Power Module for Phased Arrays," **Microwave J.,** Vol. 13, No. 7, p. 29, July 1970.

[6] E. Belohoubek, "Wideband Microwave Transistor Power Amplifiers," **Digest IEEE 1971 International Conf.,** p. 364.

[7] M. J. Schindler, "A Fast Data-Acquisition System for a Time-Sharing Computer," **IEEE Trans. MTT,** Vol. MTT 20, p. 54, Jan. 1972.

[8] K. M. Eisele, R. S. Engelbrecht, and K. Kurokawa, "Balanced Transistor Amplifier for Precise Wideband Microwave Applications," **Digest of International Solid-State Circ. Conf.,** 1965.

* Developed by the RCA Solid-State Division, Somerville, N.J.

Integral Heat Sink Transferred Electron Oscillators

S. Yegna Narayan and John P. Paczkowski
RCA Laboratories, Princeton, N. J.

Abstract—An integral heat sink technology has been developed for the fabrica-
tion of TEOs that results in an increase in typical oscillator efficiency
to between 6 and 9%. Integral heat sink TEOs fabricated from several
GaAs wafers operated at these efficiencies. The highest efficiency ob-
tained to date from such TEOs is 14% with a power level of 105 mW
at 8 GHz. This is believed to be the highest efficiency reported to
date for cw TEOs. The highest output power obtained to date from
a single integral-heat-sink mesa is 400 mW at 11.3 GHz with 6.4%
efficiency, while the best single mesa output-power—efficiency combi-
nation obtained is 305 mW at 10.5 GHz with 9% efficiency. This paper
describes a simple analysis carried out to generate guidelines for the
development of device technology, the integral-heat-sink technology,
and the results obtained from integral-heat-sink devices.

Introduction

The excellent noise properties of transferred electron oscillators
(TEOs) coupled with their relatively low operating voltages makes
them attractive for portable battery operated applications. As a result
cw TEOs are finding increasing use in commercial and military
systems. The major drawback of TEOs has been their low operating
efficiency. Commercial TEOs have typical efficiencies of 2 to 3%, while
efficiencies obtained in the laboratory are typically 4 to 6% with

occasional devices achieving close to 10%. We have now developed an integral heat sink technology that has increased typical TEO efficiencies to between 6 and 9%. Integral heat sink TEOs fabricated from several GaAs wafers have operated at these high efficiencies. The highest efficiency obtained to date from such TEOs is 14% with a power level of 105 mW at 8 GHz. This is believed to be the highest efficiency reported for cw TEOs. The highest output power obtained to date from a single integral heat sink mesa is 400 mW at 11.3 GHz with 6.4% efficiency, while the best single mesa output-power–efficiency combination obtained is 305 mW at 10.5 GHz with 9% efficiency.

Thermal Analysis

The potential of transferred electron devices as high efficiency oscillators has been demonstrated under pulsed conditions. Efficiencies as high as 32% in L-band[1] and 22% in X-band[2] have been achieved. In contrast, typical cw efficiencies in C and X-band have until recently been of the order of 3 to 5%. This difference between pulsed and cw efficiencies is attributed mainly to the higher power dissipated under cw conditions and the consequent temperature rise. The three important temperatures for cw TEOs are (1) the average active layer temperature T_{av}, (2) the temperature gradient across the active layer ΔT, and (3) the maximum active layer temperature T_{max}. These temperatures are interrelated; the first two effect oscillator efficiency while the third effects device reliability. In general high T_{max} leads to low reliability.

Effect of T_{AV} and ΔT on TEO Efficiency

(a) *Effect of T_{av}*: The efficiency of TEOs is proportional to the current peak/valley ratio β, since this determines the allowed rf current swing at a fixed bias voltage. β is in turn proportional to the electron velocity peak/valley ratio in GaAs. It has been established that the velocity peak/valley ratio in GaAs decreases with increasing lattice temperature.[3] The TEO efficiency, therefore, decreases with T_{av} and this is thus a fundamental limitation.

(b) *Effect of ΔT* The temperature gradient across the device causes the material properties to become nonuniform over the active layer. In epitaxial GaAs doped with shallow donors, in the temperature range of 300°-600°K, the electron concentration n is temperature independent, while electron mobility μ varies inversely as the lattice tempera-

ture. ΔT consequently causes a resistivity gradient which, in turn, causes an electric field gradient with the hotter part of the active region at a higher field. As soon as this region reaches threshold field, the current is pinned and any further increase in voltage is absorbed therein. This effect limits the device peak current and hence β.[4] The limitation imposed is not, however, a fundamental one, since ΔT can be decreased by proper design of the device geometry.

One can also, in principle, tailor the doping density in the active region to keep $n(x)\ \mu(x)$ constant and completely eliminate the effect of ΔT on β.
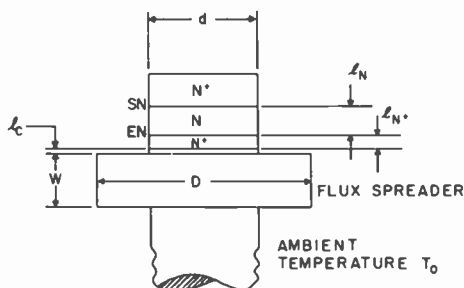
Fig. 1—Diagram of a typical TEO.

Effect of Device Geometry

We will now discuss the effect of device geometry on T_{max}, T_{av}, and ΔT and consider how these parameters can be minimized. Fig. 1 shows a typical single heat-sink TEO structure. T_{max}, T_{av}, and ΔT are computed for this structure assuming one dimensional heat flow and neglecting joule heating in the low resistivity n+-layers. The thermal conductivities of n and n+ GaAs are approximated by $150/T$ and $120/T$ respectively where T is the temperature in °K.[5] The analysis is then extended to dual-heat-sink structures in which a fraction $(1 - \delta)$ of the heat flux flows through the substrate–active-layer interface (SN). A simplified device model neglecting domain formation and assuming a cubic current/voltage characteristic[6] is then used to compute trends in device efficiency. The details of this analysis are given in the Appendix. The results of computations for typical X-band structures with $l_n = 10\ \mu$m are presented in Figs. 2 to 6, and are discussed below.

(a) The effect of mesa diameter on T_{max} and ΔT (Fig. 2) For a given bias/threshold ratio α, both T_{max} and ΔT increase with diameter.

This implies that for a given T_{max} and ΔT, higher bias voltages can be used for smaller diameter devices. In general, efficiency increases with bias voltage for fixed T_{max} and ΔT. For high efficiency operation, it is thus clear that small diameter devices should be used. The physical reason for this effect is that, with small diameter devices, one takes full advantage of thermal spreading in the heat sink. This
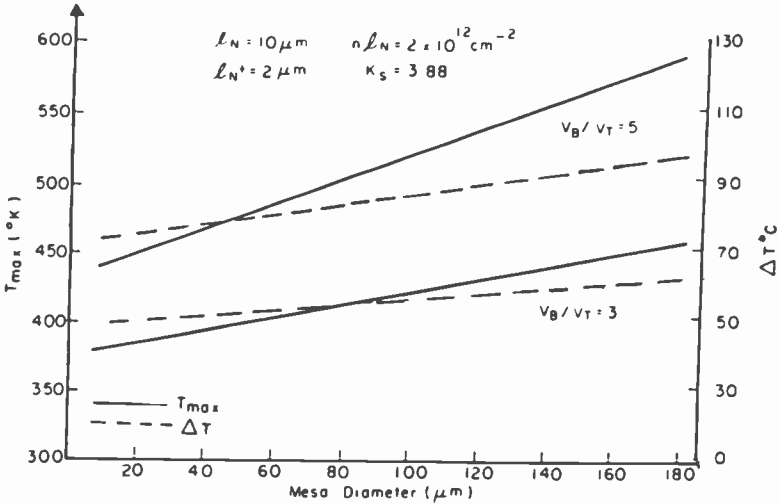
Fig. 2—T_{max} and ΔT as a function of device diameter for a typical X-band TEO.

effect can be further enhanced by using geometries that have high perimeter/area ratio for a given active area, such as annular rings,[7] stripes, etc. If we remove the one dimensional restriction and allow lateral thermal variation, even more stringent constraints will be placed on the device diameter.

(b) *Effect of dual heat sinking (Fig. 3)*   Dual heat sinking can significantly reduce T_{max}, even when $\Delta = 2(1-\delta) = 0.5$, i.e., with only 25% heat flux removal from the SN interface. In order to have any heat removal from the SN interface, it is necessary to reduce the substrate thickness to the order of the epitaxial n+ thickness. For X-band devices this involves using an n+-n-n+ GaAs wafer thickness of the order of 15 μm.

(c) *Effect of K_s (Fig. 4)*   Using a thermal flux spreader of higher thermal conductivity reduces T_{max}. Or, for a given T_{max}, the use of a higher thermal conductivity heat spreader allows the use of larger
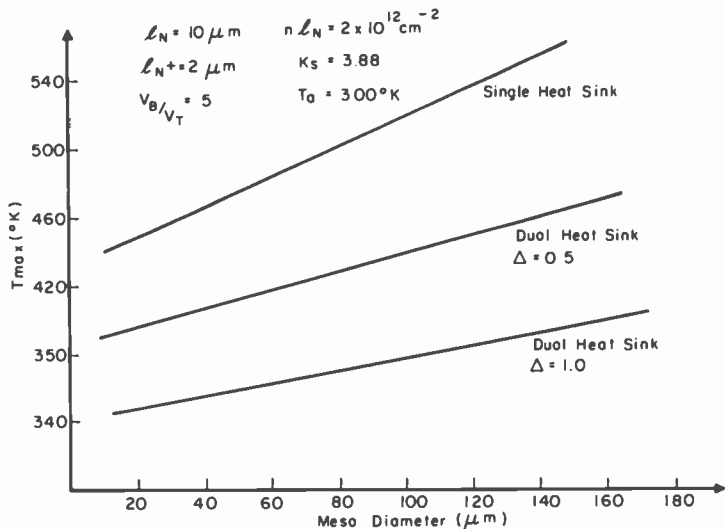
Fig. 3—Effect of dual heat sinking. Even a dual heat sinking efficiency of 50% (i.e., 25% heat removed from top contact) has a dramatic effect on T_{max}.

diameter devices and hence higher output-power capability. While type 11A diamond flux spreaders have the highest thermal conductivity, technological problems and high cost make them unattractive for general applications.
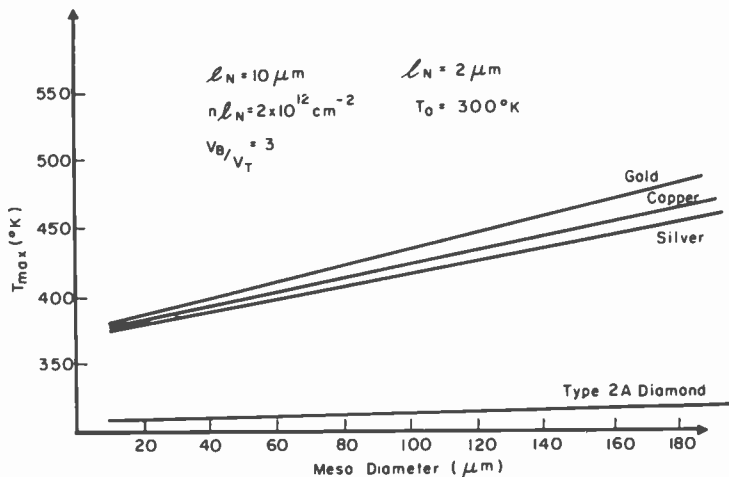
Fig. 4—Effect of thermal conductivity of heat spreaders.

(d) *Effect of* nl_n *product (Fig. 5)* Increasing the nl_n product increases the thermal flux density Q and hence T_{max} and ΔT. The lower limit is set at 1×10^{12} cm^{-2} by space-charge considerations, while thermal dissipation sets an upper limit of the order of 3×10^{12} cm^{-2}.
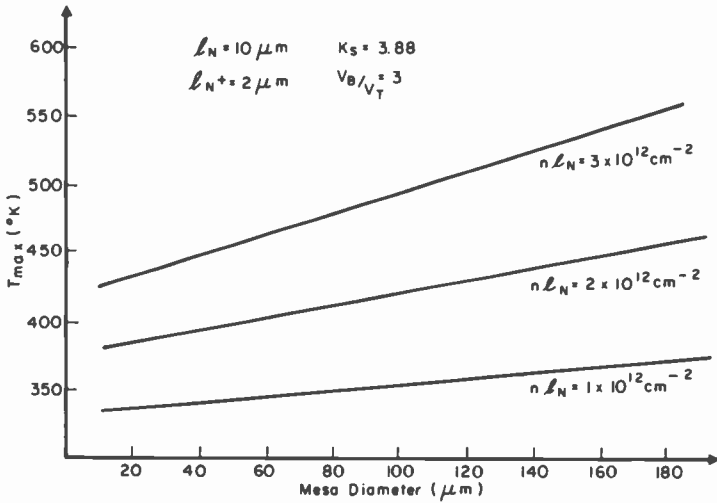
Fig. 5—Effect of the nl_n product on T_{max}.

(e) *Effect of device diameter on* β *and efficiency (Fig. 6)* Three cases are considered: (A) a device with a thermal gradient, corresponding to typical cw operation, (B) device with uniform n-layer temperature maintained at the same average temperature as the corresponding case (A) device, and (C) an ideal dual heat sink device. Case (B) is equivalent to a pulsed device operated in an oven, the oven temperature being maintained at the corresponding case (A) average temperature. Fig. 6 shows that, (1) β and η decrease with increasing device diameter, (2) the thermal gradient has a more drastic effect than the average temperature, consistent with the experimental observations in Ref. [4] and [3]. Dual heat sinking increases efficiency significantly by reducing both T_{max} and ΔT.

Integral-Heat-Sink Technology

Based on the above analysis we can generate guidelines for the development of TEO technology. Technology developed for high efficiency

TEOs should be capable of the following:

(1) Fabrication of small-diameter (<100 μm) devices. It should also allow the fabrication of ring and stripe geometry devices.

(2) Fabrication of dual-heat-sink structures. For X-band operation, this implies that all excess GaAs should be removed, leaving a total thickness of the order of 15μm.

(3) Fabrication of multiple mesa devices for high output power operation.

(4) Achieving an intimate mechanical bond between device and heat spreader to assure low thermal resistance.
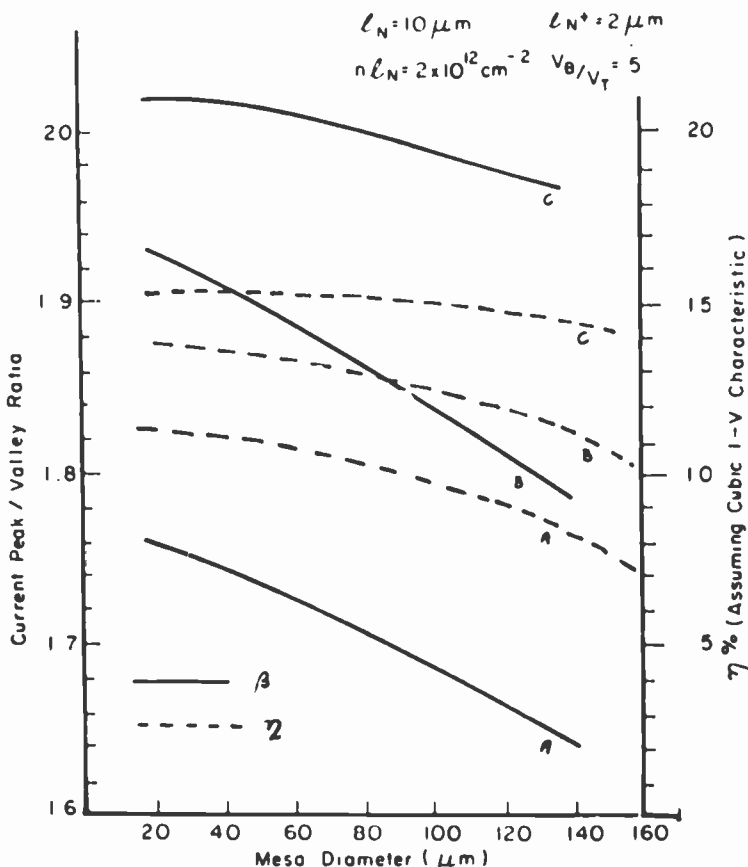
Fig. 6—α and η as functions of device diameter. Case (A) device with temperature gradient, a typical cw device, case (B) device without temperature gradient maintained at the same average temperature as in case (A) and case (C) an ideal dual heat sink device.

An integral heat sink technology for the fabrication of high efficiency TEOs was developed based upon these guidelines. Its main features as illustrated in Fig. 7 are as follows.

(1) Starting with an epitaxially grown n+-n-n+ GaAs wafer, ohmic contacts are deposited on the thin n+ layer. This n+ layer is 1 to 2 μm thick.
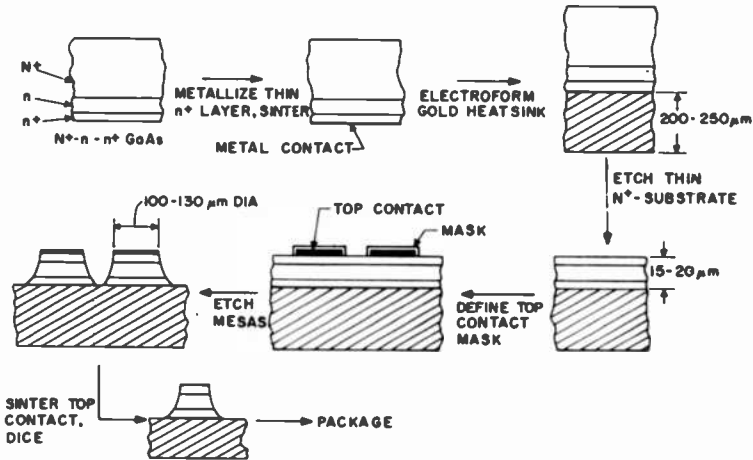
Fig. 7—Simplified process schedule for integral heat sink TEO's.

(2) A 100-125 μm thick Au heat sink is electroformed on the contact.

(3) The n+ substrate is chemically thinned down till the total GaAs thickness is of the order of 15-20 μm.

(4) For a typical top-contact pattern, 100-150 μm diameter dots are deposited, masked, and mesas etched. The Au heat sink is then diced into 500×500 $(\mu m)^2$ squares, each with the mesa in the center, and these are packaged.

The advantages of this fabrication process are: (1) it is a batch process suitable for the fabrication of multiple mesa devices to achieve both high efficiency and high power operation, (2) the removal of excess GaAs makes it suitable for realizing small diameter devices without excessive undercut during etching, (3) the removal of excess GaAs also allows the fabrication of ring structures, (4) electroforming of the Au heat sink assures intimate contact and, thus, lower thermal resistance than bonding a device directly to the heat spreader, and (5) this process can be extended to the fabrication of dual-heat-sink structures by electroforming thick-top contacts.

Results

X-band integral heat sink TEOs were fabricated from several $n+$-n-$n+$ GaAs wafers and evaluated. These wafers had nominal active lengths of 10 μm and nominal n-layer carrier concentrations of 2×10^{15} cm^{-3}, corresponding to an nl_n product of 2×10^{12} cm^{-2}. Differential capacitance measurements made on Schottky barrier diodes fabricated from $n+$-n wafers grown under conditions similar to these $n+$-n-$n+$ wafers indicate that the n-layer doping is flat to within 10%.

Table 1—Summary of Typical Integral Heat Sink Devices

Device Number	V_{bias} (Volts)	I_{bias} (Amps)	P_{out} (mW)	f (GHz)	η (%)	$\dfrac{V_{bias}}{V_{threshold}}$	d (μm)
727A3	9.5	0.100	70	11.5	7.4	2.4	110
727A5	7.5	0.120	75	9.6	8.3	2.14	110
727A8	12.0	0.120	110	9.5	8.0	3.0	110
727A4	7.5	0.100	105	8.0	14.0*	2.14	110
727A6	7.5	0.130	90	8.0	9.2	2.14	110
727A10	14.4	0.150	160	10.5	7.5	3.6	110
717E2	8.0	0.250	160	7.8	8.0	2.0	135
727B14	14.0	0.30	270	10.8	6.4	3.7	135
641B4	11.2	0.33	230	10.2	6.2	2.8	135
366C2	11.0	0.19	140	10.7	7.0	2.5	135
729B6	12.2	0.45	340	8.8	6.2	3.0	135
729B15	14.0	0.45	400†	11.3	6.4	3.5	135
729B17	14.1	0.40	340	8.5	6.1	3.5	135
729B29	11.0	0.31	305#	10.5	9.0#	2.7	135

* The best efficiency obtained to date.
† Highest P_{out} from a single-mesa device.
# Best power-efficiency combination from a single-mesa device.

Microwave measurements were made on integral heat sink TEOs with diameters ranging from 110 μm to 180 μm. The maximum output power, efficiency and operating frequency were measured using standard methods. Devices were evaluated in a reduced-height waveguide[8] and a waveguide-vane circuit[2] described elsewhere. Operation in both these circuits was comparable. The TEOs were evaluated in both polarities, i.e., in the heat-sink-anode and heat-sink-cathode configurations. Efficiencies were found to be consistently 1.5 to 2% higher in the heat-sink-anode configuration. Table 1 is a summary of results obtained in the heat-sink-anode configuration. Fig. 8 is a plot of efficiency as a function of diameter showing a decreasing trend.

Thermal measurements were made on representative devices using an infrared radiometer with a spot size of 35 μm. Fig. 9 is a plot of T_{max} versus α for a 110 μm diameter device. Note that the thermal
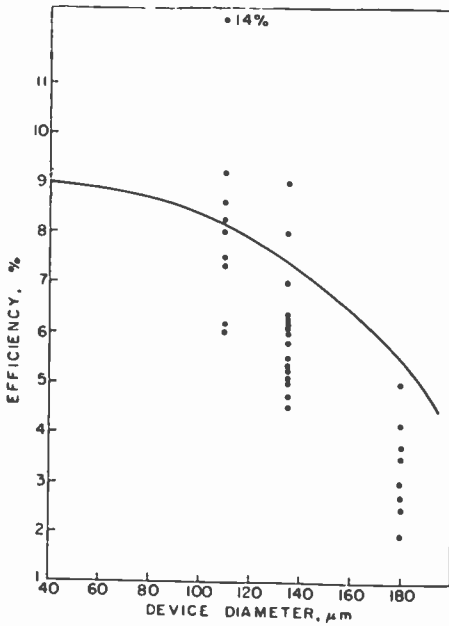
Fig. 8—Measured cw TEO efficiency as function of device diameter. Solid line is the computed curve for $\alpha = 3$, $nl_n = 2 \times 10^{12}$ cm^{-2}, and $l_n = 10$ μm.
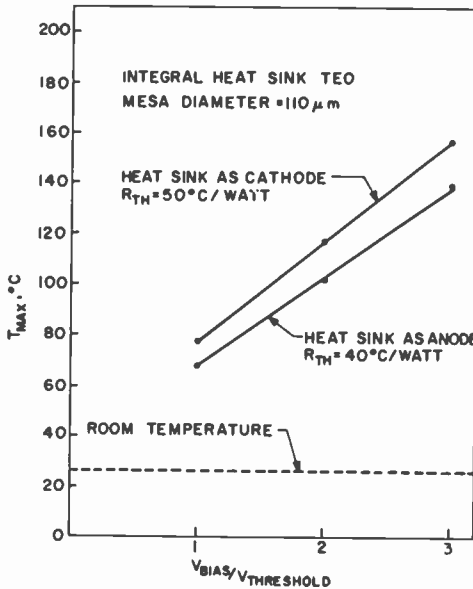
Fig. 9—Typical R_{th}, V_B/V_T characteristic for integral heat sink TEO.

resistance in the heat-sink-anode configuration is 40°C/watt in contrast to 50°C/watt in the heat-sink-cathode configuration. These measurements are consistent with the microwave measurement and indicate that heat generation is higher at the anode. This fact has been ignored in our simplified analysis, which assumed uniform heat generation, to make the thermal problem tractable. The effect of inhomogeneous heat distribution has been considered by Johnson, et al.[9] Fig. 10 is a plot of measured T_{max} as a function of mesa diameter for a number of integral heat sink TEOs fabricated from an n+-n-n+ wafer. The computed curve is also shown. Agreement between measured and computed values is within experimental error.
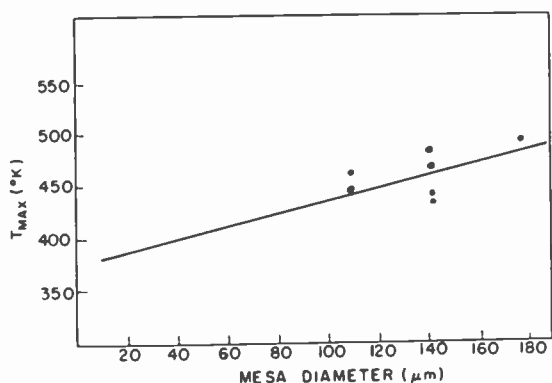
Fig. 10—Measured T_{max} as function of diameter for X-band TEO's on integral gold heat sink. Solid line shows computed curve.

Conclusions

An integral heat sink technology has been developed embodying all the guidelines developed in the simplified analysis. Using this technology we have fabricated single-heat-sink devices from several GaAs wafers that have typical cw efficiencies between 6 and 9% in X-band. The highest efficiency obtained from integral heat sink TEOs was 14% at a power level of 105 mW at 8 GHz. This is believed to be the highest efficiency reported to date for cw TEOs. The highest power output obtained from a single mesa device was 400 mW with 6.4% efficiency at 11.3 GHz, while the best power-output–efficiency combination from a single mesa structure was 305 mW at 10.5 GHz with 9% efficiency.

Acknowledgments

Appendix—Effect of Device Geometry

Consider the schematic of a typical TEO shown in Fig. 1. We will compute the maximum temperature in the active layer, temperature difference across the active layer, and the average active layer temperature under the following assumptions:

(a) One dimensional heat flow normal to the flux spreader plane is considered.

(b) The heat flux spreader is semi-infinite. This approximation has been shown to be valid for $d/D < 0.1$; and $0.04 < w/D < 4.$[10]

(c) The thermal conductivity of n and n+ GaAs are approximated by $150/T$ and $120/T$ watt/cm°C, respectively, where T is the temperature in °K.[5]

(d) Joule heating in the n+ layer is neglected.

(e) The power flux to the heat sink is Q watt/cm^2.

It can be shown that T_{max}, the maximum temperature, occurs at the active layer-substrate interface (T_{sn}) and is given by:

$$T_{max} = \left[T_o + Q\,\frac{\pi d}{8K_s} + Q\,\frac{l_c}{K_c} \right] \exp\left\{ Q\left[\frac{l_n+}{120} + \frac{l_n}{300}\right] \right\} \qquad [1]$$

and the temperature difference across the active layer ΔT, is given by

$$\Delta T = \left[T_o + Q\,\frac{\pi d}{8K_s} + Q\,\frac{l_c}{K_c} \right] \left[\exp\left\{ Q\left(\frac{l_n+}{120} + \frac{l_n}{300}\right)\right\} \right.$$
$$\left. - \exp\left\{ \frac{Ql_n+}{120}\right\} \right] \qquad [2]$$

where K_c and K_s are the thermal conductivities of the bonding layer and heat spreader, respectively. Other parameters are defined in Fig. 1.

$$T_{av} = T_{max} - \frac{\Delta T}{2}. \qquad [3]$$

The heat flux $Q = \dfrac{\text{Bias power}}{\text{area}} = \dfrac{\alpha}{\beta} E^2_T e \mu_T n l_n,$ [4]

where α is the bias/threshold voltage ratio, E_T the threshold field, and μ_T the low field mobility of the device threshold bias temperature. By using the value of μ at the ambient temperature, a conservative estimate of T_{max} is obtained.

Eqs. [1] and [2] can be extended to dual-heat-sink structures where heat is removed from both sides of the active region. The location of T_{max} will be somewhere in the active layer. Assuming that a fraction δ of the heat flux flows through the active layer–exitaxial $n+$ contact interface, it is clear from symmetry that T_{max} occurs δl_n from this interface. The dual-heat-sink structure is therefore equivalent to a single-heat-sink structure with length δl_n and heat flux δQ. The corresponding T_{max} and ΔT can be obtained from Eqs. [1] and [2];

$$T_{max} = \left[T_o + Q\delta \frac{\pi d}{8K_s} + Q\delta \frac{l_c}{K_c} \right] \exp \left\{ Q\delta \left[\frac{l_n+}{120} + \frac{\delta l_n}{300} \right] \right\} \quad [5]$$

$$\Delta T = \left[T_o + Q \frac{\pi d}{8K_s} + Q\delta \frac{l_t}{K_c} \right]$$
$$\exp \left\{ Q\delta \left(\frac{l_n+}{120} + \frac{\delta l_n}{300} \right) \right\} - \exp \frac{Q\delta l_n+}{120} \right]. \quad [6]$$

Dual heat sinking thus significantly reduces T_{max} and ΔT. We define a dual-heat-sinking efficiency parameter Δ,

$$\Delta = 2 (1 - \delta). \quad [7]$$

$\Delta = 1$ corresponds to $\delta = 0.5$ or perfect dual heat sinking and $\Delta = 0$ corresponds to $\delta = 1$ or a single heat sink.

To estimate the effect of T_{av} and ΔT, we will assume that we can neglect the formation of domains in the device. Under this assumption, the current is directly proportional to carrier velocity, and we can use the published values of the velocity peak/valley ratio for β.[3] Since the peak current is proportional to $\mu(T_{max})$ and hence $1/T_{max}$, we have

$$\beta(\text{gradient}) = \beta(T_{av}) \frac{\text{Average temperature}}{\text{Maximum temperature}}$$

$$= \beta(T_{av}) \cdot \frac{T_{max} - (\Delta T/_2)}{T_{max}}. \quad [8]$$

Once β(gradient) and $\beta(T_{av})$ are known we can estimate the efficiency by assuming a cubic current-voltage characteristic for the device and use the Van der Pol equation for nonlinear oscillators.[6] While this will not tell us the actual efficiencies obtained in practice, it will show the various trends in efficiency as device parameters are varied.

References:

[1] B. E. Berson, R. E. Enstrom and J. F. Reynolds, "High Power L and S-Band Transferred Electron Oscillators," **RCA Review,** Vol. 31, p. 20, March 1970.

[2] H. C. Huang, R. E. Enstrom, and S. Y. Narayan, "High Efficiency Operation of Transferred Electron Oscillators in the Hybrid Mode," **Electronics Letters,** Vol. 8, No 10, p. 271, May 1972.

[3] J. G. Ruch and W. Fawcett, "Temperature Dependence of the Transport Properties of GaAs Determined by a Monte Carlo Method," **J. Appl. Phys.,** Vol. 41, p. 3843, Aug. 1970.

[4] J. S. Bravman and L. F. Eastman, "Thermal Effects of the Operation of High Average Power Gunn Devices," **IEEE Trans. Electron Devices,** Vol. ED-17, No. 9, p. 744, Sept. 1970.

[5] S. Knight, "Heat Flow in n^{++}-n-n^+ Epitaxial GaAs Bulk Effect Devices," **Proc. IEEE,** Vol. 56, p. 336, March 1968.

[6] F. Sterzer, "Power Output and Efficiency of Voltage Controlled Negative Resistance Oscillators," **IEEE Trans. Electron Devices,** Vol. ED-14, p. 718, Oct. 1967.

[7] S. P. Yu and G. H. Glover, "Heat Sink Temperature Distribution of the Annular Solid State Microwave Diode," **Electronics Letters,** Vol. 7, p. 182, April 1971.

[8] S. Y. Narayan, H. C. Huang and A. R. Gobat, "Operation of TEOs in the Ridge Waveguide Circuit," **Electronics Letters,** Vol. 6, No. 1, p. 17, Jan. 1970.

[9] N. O. Johnson, K. O. I. Olsson and S. J. Wildheim, "Temperature in Gunn Diode with Nonuniform Power Dissipation," **IEEE Trans. Electron Devices,** Vol. ED-18, No. 3, p. 158, March 1971.

[10] D. P. Kennedy, "Spreading Resistance in Cylindrical Semiconductor Devices," **J. Appl. Phys.,** Vol. 31, p. 1490, Aug. 1960.

Recent Papers by RCA Authors

Listing is alphabetical by name of publication. For copies of reprints the reader should contact the publication directly.

D. E. Carlson, K. W. Hang, and G. F. Stockdale, "Electrode 'Polarization' in Alkali-Containing Glasses," **American Ceramic Society, J. of,** Vol. 55, p. 337, July 1972.

A. H. Firester, T. E. Gayesky, and M. E. Heller, "Efficient Generation of Laser Beams with an Elliptic Cross Section," **Applied Optics,** Vol. 11, p. 1648, July '72.

D. Vilkomerson, "Comments on: Light Scattering in Photographic Materials for Holography," **Applied Optics,** Vol. 11, p. 1869, Aug. '72.

M. S. Abrahams, C. J. Buiocchi, M. Rayl, and P. J. Wojtowicz, "Transmission Electron Microscopy of Granular Nickel/SiO_2 Cermet Films," **Applied Physics, J. of,** Vol. 43, p. 2537, June '72.

M. S. Abrahams, J. Blanc, and C. J. Buiocchi, "Like-Sign Asymmetrical Dislocations in Zinc-Blende Structure," **Applied Physics Lett.,** Vol. 21, p. 185, 1 Sept. 1972.

V. S. Ban, H. F. Gossenberger, and J. J. Tietjen, "Influence of Deposition Temperature on Composition and Growth Rate of $GaAs_xP_{1-x}$ Layers, "**Applied Physics, J. of,** Vol. 43, p. 2471, May'72.

A. C. Ipri, "Electrical Properties of Silicon Films on Sapphire Using the MOS Hall Technique," **Applied Physics, J. of,** Vol. 43, p. 2770, June '72.

P. D. Southgate and D. S. Hall, "Second-Harmonic Generation and Miller's Delta Parameter in a Series of Benzene Derivatives," **Applied Physics, J. of,** Vol. 43, p. 2765, June '72.

H. F. Lockwood and M. Ettenberg, "Thin Solution Multiple Layer Epitaxy," **Crystal Growth, J. of,** Vol. 15, p. 81, 1972.

C. C. Wang and S. H. McFarlane, III, "Epitaxial Growth and Characterization of GaP on Insulating Substrates," **Crystal Growth, J. of,** Vol. 13/14, p. 262, 1972.

J. I. Pankove, "Electrolytic Etching of GaN," **Electrochemical Soc., J. of,** Vol. 119, p. 1118, Aug. '72.

A. G. Sigal, M. S. Abrahams, and J. Blanc, "Properties of Vapor-Deposited Aluminum Arsenide," **Electrochemical Soc., J. of,** Vol. 119, p. 952, July '72.

M. E. Fohl, "Central Processor Unit Diagnosis by Function," **Fault Tolerant Computing Symp.,** Boston, Mass., 6/19-21/72 (Digest of Papers).

J. A. Rajchman, "A Survey on Magnetic Memories," **Ferrites, Proc. of Int'l Conf. on,** p. 409, July '70.

S. S. Perlman, J. H. McCusker, and S. M. Broadman, "Analog Memory Devices Employing PE-FE Interactions for Adaptive Control Voltage Modules," **Ferroelectrics,** Vol. 3, p. 239, Feb. '72.

A. Mack and B. Patrusky, "Time Division Digital Switch Matrix Technique Evaluation," **IEEE Int'l Conf. on Communications,** June 19-21 ,1972 (ICC '72 Conf. Proc.).

J. H. McCusker and S. S. Perlman, "Adaptive Thyristor Power-Control Circuits," **IEEE J. of Solid-State Circuits,** Vol. SC-7, p. 282, Aug. '72.

A. S. Clorfeine, H. J. Prager, and R. D. Hughes, "Improved Diode and Circuit Procedures for High-Efficiency S-Band Oscillators," **Proc. IEEE,** Vol. 60, p. 729, June '72.

P. A. Levine and V. W. Chan, "A Comparative Study for IMPATT Diode Noise Properties," **Proc. IEEE,** Vol. 60, p. 745, June '72.

H. Sobol and F. Sterzer, "Microwave Power Sources," **IEEE Spectrum,** Vol. 9, p. 20, April '72.

G. D. O'Clock, Jr., "Phase Detector Data Distortion in Phase-Lock Loop Receivers," **IEEE Trans. on Aerospace and Electronic Systems,** Vol. AES-8, p. 391, May '72.

J. Campbell and B. Popovich, "A Broad-Band Wide-Angle Scan Matching Technique for Large Environmentally Restricted Phased Arrays," **IEEE Trans. on Antennas and Propagation,** July '72.

J. E. Carnes, W. F. Kasonocky, and E. G. Ramberg, "Free Charge Transfer in Charge-Coupled Devices," **IEEE Trans. on Electron Devices,** Vol. ED-19, p. 798, June '72.

F. H. Nicoll, "Low-Voltage Electron-Beam-Pumped Lasing of CdS at Atmospheric Pressure," **IEEE Trans. on Electron Devices,** Vol. ED-19, p. 838, June '72.

R. A. Sunshine and M. A. Lampert, "Second-Breakdown Phenomena in Avalanching Silicon-on-Sapphire Diodes," **IEEE Trans. on Electron Devices,** Vol. ED-19, p. 873, July '72.

C. P. Wen, K. P. Weller, and A. F. Young, "Multilayer Vapor-Phase Epitaxial Silicon Millimeter-Wave/IMPATT Diodes," **IEEE Trans. on Electron Devices,** Vol. ED-19, p. 891, July '72.

H. Sobol, "A Review of the Technological and Electromagnetic Limitations of Hybrid Circuits for Microwave Applications," **IEEE Trans. on Parts, Hybrids, and Packaging,** Vol. PHP-8, p. 58, June '72.

B. Miyatani, F. Okamoto, P. K. Baltzer, S. Osaka, and T. Oka, "Optical Properties of Impurity Levels in $CdCr_2Se_4$ and $CdCr_2S_4$," **Magnetism and Magnetic Materials Conf. Proc.,** Chicago, Ill., Nov. 1971, p. 285, 1972.

S. T. Opresko, Jr. and H. L. Pinch, "Control of Product Phases in the Chemical Vapor Deposition of Garnet Films," **Materials Research Bulletin,** Vol. 7, p. 685, 1972.

J. S. Furnstahl, "Military/Aerospace Packaging," **Packaging and Production,** Aug. '72.

A. Pellos, R .W. Klopfenstein, "Minimal Error Constant Numerical Differertiation," **Mathematics of Computation,** Vol. 26, p. 467, April '72.

R. E. Flory, "Video Recoiding and Playback," **McGraw-Hill Yearbook of Science and Technology,** 1972.

A. W. Levine and J. Fech, Jr., "The Chemistry of Blocked Isocyanates. II. Kinetics and Mechanisms of the Reaction of Dibutylamine with Phenyl and 2-Methylphenyl Oxime Carbamates," **Organic Chemistry, J. of,** Vol. 37, p. 2455, July 28, '72.

P. M. Schwartz, R. A. Blakely, and B. B. Robinson, "Efficiency of the Electrochemiluminescent Process," **Physical Chemistry, J. of,** Vol. 72, p. 1868, June 22, '72.

R. S. Crandall, "Non-Ohmic Electron Transport on Liquid Helium," **Physical Review A,** Vol. 6, p. 790, Aug. '72.

W. Rehwald, M. Rayl, R. W. Cohen, and G. D. Cody, "Elastic Moduli and Magnetic Susceptibility of Monocrystalline Nb_3Sn," **Physical Review B,** Vol. 6, p. 363, July 15, '72.

R. Klein, "Theory of Rayleigh and Brillouin Scattering Near the Phase Transition," **Physique, J. de,** Suppl., Vol. 33, p. Cs-11, April '72.

N. Feldstein and J. A. Weiner, "The Effectiveness of Tin Sensitizer Solutions," **Plating,** Vol. 59, p. 140, Feb. '72.

G. A. Alphonse, "Broad-Band Acousto-Optic Deflectors Using Sonic Gratings for First-Order Beam Sttering," **RCA Review,** Vol. 33, p. 543, Sept. '72.

R .W. Engstrom and J. H. Sternberg, "The Silicon Return-Beam Vidicon—A High-Resolution Camera Tube," **RCA Review,** Vol. 33, p. 501, Sept. '72.

I. Ladany and H. Kressel, "An Experimental Study of High-Efficiency GaP:N Green-Light-Emitting Diodes," **RCA Review,** Vol. 33, p. 517, Sept. '72.

W. S. Pike, M. G. Kovac, F. V. Shallcross, and P. K. Weimer, "An Experimental Solid-State TV Camera Using a 32 × 44 Element Charge-Transfer Bucket-Brigade Sensor," **RCA Review,** Vol. 33, p. 483, Sept. '72.

J. L. Vossen, "Non-Destructive Sheet-Resistivity Measurements with Two-Point Probes," **RCA Review,** Vol. 33, p. 537, Sept. '72.

A. Waksberg and J. Wood, "An Automatic Optical Bias Control for Laser Modulators," **Review of Scientific Instruments,** Vol. 43, No. 9, Sept. '72.

M. Toda, "A Magnetically Susceptible, Highly Resistive Surface Layer in N-Type $CdCr_2S_4$," **3rd Solid State Devices Conf.,** Tokyo, Japan, 1971, Proceedings, Oyo Buturi Supplement, Vol. 41, p. 183, 1972.

G. D. OClock, D. A. Gandolfo, and J. R. Loose, "Acoustic Surface Wave Device Performance in Microwave Communications Systems," **Ultrasonics Symposium Digest,** Oct. '72.

J. A. Rajchman, "Promise of Optical Memories," **Vacuum Science and Technology, J. of,** Vol. 9, p. 1151, July/Aug. '72.

P. B. Silverman, "International Communications—An Overview," **WESCON/72 Digest.**

Patents Issued to RCA Inventors Third Quarter, 1972

July

R. W. Ahrons Delay Line Using Integrated MOS Circuitry (3,676,711)
R. W. Ahrons High Gain MOS Linear Integrated Circuit Amplifier (3,678,407)
T. P. Allington Method of Electrically Mounting Components in Hybrid Circuits (3,676,252)
T. G. Athanas Formation of Openings in Insulating Layers in MOS Semiconductor Devices (3,674,551)
J. Avins Amplifier-Limiter Circuit with Reduced AM to PM Conversion (3,678,405)
J. Avins Variable Gain Amplifier (3,678,406)
J. Avins and **L. R. Kirkwood** Control Apparatus for a Color Television Receiver (3,679,816)
C. D. Boltz, Jr. Optical Apparatus for Continuous Television Film Projection System (3,679,827)
D. S. Bond Radio Facsimile Postal System for Multiple Addresses (3,678,180)
R. A. Bonnette Filamentary Display Devices (3,673,652)
L. J. Caprarola Hybrid Thermoelectric Generator (3,674,568)
J. A. Castellano and R. N. Friel Liquid Crystal Display Device Including Side-By-Side Electrodes on a Common Substrate (3,674,342)
J. R. Collard Support for Electrical Components and Method of Making the Same (3,678,995)
J. Craft Balanced Variable Gain Amplifier (3,678,403)
F. P. Daly Metal-Oxide-Metal, Thin-Film Capacitors and Method of Making Same (3,679,942)
J. A. Dodd, Jr. and G. H. Lines Method of Making Matching Photoprinting Masters (3,674,488)
W. G. Einthoven, E. S. Jetter, and C. F. Wheatley, Jr. Method of Making Transistors Including Base Sheet Resistivity Determining Step (3,676,229)
A. N. Goldsmith Three-Dimensional Television System (3,674,921)
D. F. Griepentrog Automatic Beam Current Limiter (3,674,932)
D. Hampel Multi-Function Logic Gate Circuits (3,678,292)
G. D. Hanchett Alarm Circuit (3,680,068)
M. M. Kaufman Decoder Circuit (3,679,911)
S. A. Keneman and A. Miller Electro-Optical Memory Employing Ferroelectric Element (3,680,060)
H. G. Kiess Non Air-Polluting Corona Discharge Devices (3,675,096)
W. L. Lehmann Capacitors of Constant Capacitance (3,675,095)
A. L. Limberg Synchronous Demodulator Employing Common Base Transistor Amplifier Input and Base-Emitter Clamping Action (3,679,981)
A. L. Limberg Synchronous Demodulator Employing Transistor Base-Emitter Clamping Action (3,679,982)
E. Luedicke and R. S. Silver Method of Operating an Information Storage Tube (3,675,134)
E. P. McGorgan, Jr. Comparator Circuit (3,676,702)
J. E. Meyer, Jr. Logic Circuits Employing Switches Such as Field-Effect Devices (3,676,705)
H. I. Moss and E. F. Hockings Magnetic Head with Modified Grain Boundaries (3,676,610)
F. Okamoto, Y. Wada, and K. Miyatani Magnetic Compositions (3,679,379)
P. C. Olsen and P. C. Tang Video Blanking and Sound Muting Circuit Employing Grounded Tuner Switches (3,679,819)

F. R. Ragland, Jr.   Method for Making a Light Intensity Correction Filter   (3,676,129)
M. Robbins   Magnetic Compositions   (3,676,082)
A. I. Stoller and S. T. Opresko   Method and Material for Etching Semiconductor Bodies   (3,677,848)
K. Strater, W. B. Hall, E. M. Mihalick, and W. C. Stever   High Capacity Deposition Reactor   (3,673,983)
G. V. Taylor   Tape Winding Mechanism   (3,677,505)
E. S. Thall   Method for Filling an Evacuated Electron Tube with Gas to Atmospheric Pressure   (3,679,284)
G. J. Thibodeau   Clamp Circuit for Preventing Saturation of Operational Amplifier   (3,679,989)
P. K. Weimer   Decoders and Coupling Circuits For Solid State Video Pickup   (3,676,590)
O. M. Woodward   Printed Circuit Balun   (3,678,418)
B. Zuk   Transmission Gate and Biasing Circuits   (3,675,144)

August

J. G. Banfield, S. Y. Husni, and W. J. Greig   Method of Fabrication of Semiconductor Devices   (3,686,080)
J. D. Callaghan   Antenna System for Television Reception Within Both the UHF and VHF Television Band of Frequencies   (3,683,391)
T. J. Christopher   Astable Multivibrator Circuit with Means for Ensuring Proper Starting of Oscillations   (3,688,154)
S. B. Deal and D. W. Bartch   Electron Tube Having Tamper-Detectable Label Attached Thereto   (3,680,236)
R. S. Degenkolb and E. R. Skaw   High Q Circuits on Ceramic Substrates   (3,681,713)
A. G. F. Dingwall   Operation of Field-Effect Transistor Circuits Having Substantial Distributed Capacitance   (3,688,264)
R. A. Dischert and J. F. Monahan   Contrast Compression Circuits   (3,684,825)
W. A. Dischert   Sheet Metal Waveguide Constructed of a Pair of Interlocking Sheet Metal Channels   (3,686,590)
P. J. Donald   Method of Pressure Treating Electrophotographic Recording Elements to Change Their Sensitivity to Light   (3,681,071)
N. Feldstein   Method of Producing a Luminescent-Screen Structure Including Light-Emitting and Light-Absorbing Areas   (3,681,110)
W. V. Fitzgerald, Jr. and P. C. Wilmarth   Horizontal Oscillator Disabling   (3,688,031)
H. R. Frey   Photographic Method for Printing a Screen Structure for a Cathode-Ray Tube   (3,685,994)
A. N. Gardiner   Method for Manufacturing Wire Bonded Integrated Circuit Devices   (3,685,137)
J. B. George   VHF and UHF Automatic Gain Control Circuitry Derived From a Single Control Voltage   (3,688,198)
R. N. Guadagnolo   High Voltage Pulse Generator   (3,686,516)
L. A. Harwood   Integrated Circuit Biasing Arrangements   (RE27454)
K. G. Hernqvist   Gas Laser Discharge Tube   (3,683,295)
C. J. Hirsch   Time Delay Device   (3,688,131)
C. Y. Hsueh   Measurement of Maximum Dynamic Skew in Parallel Channels   (3,681,693)
R. N. Hurst   System for Record Medium Control and Editing   (3,684,826)
A. C. Ipri   Synchronizing System   (3,688,037)
D. A. Johnson   Low Level DC Amplifier with Automatic Zero Offset Adjustment   (3,681,703)
H. Kawamoto   Microwave Apparatus Using Multiple Avalanche Diodes Operating in the Anomalous Mode   (3,683,298)
M. S. Masse and J. P. McDowell   Servo System with Noise Cancellation   (3,683,254)
L. C. Morris   High Speed Tunable Maser for Use in Radar and Communication Receivers   (3,688,207)
L. S. Napoli and J. J. Hughes   Coax Line to Strip Line End Launcher   (3,686,724)
P. Nyul   Angled Array Semiconductor Light Sources   (3,686,543)
J. I. Pankove   Electroluminescent Semiconductor Device of GAN   (3,683,240)
S. S. Perlman and J. H. McCusker   Ferro-Electric Transformers with Means to Suppress or Limit Resonant Vibrations   (3,683,211)
W. Phillips   Doped Calcium Fluoride and Strontium Fluoride Photochromic Compositions   (3,684,727)
R. R. Russo   Process for Forming an Isolated Circuit Pattern on a Conductive Substrate   (3,682,785)

R. J. Ryan, S. F. Burtis, and J. T. Grogan Process For Forming a Conductive Coating on a Substrate   (3,682,784)
A. N. Saxena Method of Coating Selective Areas of the Surface of a Body   (3,687,722)
E. W. Schlieben Bookbinding   (3,685,857)
S. Shwartzman Gallium Arsenide Semiconductor Device With Improved Ohmic Electrode   (3,686,539)
L. E. Smith Transistorized Vertical Deflection Circuit   (3,684,920)
C. L. Upadhyayula and B. S. Perlman Stabilized Transferred Electron Amplifier (3,686,578)
P. K. Weimer Bucket Brigade Scanning of Sensor Array   (3,683,193)
C. F. Wheatley, Jr. Deflection Circuit   (3,688,153)
M. J. Whittemore, Jr. Recorder and Playback Apparatus for Pulse Width Modulated Record   (3,688,025)
Y. Yao Capacitive Steering Networks   (3,684,899)

September

J. K. Allen and M. N. Norman Television Image Control Circuit   (3,692,931)
D. S. Bond Apparatus for the Automatic Navigation of a Sailing Vessel   (3,691,978)
J. G. Butler Waveform Generator   (3,689,914)
V. M. Cannuli Method of Forming an Epitaxial Semiconductive Layer with a Smooth Surface   (3,692,594)
D. J. Carlson Mixer Circuit   (3,694,756)
K. K. Chang Solid State Microwave Heating Apparatus   (3,691,338)
N. Feldstein Electroless Nickel Plating Method   (3,690,944)
H. G. Greig Electrostatic Printing   (RE27490)
S. E. Harrison and R. Drake Photocolorable Vacuum Sublimed Xanthene Dye (3,690,889)
F. Z. Hawrylo and H. Kressel Method of Forming Semiconductor Device with Smooth Flat Surface   (3,692,593)
C. C. Ih Sound Records and Reproducing Apparatus   (3,689,692)
L. B. Juroff and L. M. Lunn Remote Controlled Television Tuner Motor Switching Circuit   (3,691,444)
R. I. Klein, S. Caplan, and R. T. Hansen Liquid Crystal Display Device   (3,689,131)
G. E. Long III and D. W. Bartch Spray Method for Producing a Glare-Reducing Coating (3,689,312)
M. J. Lurie High Resolution, Redundant Coherent Wave Imaging Apparatus Employing Pinhole Array   (3,689,129)
D. P. Marinelli Method and Apparatus for Depositing Epitaxial Semiconductive Layers from the Liquid Phase   (3,692,592)
H. Nelson Method of Making Light Emitting Diode   (3,694,275)
G. S. Newcomb Conversion to a Digital Code Which is Self-Clocking and Absolute Phasing   (3,689,913)
C. L. Olson and R. A. Dischert Automatic Registration of Color Television Cameras (3,692,918)
F. J. Papiano Method of Alloying Two Metals   (3,690,943)
A. Presser Variable Tuning Arrangement for a Strip Transmission Line Circuit (3,693,118)
A. N. Saxena Schottky Barrier Diode   (3,694,719)
L. J. Thorpe Special Effects Generator   (3,689,694)
J. L. Vossen, Jr. Method of Radio Frequency Sputter Etching   (3,692,655)
W. R. Walters Time Delay Circuits   (3,693,030)
P. C. Wilmarth Horizontal Oscillator Disabling Circuit Control Apparatus   (3,692,932)
C. F. Wheatley, Jr. Television Deflection System Including AFC Circuit with Regenerative Phase Detector   (RE27492)

AUTHORS

Erwin F. Belohoubek received the degree of Diplom-Ingenieur in 1953 and the Ph.D. in Electrical Engineering in 1955 from the Technical University in Vienna, Austria. From 1953 to 1955, he worked as Research Assistant at the Institute for High Frequency Techniques of the same university. He joined the RCA Electronic Components Division in Harrison, New Jersey, in 1956 and transferred to the Microwave Technology Center in Princeton, New Jersey, in 1957. Here he worked on the development of magnetrons, electrostatically and magnetically focussed traveling-wave tubes, and a crossed field microwave delay tube. In 1969, Dr. Belohoubek became Leader of a group working on hybrid integrated circuits. He is presently responsible for the development of passive and active MIC circuits, including high-power transistor amplifiers, multipliers, linear amplifiers, circulators and limiters, and acoustic delay devices. He received an Outstanding Performance Award of the RCA Electronic Components Division in 1963 and an RCA Laboratories Achievement Award in 1967.

Dr. Belohoubek is a Senior Member of the IEEE.

James E. Carnes received the B.S. degree from Pennsylvania State University, University Park, in 1961, and the M.A. and Ph.D. degrees in electrical engineering from Princeton University, Princeton, N. J., in 1967 and 1970, respectively. His Ph.D. dissertation was an investigation on photo-induced currents and charge transport in polyvinylcarbazole, an organic polymer. He was in the U. S. Navy from 1961 to 1965. During the summers of 1966 and 1967 he investigated metallic contacts and dc electroluminescence in strontium titanate at RCA Laboratories, David Sarnoff Research Center, Princeton, N. J., which he joined as a member of the technical staff in 1969. Since that time he has studied electrical breakdown, conduction, and interface properties of various insulating films on silicon and is currently involved in the investigation of charge-coupled devices.

Dr. Carnes is a member of the American Physical Society, Tau Beta Pi, Phi Kappa Phi, and IEEE.

Peter Foldes received his diploma of electrical engineering from the Technical University of Budapest in 1950. He did his Post Graduate work at the Telecommunication Research Institute and Academy of Science in Budapest between 1953 and 1956. In the early part of his career, he was involved in the design of airborne communication radio, radar transmitters and antennas, propagation studies and system design of radar and microwave communication systems at the Army Research Institute and the Telecommunication Research Institute of Budapest. In 1957, he joined RCA Limited in Montreal, where he was involved in the rf-multiplexer, waveguide, and antenna-system design for the Alaska and Trans-Canada microwave communication systems. During this period, he pioneered the use of Cassegrainian antennas for communication systems, which led to a participation in various NASA-JPL programs. On the basis of his work JPL built the first 85-foot Cassegrainian antenna for Space Communication, and his rf-optics design was adapted for JPL's 210-foot diameter antenna. Since 1962, he has designed a number of rf-optics and feed systems for the Intelsat network. These are now in operation or being built in Canada, the United States, Panama, Brazil, Argentina, India, and Pakistan. In 1969, he became Staff Engineer for RCA Space Systems. In this capacity, he was involved in Earth Station as well as Aerospace problems and conducted studies into the long term aspects of communications. Recently, he designed a 30-foot antenna to meet the Earth-Station requirements of the Canadian Telesat network and led the development of the antenna required for the space craft. Mr. Foldes has been a lecturer at both the Technical University of Budapest and at McGill University in Montreal.

Peter V. Goedertier obtained his Bachelor's Degree at the University of Louvain, Belgium. He later took a License Degree in Mathematics at the same University, majoring in theoretical physics. He taught Statistics at the Antwerp Business School, and was granted a leave of absence to study microwave theory and techniques at Cruft Laboratory, Harvard University, in 1947-1948. After that, he was appointed Professor of Physics at the Philosophical College of Louvain. In 1954, he conducted a research project on microwave spectroscopy at the Center of Physique Nucleaire of the University of Louvain, working mainly on the determination of the molecular structural constants of vinyl bromide and its deutero substitutes. In 1958 he came to the United States as a Research Associate in the Microwave Spectroscopy Group of Duke University. He joined RCA Laboratories, Princeton, New Jersey in 1959.

At RCA Laboratories he has studied the interaction of gas molecules with crystalline fields (in the course of this work he developed a new kind of Cs-ion source), has been engaged in the early research on optical masers (both gaseous and solid-state materials), and was a co-discoverer of the He-Ne "cascade" laser. In 1965, he was given an Achievement Award for his contributions to the development of the cross-pumped YAG:Nd:Cr laser. For the past three years, he has worked on the development of various optical systems relating to the processing and the displaying of video information.

Istvan Gorog attended the University of California at Berkeley, where he received the B.Sc. (1961) and the M.Sc. (1962) and Ph.D. (1964) degrees in Electrical Engineering. In September 1964, Dr. Gorog joined RCA Laboratories, David Sarnoff Research Center, where his main areas of concern have been quantum electronics and electro-optical systems. His activities have included gas laser research, holography, investigation of pre-recorded video recording and playback techniques, laser deflection, and photochromic and cathodochromic devices and systems. Currently he is head of the Optical Electronics Research Group in the Physical Electronics Research Laboratory. During 1968 Dr. Gorog was on leave of absence from RCA as a National Science Foundation Post-Doctoral Fellow in Frascati, Italy, where he worked on laser related problems in plasma research.

Dr. Gorog is a member of the American Physical Society and of Eta Kappa Nu.

Joseph D. Knox received his B.S. degree in Electrical Engineering from the University of Dayton in Dayton, Ohio, in 1966 and his M.S. and Ph.D. degrees from Case Institute of Technology in Cleveland, Ohio, in January 1970 and September 1970, respectively. During his stay at Case Institute, Dr. Knox did an extensive study of the absorption of iodine 127 and iodine 129 inside and outside the cavity of a He^3-Ne^{20} laser. In the course of this work, he developed a spectroscopic technique that gave sufficient resolution to observe the actual hyperfine structure (38 lines in all) of iodine 129. Dr. Knox also engaged in a study of the He-Ce laser, high-power CO_2 lasers, the use of cold cathodes in gas lasers, and the design and development of He-Ne lasers for special applications. He joined RCA in September 1970, working on the design and development of a laser deflection display system. His other activities include the design and fabrication of acousto-optic deflectors, modulators, and cavity "dumpers" for visible and infrared lasers. The tellurium dioxide deflectors and latest lead molybdate deflector incorporated in the laser deflection system described were of his design.

Dr. Knox is a member of Tau Beta Pi (Physics and Engineering Honorary), Sigma Xi, the IEEE, and the Optical Society of America.

Walter F. Kosonocky received the B.S. and M.S. degrees in electrical engineering from Newark College of Engineering, Newark, N. J., in 1955 and 1957, respectively, and the Sc.D. degree in engineering from Columbia University, New York, N. Y. in 1965. Since June 1955 he has been employed at RCA Laboratories, Princeton, N. J., where he has conducted research on application of new phenomena and new devices for information processing systems. This work has included ferrite memory systems, parametric digital devices, tunnel-diode circuits, tunnel-diode and transistor circuits, pattern-recognition systems, applications of lasers for digital systems (including a study of saturable absorbers for Q-switched lasers and semiconductor laser digital devices), optical hologram memory systems and page composition, optically controlled p-MOS circuits, and a liquid-crystal image converter. Presently he is working on the development and applications of charge-coupled devices.

Dr. Kosonocky is a member of Sigma Xi, Tau Beta Pi, Eta Kappa Nu, and a senior member of IEEE.

Shing-gong Liu received his B.S. degree in electrical engineering from Taiwan University, Taipei, Taiwan, in 1954, the M.S. degree in electrical engineering from North Carolina State College, Raleigh, North Carolina, in 1958, and the Ph.D. degree in electrical engineering from Stanford University, Stanford, California, in 1963. From 1958 to 1959 he worked with the IBM Laboratories, Poughkeepsie, New York. He was a research assistant at the Hansen Microwave Laboratories, Stanford University, where he worked in the field of microwave ferrites. He joined RCA Laboratories, Princeton, New Jersey, in 1963, and has since worked principally in the areas of semiconductor microwave devices.

Dr. Liu is a member of Phi Kappa Phi, Sigma Xi, and the American Physical Society.

S. Yegna Narayan received his B.Sc. (Honors) from the University of Delhi, India in 1959, his B.E. (Distinction) from the Indian Institute of Science, Bangalore, India, in 1962, and his M.S. and Ph.D. from Cornell University in 1964 and 1966, respectively. His graduate research dealt with the coupling of microwave energy to plasma systems. Since joining the staff of RCA Laboratories in 1966, Dr. Narayan has been working in the area of high-power epitaxial GaAs microwave devices. Most of his effort has been on the development of high-power cw X-band TEOs. He was the recipient of the RCA Laboratories Outstanding Achievement Award for the team effort in the development of GaAs transferred electron device technology. Dr. Narayan is now responsible for epitaxial GaAs growth in the Microwave Technology Center. He is an associate member of Sigma Xi, and a member of the American Physical Society.

John P. Paczkowski received his B.S. degree in Physics from the Polytechnic Institute of Brooklyn in 1969. He has been with RCA since 1950 and worked as a Design Draftsman and Engineering Associate on microwave devices. Since he joined the Microwave Technology Center in 1962 he has worked on the fabrication of various solid-state microwave devices. In 1968 he was associated with the formation of the semiconductor processing and fabrication laboratory in the Microwave Technology Center. He worked on the development of electro-chemical, vacuum and sputtering deposition of metal on semiconductors for ohmic contacts and Schottky barriers. He has experience in the processing of both silicon and gallium arsenide microwave devices.

Adolph Presser received the B.E.E. degree in 1950 from the Institute of Technology, Vienna, Austria, and the M.E.E. degree in 1961 from the Polytechnic Institute of Brooklyn. From 1950 to 1952 he was a production engineer for the Schrack A.G. in Vienna, and from 1954 to 1959 he was a development engineer for the Allied Control Co. in New York. In 1959, Mr. Presser joined the RCA Microwave Technology Center at the David Sarnoff Research Center in Princeton, New Jersey, where he worked on the development of various solid-state microwave devices, including parametric amplifiers, tunnel-diode amplifiers, tunnel-diode frequency converters, and tunnel-diode oscillators. In 1965 his field of interest broadened to include microwave integrated circuitry. He has been instrumental in the design and development of telemetry transmitters, high-power transistor amplifiers, power sources for ECM systems, and more recently, of linear transistor power amplifiers and Doppler radar modules.

Mr. Presser received an Outstanding Performance Award of RCA Electronic Components in 1964 and an RCA Laboratories Achievement Award in 1965. He is a member of the IEEE.

James F. Reynolds received his B.E.E., M.E.E., and Ph.D. from Rensselaer Polytechnic Institute in 1964, 1965, and 1967, respectively. His doctoral thesis investigated methods of stabilizing gaseous magneto-plasmas by controlling the magnetic field geometry. His earlier graduate research was concerned with the use of microwave techniques for plasma diagnostics. Since joining the RCA Microwave Technology Center in 1967, Dr. Reynolds has been engaged in work on silicon and GaAs active microwave devices. In 1968, he received an RCA Laboratories Achievement Award for his research on transferred electron oscillators. His recent work has been concerned with the development of Trapatt diode sources for military and commercial systems. This work has included device, rf circuit, and pulse modulator development.

Dr. Reynolds is a member of Tau Beta Pi, Eta Kappa Nu, and an associate member of Sigma Xi.

Arye Rosen received the B.S.E.E. degree from Howard University in 1963, and the M.Sc.E. degree from Johns Hopkins University in 1965. He was an instructor at Johns Hopkins during the year 1963-64, and presently is enrolled in a Ph.D. program at Jefferson University. From 1964 to 1967, Mr. Rosen was concerned with systems design at General Telephone and Electronics International, and with antenna and circuit design at Channel Master, Inc., and American Electronic Laboratories, Inc. In 1967, Mr. Rosen joined the RCA Microwave Technology Center in Princeton, N. J., where he is presently engaged in the study and development of microwave circuits for solid-state microwave oscillators and amplifiers, including varactor multipliers, transistors, and Trapatt devices.

Mr. Rosen is a member of Tau Beta Pi, Sigma Xi, and the Association of Professional Engineers of British Columbia.

Igal Shidlovsky graduated from the Israel Institute of Technology in Haifa, Israel with a B.S. in chemistry in 1961. He obtained his M.S. in Inorganic Chemistry from Hebrew University in Jerusalem in 1963. His Ph.D. in Inorganic Chemistry was obtained from Hebrew University in 1968. His Ph.D. thesis was in the area of silicides and germanides of the rare earth metals. He concurrently served as an instructor in the chemistry department. During the academic year 1968-69, he was a Research Associate in the Physical Chemistry Department at the University of Pittsburgh working on magnetic properties of intermetallic compounds. In August 1969, he joined RCA Laboratories in the Luminescent and Electro-optics group of the Materials Research Laboratory. His primary interest has been in the area of inorganic photochromics and cathodochromic materials.

Dr. Shidlovsky is a member of the Sigma Xi and the Electrochemical Society.

Gerald E. Theriault received the B.S. degree in Engineering Physics from the University of Maine in 1950. After Air Force Service, he joined the Advanced Development Section of Home Instruments Division at RCA. From 1952 to 1963, he contributed to the application of semiconductors to radio and television circuit design. In 1963, he was transferred to the Defense Microelectronic Engineering group where he has contributed to the technology of the design and application of integrated circuits for microelectronic communication equipment. In 1966, he was promoted to the position of Leader, Analog Circuit Development. During 1968, he held the positon of Leader in the area of circuit evaluation and design for microwave hybrid circuits using semiconductors. In 1972, he joined the Microwave Technology Center at the RCA David Sarnoff Research Center in Princeton, New Jersey.

James P. Wittke received the M.E. degree from Stevens Institute of Technology, Hoboken, New Jersey in 1949, and the M.A. and Ph.D. degrees in physics from Princeton University, Princeton, New Jersey in 1952 and 1955, respectively. His doctoral research was a precision microwave determination of the hyperfine splitting in atomic hydrogen. He was an instructor in the Physics Department at Princeton for one year before joining the technical staff of RCA Laboratories, Princeton, New Jersey. At RCA he has engaged in paramagnetic resonance and microwave maser studies, in research on optically excited crystal lasers, and in investigations of the motions and properties of impurities in rutile. He has also worked on various classified projects. In 1967 Dr. Wittke was awarded an RCA Fellowship for a year of study abroad at the Clarendon Laboratory at Oxford, England. Since returning to America, he has studied the luminescence of heavily doped GaAs, helped develop new infrared-stimulated light emitting phosphors, and worked on the generation of ultra-short laser pulses, using mode-locking techniques.

Dr. Wittke is a Fellow of the American Physical Society, and is a member of the IEEE, Sigma Xi and Tau Beta Pi.

RGA
Review

Index 1972 Volume 33

Contents

March 1972 Volume 33 Number 1
Special Issue

Optical Storage and Display Media

June 1972   Volume 33   Number 2

Index to Authors, Volume 33, 1972